

In presenting this dissertation as a partial fulfillment of the requirements for an advanced degree from Emory University, I agree that the Library of the University shall make it available for inspection and circulation in accordance with its regulations governing materials of this type. I agree that permission to copy from, or to publish, this dissertation may be granted by the professor under whose direction it was written when such copying or publication is solely for scholarly purposes and does not involve potential financial gain. In the absence of the professor, the dean of the Graduate School may grant permission. It is understood that any copying from, or publication of, this dissertation which involves potential financial gain will not be allowed without written permission.

Christopher J. Lue

Spectroscopic Characterization of Matrix Isolated Transient Species

By

Christopher J. Lue
Doctor of Philosophy

Department of Chemistry

Michael C. Heaven, Ph.D.
Adviser

Tim Lian, Ph.D.
Committee Member

Myron Kaufman, Ph.D.
Committee Member

Accepted:

Lisa A. Tedesco, Ph.D.
Dean of the Graduate School

Date

Spectroscopic Characterization of Matrix Isolated Transient Species

By

Christopher J. Lue

B.S., Washington and Lee University, 2001

Adviser: Michael C. Heaven, Ph.D.

An Abstract of

A dissertation submitted to the Faculty of the Graduate

School of Emory University in partial fulfillment

of the requirements for the degree of

Doctor of Philosophy

Department of Chemistry

2008

Part I describes the electronic spectra of various actinide containing compounds isolated in solid Ar using laser induced fluorescence (LIF) spectroscopy. The IR spectra for many of the same molecules were also recorded to aid in the identification of the fluorescing species in the LIF spectra.

LIF spectra of UO_2 isolated in solid Ar were recorded to investigate the interactions between actinide compounds and the rare gas matrix host. At the time of the experiments, it had been proposed that for UO_2 and CUO , the interactions between the actinide containing molecule and Ar were strong enough to reorder the low-lying electronic states of the molecule. The experiments presented here showed no evidence of a reordering of low-lying electronic states based on comparison of the matrix spectra with theoretical predictions and gas phase spectra.

An attempt to observe fluorescence from higher order uranium oxides was undertaken. A matrix was made by ablating U metal in a 1.0% O_2 / Ar mixture. UO_3 was a probable molecule formed in the experiment. And, while absorptions belonging to UO_3 were observed in IR spectra, LIF from the same matrix provided evidence that another molecule was fluorescing. Two different vibrational frequencies observed in the U-O symmetric stretching region were indicative of at least two low-lying electronic states in fluorescing molecule. UO_3 is a closed shell molecule, and it is unlikely that it has any low-lying electronic states. Instead, the fluorescence was attributed to the open shell species $(\text{UO}_2)^+(\text{O}_2)^-$.

LIF and IR spectra of thermally vaporized UCl_4 isolated in solid Ar were recorded. UCl_4 contains U(IV), which is the most stable oxidation state other than U(VI). Before these experiments, no fluorescence had been recorded that could be attributed to UCl_4 . Based on the observed vibrational frequencies in the fluorescence bands and the lifetime of the fluorescence, it was determined that there was at least two different fluorescing species. The short lived fluorescence was assigned to UCl_4 , and the long-

lived fluorescence was assigned to UOCl_x . A low resolution map for the electronic levels in UOCl_x was created.

One of the first LIF studies of actinide containing molecules was performed by Grzybowski and Andrews[1] for UF_6 . While, the same group later recorded IR spectra for the UF_x fragments[2], no fluorescence spectra were recorded. Spectra were recorded here of UF_x fragments trapped in solid formed by either passing UF_6 through a microwave discharge or ablating U atoms into an F_2 / Ar mixture. At the time of these experiments, the IR spectrometer was not available, and the molecules producing the fluorescence could not be deduced solely from the LIF spectra. A comparison with previous IR spectra[2] gave some indication of possible candidates.

In all the experiments that investigated uranium containing matrices with IR spectroscopy, UN_2 was observed. A search was undertaken to observe fluorescence from UN_2 . To insure a good yield of UN_2 , 1% N_2 was added to the carrier gas. The fluorescence spectra observed in these experiments was very intriguing, but was determined not to be coming from UN_2 , rather it appears to be coming from U atom clusters. However further experiments are necessary to confirm how many atoms are in the clusters.

The final part of this thesis focuses on the electronic spectra of Xe-OH isolated solid Ar. Rare gas radical systems (Rg-X) such as Rg-OH are a good model system for studying weak, long range intermolecular interactions. It is known that when Rg=Xe, the strength of the interaction is much larger. For most Rg-OH complexes, the spectroscopic constants have been determined previously[3]. However, the constants for Xe-OH are currently undetermined. Gas-phase studies were undertaken to determine these constants.[4] However, these experiments were in conflict with previous LIF spectra recorded in a matrix in which Goodman and Brus[5] observed that the $A \rightarrow X$ emission band for Xe-OH is redshifted approximately $5,000 \text{ cm}^{-1}$, which is unusually large. Additionally, they found Xe-OH relaxes much faster than other

Rg-OH species. The experiments in this part of the dissertation confirm the findings Goodman and Brus with the exceptions being in the line shape of the fluorescence bands and the extent to which Xe shortens the lifetime of the OH fluorescence.

Spectroscopic Characterization of Matrix Isolated Transient Species

By

Christopher J. Lue

BS, Washington and Lee University, 2001

Adviser: Michael C. Heaven, Ph.D.

A dissertation submitted to the Faculty of the Graduate
School of Emory University in partial fulfillment
of the requirements for the degree of
Doctor of Philosophy

Department of Chemistry

2008

Acknowledgements

First and foremost, I want to thank Dr. Jin Jin. She worked alongside me during most of the experiments. Without her, most of this work would not be possible. Also, I owe great gratitude to Dr. Jiande Han and the rest of the Heaven group for serving as my mentors during my first several years at Emory University.

My inspiration for studying chemistry and obtaining my Ph.D. came from my high school chemistry teacher Lisa Blowers. She made me passionate about the subject. I also owe a great gratitude to Dr. Erich Uffelman, my undergraduate academic advisor at Washington and Lee University, and Dr. Matthew Tuchler, my undergraduate research advisor. It was Dr. Tuchler who introduced me to laser spectroscopy and my great sparked interest in lasers. The skills he taught me were invaluable for my tenure as a graduate student and future career as a physical chemist.

While those people fore mentioned helped get me to this stage in life, I owe my deepest appreciation to my advisor at Emory University, Dr. Michael Heaven. It was he who believed I could succeed as a graduate student, always putting in countless hours to help me revise a presentation for my Ph.D. committee or poster for a conference, and most of all, helping me to finish my dissertation. He taught me numerous skills about lasers and laser spectroscopy. Another person I would like to thank is Patrick Morris of the electronic shop in the Emory Chemistry Department. It is he who taught me the details of reading circuit diagrams and the skills necessary to troubleshoot and repair electronic devices that I used and will use in my research. Also, I would like to thank Jaime Rhieneker-Clayton, a fellow graduate student who helped me through the difficult years of completing all the requirements necessary for a Ph.D. degree.

In addition, there are several other people I would like to thank at Emory University. First I want to thank Kim Smith, the graduate coordinator during my first years at Emory. My first year living in Atlanta was very chaotic to say the least, and I owe

my survival to her. Additionally, I owe thanks to Ann Dasher and Tanya Chambers who assumed Kim's duties. Secondly, I want to thank Diedre Russell, Ethel Ellington, and the rest of the chemistry office staff who were always there to assist me. Third, I want to thank the chemistry stockroom staff. Fourth, I would like to thank all the faculty at Emory who taught me and prepared me with all the knowledge necessary for my degree. Fifth, I owe my gratitude to Dr. Hilary Ford, my mentor during my years in student government at Emory. Lastly, I would like to thank Dr. Tim Lian, Dr. M.C. Lin, Dr. Myron Kaufman, the members of my committee, for their time and effort in getting me to this stage.

With all my gratitude to the faculty and staff at Emory there still more people who I need to thank namely my family. My parents— through all the good times and the bad times you have always been there for me. Whether it was taking me to various activities as a kid or helping to proofread a high school English paper, you were always there. You also provided the financial support and sacrifices needed to put three kids through college (two of them graduate school). My sister, Jennifer, you were like my best friend growing up. You are so talented and set such high goals for yourself. I will always look up to you. Lastly, my bother— while we were nearly 10 years apart growing up, you were the technology person in the family, always willing to give advice on my countless computer problems.

There is another person I need to thank, Lee Cancellia or Mr. C. as he is known by me and many others. He taught me so many lifelong skills, whether it is the basics of automotive repair, a skill that is very useful to experimental physical chemistry, or learning how to swim. Whenever I have a question you always welcome it with a warm, kind-hearted spirit that is hard to come by these days.

I could go on and on thanking friends and family, and to those I did not explicitly mention above thank you. For there is no way I could be where I am today without your love and support. Finally, as I conclude these acknowledgements, I would like to

thank Stephanie DeSantis. Today, it is hard to find a person whom one can really trust, and she is one of those few people. This past year was long and tiring as I spent endless hours completing my dissertation. Through it all, you have always been there. You are truly the best and no matter what life holds in store for us you will always be one of my best friends.

In memory of Therese M. Brown.

Grandma, there is not a day that goes by that I do not think of you. I miss you dearly. I only wish you were here to see me obtain my degree. But I know you are and always will be with me in spirit.

Contents

1	Introduction	1
1.1	Actinide Spectroscopy	2
1.2	Rare Gas Radical Complexes	3
2	Introduction to Matrix Isolation Spectroscopy	5
2.1	Why is Matrix Isolation Spectroscopy Useful?	5
2.2	Experiment Setup	7
2.3	Sample Preparation	11
2.3.1	Room Temperature Gaseous Samples	12
2.3.1.1	Cl ₂ Shakedown Experiments	13
2.3.1.2	Using a Microwave Discharge to Fragment Samples	13
2.3.2	Room Temperature Solid Samples	16
2.3.2.1	Laser Ablation	16
2.3.2.2	Thermal Processes	20
2.4	Data Collection and Processing	21
I	Electronic and Infrared Spectra of Actinide Compounds Isolated in Solid Ar	24
3	Introduction to Actinide Spectroscopy	25
3.1	Interests in Actinide Spectroscopy	25

3.2	Theoretical Treatment of Actinides	29
3.2.1	Ligand Field Theory.	29
3.2.2	Other Theoretical Approaches	34
3.3	Matrix Effects in Heavy-Metal Spectroscopy	37
4	Uranium Dioxide (UO₂)	39
4.1	Introduction	39
4.2	Experiment Details	41
4.3	Results	42
4.3.1	Fixed Wavelength Excitation	42
4.3.2	Tunable Wavelength Excitation	44
4.4	Analysis and Discussion	45
4.4.1	Conclusions	56
5	Uranium Chlorides	58
5.1	UCl ₄ and Its Chemical, Physical, and Spectra Properties	59
5.2	Experiment Details	60
5.3	The Uranyl Ion and the Oxidation of UCl ₄ to Form UO ₂ Cl ₂	63
5.4	Further Experiments	64
5.4.1	IR Absorption Spectra	64
5.4.2	Fixed Frequency Excitation	65
5.4.3	Tunable Excitation	68
5.5	Analysis and Discussion	70
5.5.1	Long-Lived Fluorescence	70
5.5.2	Short-Lived Fluorescence	78
5.6	Conclusion	80
6	UO₃ and Higher Order Oxides	81
6.1	Introduction	81

6.2	Experiment Details	83
6.3	Results	84
6.3.1	Infrared Absorption Spectra	84
6.3.2	Fixed Wavelength Excitation	86
6.3.3	Tunable Excitation	88
6.4	Analysis and Discussion	90
6.5	Conclusion	94
7	Uranium Fluorides	96
7.1	Introduction	96
7.2	Experiment Details	98
7.2.1	Formation of UF_x by Passing UF_6 through a Microwave Discharge.	98
7.2.1.1	Preliminary Spectra of UF_6	99
7.2.2	Formation of UF_x by Mixing Ablated U with F_2	102
7.3	Results	102
7.3.1	Spectra for UF_x Products Generated by Passing UF_6 through a Microwave Discharge.	102
7.3.1.1	Fixed Frequency Excitation	102
7.3.1.2	Tunable Excitation	104
7.3.2	Spectra from the Formation of UF_x by Mixing Ablated U with F_2	107
7.3.2.1	Fixed Frequency Excitation	107
7.3.2.2	Tunable Excitation	107
7.4	Analysis and Discussion	109
7.5	Conclusion	112
8	The Search for the Electronic Spectra of Uranium Nitrides	114

8.1	Introduction	114
8.2	Experiment Details	116
8.2.1	IR Absorption	116
8.2.2	Fixed Frequency Excitation	119
8.2.2.1	Tunable Excitation	119
8.2.3	Visible Absorption	125
8.3	Determining the Fluorescing Species	126
8.4	Analysis and Discussion	129
8.5	Conclusion	131

**II Electronic and Infrared Spectroscopy of OH-Xe Isolated
in Solid Ar** **133**

9 OH-Xe **134**

9.1	Introduction	134
9.2	Experiment Details– Generating OH and Xe-OH	140
9.3	Results	141
9.3.1	IR Spectra	141
9.3.2	Fixed Frequency Excitation	142
9.3.3	Tunable Excitation	145
9.4	Analysis and Discussion	146
9.5	Conclusion	150

A A Note About Actinide Radioactivity **151**

B The Synthesis of Uranium Chloride **152**

Bibliography **154**

List of Figures

2.1	Experiment setup.	8
2.2	FTIR and UV / VIS setup.	9
2.3	The effect of purging with N ₂ on an IR background spectrum.	10
2.4	Cl ₂ fluorescence.	14
2.5	Microwave discharge setup.	15
2.6	Various laser ablation apparatuses.	18
2.7	Cu ₂ isolated in solid Ar.	20
2.8	Thermal vaporization apparatus.	21
3.1	Spatial extent of Nd ³⁺ and U ³⁺ valence wavefunctions.	28
3.2	Two Spin-orbit coupling schemes.	34
3.3	Correlation diagram for Group IVA elements.	35
4.1	ADF/PW91 linear transit energy curves for UO ₂ + 5Ar → UO ₂ (Ar) ₅ (D _{5h}).[6]	40
4.2	UO ₂ fluorescence induced by 266 nm radiation.	42
4.3	Visible UO ₂ fluorescence induced by 266 nm radiation.	43
4.4	25,942 cm ⁻¹ fluorescence induced by tunable radiation.	44
4.5	The phonon effect.	47
4.6	Spectrum of ablated U + ¹⁶ O/ ¹⁸ O (5/1) isolated in solid Ar.	49

4.7	Two possible electronic configurations for UO_2 to describe the UV emission.	53
5.1	Comparison of UCl_4 trapped in solid Ar with UO_2Cl_2 in acetone. . .	62
5.2	IR absorptions of thermally vaporized UCl_4 trapped in solid Ar. . . .	65
5.3	Fluorescence from thermally vaporized UCl_4 in solid Ar induced by 355 nm radiation.	67
5.4	Short-lived fluorescence induced by 308 nm radiation.	68
5.5	Fluorescence decay curves from thermally vaporized UCl_4 in solid Ar induced by 355 nm radiation.	69
5.6	Excitation spectrum of thermally vaporized UCl_4 trapped in solid Ar recorded by monitoring long-lived fluorescence.	71
5.7	Excitation spectrum of thermally vaporized UCl_4 trapped in solid Ar recorded by monitoring short-lived fluorescence.	72
5.8	Conversion reactions for U-O-Cl compounds and free energy at 900 K.	74
5.9	Energy level sketch of the absorption and fluorescence of UOCl_x . . .	77
6.1	Predicted geometry of UO_3 . [7, 8]	82
6.2	IR absorption spectra for ablated $\text{U} + {}^{18}\text{O}_2/{}^{16}\text{O}_2$ (1/5) in Ar.	85
6.3	Enlargement of the $(\text{UO}_2)^{2+}(\text{O}_2)^{2-}$ stretching region.	85
6.4	Enlargement of the $(\text{UO}_2)^{2+}(\text{O}_2)^{2-}$ stretching region.	86
6.5	Long-lived fluorescence from ablated $\text{U} + 1\% \text{O}_2$ in Ar induced by 308 nm radiation.	87
6.6	Lifetimes of fluorescence from ablated $\text{U} + 1\% \text{O}_2$ in Ar.	87
6.7	Excitation spectra of ablated $\text{U} + 1\% \text{O}_2$ in Ar recorded monitoring long-lived fluorescence.	89
7.1	The geometry of UF_5	97
7.2	Visible fluorescence from UF_6 induced by 355 nm Radiation.	99

7.3	Fluorescence from UF ₆ , passed through a discharge and frozen in Ar, induced by 355 nm radiation.	103
7.4	Excitation spectra of UF ₆ , passed through a discharge and frozen in Ar recorded by monitoring 21,277 cm ⁻¹ fluorescence.	105
7.5	Excitation spectra of UF _x in Ar recorded by monitoring 20,408 cm ⁻¹ fluorescence.	106
7.6	Fluorescence from ablated U + 0.5% F ₂ in Ar induced by 355 nm radiation.	108
8.1	IR absorptions of ablated U + 1% O ₂ in Ar.	115
8.2	The geometry of UN ₂	115
8.3	IR absorption spectra for U+ 1% N ₂ in Ar.	117
8.4	Fluorescence from U + 1% N ₂ in Ar induced by 355 nm radiation. . .	120
8.5	Fluorescence from U + 1% N ₂ in Ar induced by 266 nm radiation. . .	121
8.6	Excitation spectra of U + 1% N ₂ in Ar recorded by monitoring 15,924 cm ⁻¹ fluorescence.	122
8.7	Fluorescence from U + 1% N ₂ induced by 21,673 cm ⁻¹ radiation. . .	123
8.8	15,924 cm ⁻¹ fluorescence induced by 21,739 cm ⁻¹ radiation.	124
8.9	Visible absorptions of U + 1% N ₂ in Ar.	125
8.10	IR spectra for U + N ₂ in Ar.	127
8.11	IR spectrum for U + D ₂ in Ar.	128
8.12	Fluorescence from Cu + 0.5% D ₂ in Ar induced by 355 nm radiation.	129
9.1	Fluorescence from various OH containing species.[5]	135
9.2	Xe-OH ground state potential energy surfaces.[9]	138
9.3	Fluorescence from Xe-OH induced by exciting OH A ² Σ ⁺ → X ² Π(0,0).	139
9.4	Infrared spectrum of discharged 0.5% O ₂ + 0.5% H ₂ in Ar.	141
9.5	Infrared absorptions of discharged 4.5% Xe + 0.5% O ₂ + 0.5% H ₂ in Ar.	142

9.6	Fluorescence spectra of discharged 0.5% H ₂ + 0.5% O ₂ + Xe in Ar induced by 308 nm radiation.	144
9.7	Fluorescence decay lifetimes of OH in Ar and Xe-OH in Ar.	145
9.8	24,550 cm ⁻¹ fluorescence from Xe-OH in Ar induced by tunable radiation.	146
9.9	Xe-OH(A)potential energy surface.[10]	149

List of Tables

4.1	Measured low-lying energy levels of UO_2 compared with theory. . . .	43
4.2	Measured and calculated vibrational frequencies for CUO . [11]	55
4.3	Theoretical predictions for the stretching vibrational frequencies of UO_2	56
5.1	UCl_x IR absorptions.	61
6.1	UV/visible bands from ablated $\text{U} + 1\% \text{O}_2$ in Ar.	90
6.2	Comparison of experimentally observed $(\text{UO}_2)^+(\text{O}_2)^-$ vibrations with theory.	94
7.1	Peak assignments for UF_6	101
7.2	Fluorescence lifetimes for UF_6 , passed through a discharge and frozen in Ar.	104
7.3	IR absorptions of $\text{U} + \text{F}_2$	110
8.1	Summary of the IR absorptions for $\text{U} + 1\% \text{N}_2$ in Ar.	118
8.2	Summary of $\text{U} + 1\% \text{N}_2$ in Ar Fluorescence.	124
9.1	Experimentally determined vibrational constants for Rg-OH.	134
9.2	Radiative lifetimes and emission band centers for (0,0) emission from different OH containing species.	137

Chapter 1

Introduction

As the broad language in the title suggests, the molecules studied in this work are comprised of several different types, ranging from heavy actinides to rare gases complexed with radicals. While seemingly very different, there are some common underlying themes in the spectroscopy of both types of molecules stemming from the interaction between a rare gas and sample molecule. Before exploring the spectroscopy of these molecules, Chapter 2 introduces the reader to matrix isolation (MI) spectroscopy, the common technique used to investigate both types of molecules. From there, the dissertation is divided into two main parts. Part I focuses on the electronic spectroscopy of matrix isolated actinides using laser induced fluorescence (LIF) spectroscopy, with IR spectroscopy used as a complimentary technique to aid in the interpretation of the electronic spectra. Chapters 3-8 discuss the various actinide compounds studied in this program and provide an introduction to actinide spectroscopy. Part II deals with the spectroscopy of rare gas-radical (Rg-X) complexes, specifically OH-Xe.

1.1 Actinide Spectroscopy

Actinide chemistry has been studied for approximately two centuries. In more recent times, since the Manhattan project of the 1940's, much attention has been focused on using actinides to produce energy both for domestic power and atomic weapons. While much of the attention surrounding actinides has dealt with nuclear power, there are many other useful applications of actinides, some of them being very recent developments. For example actinides have long been used to make the sensors in smoke detectors and other electronic devices. And, researchers now have begun to explore the role of actinides in the future of nanotechnology. With so many uses of actinides, it is necessary to understand the electronic structure of actinide containing compounds both for the treatment of nuclear waste and the development of novel uses of actinides.

From a theoretical standpoint, researchers would like to develop models with accurate predictive properties for actinides. Before such models are developed, calculations for the simplest of actinide compounds need to be verified, preferably by comparing the results obtained from the calculations with those from gas-phase experiments. While the spectroscopic properties calculated for some actinide containing molecules are in agreement with experimental results, there is no model which will produce accurate results for all heavy metals, creating a need for further testing of the calculations. Unfortunately, experimentally obtained gas-phase electronic spectra for actinides are very sparse because the f orbitals in actinides result in a multitude of low-lying electronic states, thus making gas phase spectroscopy more difficult for actinides than lighter metals. Most of the data that does exist are IR or low resolution ultra violet (UV) / visible (VIS) absorption spectra for matrix isolated actinide species. Artifacts of MI spectroscopy such as the relaxation of selection rules makes this spectroscopic technique advantageous for heavy metals, as will be explained in Chapters 2 and 3.

As an alternative to gas phase data, scientists would like to use the available matrix data to validate their calculations if MI spectra for actinides show the same behavior as MI spectra for molecules consisting of lighter elements. When light molecules were studied in the early days of MI spectroscopy, it was shown that the matrix host material did little to perturb the spectra causing at most tens of wavenumber shifts in vibrational frequencies. However, experimentalists recently have demonstrated that the magnitude of the interaction between a heavy sample molecule and a rare gas matrix host is much stronger than first thought. This unusually large interaction causes shifts in the spectra which people referred to as matrix shifts. An underlying theme in this work on actinide spectroscopy is to understand the nature of these interactions and determine if MI data is acceptable for testing theoretical predictions for gas-phase actinide containing molecules.

The experiments described in Part I are an attempt to gather more electronic structure information on actinides. Chapter 3 goes into more detail concerning the goals of the matrix isolated actinide spectroscopy project, as well as discussing some of the challenges of actinide spectroscopy. This chapter also explains what makes actinides so different from d-block transition metals. Chapters 4-8 discuss the specific molecules studied and the data collected, with a specific focus in Chapter 4 on the matrix shifts for actinide containing molecules coordinated with Ar.

1.2 Rare Gas Radical Complexes

What is of interest in the Rg-X complexes (where Rg represents the rare gas and X stands for a radical such as OH) is that the strength of the interaction between the Rg and X gets larger as one varies the Rg down the periodic table. For over half a century, researchers have known that the interactions between molecules and Xe are

much different than the interactions between the same molecules and the lighter rare gases. The varying interaction strengths between Rg and X when Rg is varied from Ne to Xe enable these systems to serve as test systems for studying the evolution from weak intermolecular physical interactions such as van der Waals forces to more "chemical-like" interactions.

However, while Xe-OH is a very interesting species, no gas-phase spectra for the complex have been reported. Part II of the dissertation examines the spectroscopy of Rg-X complexes with a focus on Xe-OH, gives some brief background on Rg-X complexes and why they are of interest, and discusses the spectroscopic results of the investigation on Xe-OH isolated in solid Ar. Both UV / VIS fluorescence and IR absorption spectroscopy were used for this investigation. What is so interesting about the spectrum of Xe-OH is that while most of the OH-Rg compounds that have been studied over the past two decades show a physical interaction between the Rg and OH in both the ground and excited states, the interaction between Xe and the Rg in the excited state is more "chemical-like." The experiments presented in Chapter 9 are a companion to current gas phase experiments.

Chapter 2

Introduction to Matrix Isolation

Spectroscopy

Matrix isolation (MI) spectroscopy dates back to Vegard's studies in the 1920's, but the name was first coined by Whittle *et al.* and Becker and Pimentel[12, 13] in 1954. Originally, the technique was limited to highly specialized research laboratories. But now, it is a much more common laboratory technique and is as widely available as more common spectroscopic techniques. To date, there are many books that give detailed descriptions of MI spectroscopy and the general technique will not be discussed here.[13, 14] What this chapter will discuss is some of the benefits for using matrix isolation spectroscopy to study the species presented in this work as well as highlight the particulars of the matrix isolation setup used to collect the spectra presented here.

2.1 Why is Matrix Isolation Spectroscopy Useful?

MI spectroscopy has several advantages over gas phase spectroscopy: (a) the ability to study, at leisure, unstable molecules and ions because they are frozen in the ma-

trix, (b) the matrix host (usually Ar or Ne) is an inert gas and does little to perturb the sample molecules, (c) the ability in most cases to prevent thermal-rotational and vibrational excitation, especially when the sample molecules are formed at high temperatures as in the case of matrices containing metal oxides, (d) the ability to study diffusion over time by slowly warming the matrix near its melting point, (e) the relaxation of selection rules for electronic transitions of species trapped in a matrix.[13] Point (d) is useful in determining the composition of sample molecules in the matrix when reactive fragments were initially trapped in the host. Because most non resonant transitions for gas-phase heavy metals are very weak, point (e) is extremely useful for obtaining their electronic spectra. In MI spectroscopy, one can excite heavy metals with fixed frequency UV light and observe fluorescence bands. These bands can then be investigated further using tunable radiation to produce a low resolution spectral map. The spectra are called “low resolution” because no rotational information is present. The abundance of low-lying electronic states would hinder in the gas-phase search for a suitable resonant transition to investigate. The unavoidable thermal population in gas-phase spectroscopy would hinder in the assignment of spectral features because of the multitude of electronic states. Additionally, when the work presented here first began, the idea was to use this map to guide gas-phase spectroscopic studies in which more complete spectra containing rotational information could be recorded. The premise for this idea was the assumption that the rare-gas matrix host does little to perturb the spectra, a premise which had been observed previously for light molecules. However, as will be a theme in the following chapters, this assumption may not be valid for heavy molecules.

Another useful application for MI spectroscopy is the ability to measure directly, ground electronic state vibrational frequencies. Since its invention, one of the major applications of MI spectroscopy was the study of light radicals and reactive species, often using IR spectroscopy. It was found that vibrational frequencies measured

for matrix isolated samples agreed with gas phase measurements to within tens of wavenumbers. Later, when researchers began using MI spectroscopy to study heavy metals such as actinides, unexpected vibrational frequency shifts on the order of 100 cm^{-1} relative to the gas phase were observed. Such variation in perturbations by the matrix host is of considerable interest and also will be discussed in the chapters that follow.

Finally, let us examine the other benefits of MI spectroscopy. Another advantage is the ability to study reactive and unstable species at leisure. In gas phase experiments, once the experimental conditions are optimized one has to record the desired spectra immediately. If one were to return the following day, the experimental conditions could need re-optimizing. In MI spectroscopy, the sample is frozen in a cryogenic matrix and changes only minimally over time. Additionally, large amounts of sample molecules can be frozen in the matrix so that fluorescence can be observed, even from molecules with poor fluorescence quantum yields. And, with the relaxation of selection rules, what would usually be a weak or forbidden transition may now be allowed. Consequently, molecules can be studied without as much experimental optimization as in gas phase fluorescence spectroscopy.

2.2 Experiment Setup

Figure 2.1 shows a schematic of the entire experiment setup. The details of this matrix isolation refrigerator setup are described in reference[15]. But for completeness a brief description will be presented here. A matrix was formed by flowing gaseous sample molecules diluted with a rare gas onto a cold (12 K) copper mirror or CsI window under vacuum (10^{-6} torr). Section 2.3 describes in detail how matrix precursors (gaseous and solid) are prepared. Fluorescence was induced by ei-

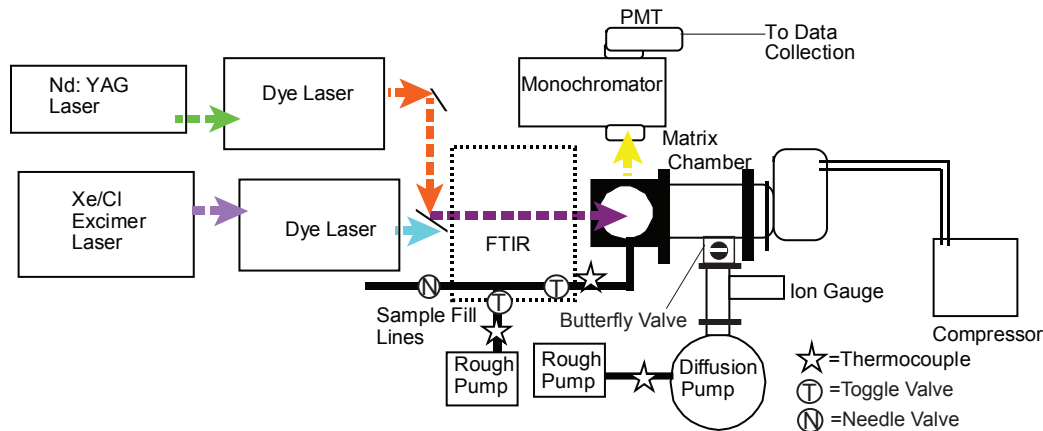


Figure 2.1: Experiment setup. An FTIR spectrometer, a butterfly valve, and a second rough pump have been added since the time of reference[15].

ther an excimer-pumped dye laser system (Lambda Physik EMG101/FL302E) or an Nd:YAG-pumped dye laser system (Quanta Ray DCR2A/PDL1). The fluorescence was dispersed by a 0.64 m monochromator (ISA, 120 line/mm grating) and detected by a photomultiplier tube (Electron Tubes Ltd. 9805QB). Signals were recorded with a digital oscilloscope (Tektronix TDS 2014) or a boxcar integrator (SRS model 250) connected to a computer. A Digi Lab FTS 3000 Excalibur spectrometer was to record IR absorption spectra. A butterfly valve placed between the chamber and the diffusion pump allowed the chamber to be isolated from high vacuum. During warm-up, when a matrix was released, a second rough pump removed the resultant gas through the sample fill lines, which saved time because the diffusion pump did not need to be turned off.

Probably the most important addition to the apparatus since reference [15] was the FTIR spectrometer which complimented the fluorescence capabilities of the current set-up by recording IR spectra. The IR spectrometer was setup for an external beam configuration. IR radiation was focused through the top of the matrix unit and sent into a detector resting on the laser table below as shown in Figure 2.2. When IR spectra were taken the copper disk was replaced with a CsI window to allow transmission of the IR radiation. This window will be described in more detail

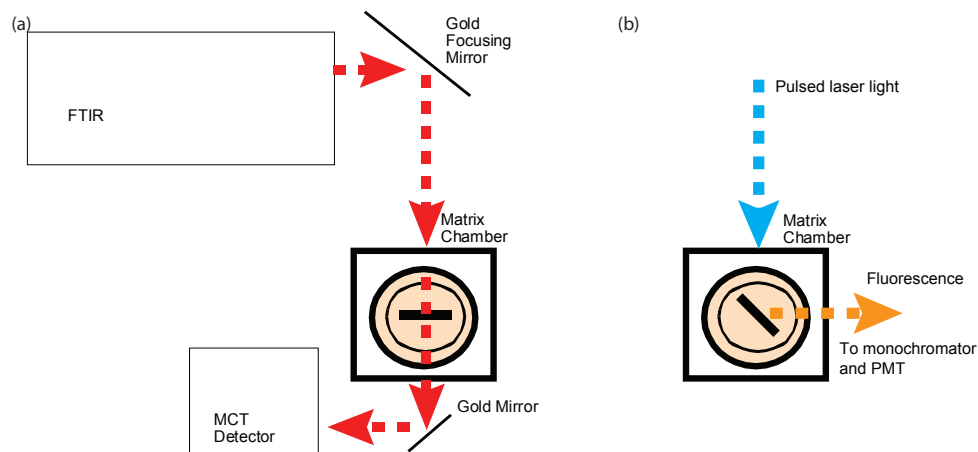


Figure 2.2: FTIR and UV/VIS setup. (a) Drawing showing the external beam configuration for the FTIR spectrometer. (b) Drawing showing the substrate position for UV / VIS fluorescence measurements.

in Section 2.3.2.1. A purge box was constructed from Lexan to reduce background absorptions from water or any other components of air because the IR radiation traveled a considerable distance outside of the spectrometer. Figure 2.3 shows a background spectrum for both purged (black) and unpurged (purple) conditions. It is evident how much the background absorptions are reduced by purging and the necessity for purging in our IR experiments. Some of the IR spectra presented here were taken before the construction of the purge box and will be noted accordingly.

All matrices were made from an effusive flow of gas mixtures onto the cold substrate at a rate of approximately 3 mmol / h. Typical deposition times were from 3-4 h. During the deposition process the cold trap above the diffusion pump was filled with liquid N_2 to freeze any impurities from back streaming onto the mirror and affecting the IR spectra. Keeping the trap filled with N_2 for the entire time a matrix was held on the substrate was not necessary because it had little effect on UV / visible fluorescence, which was the spectroscopic method used in the days after deposition. When an IR spectrum was recorded, a background spectrum of the cold CsI window was recorded just prior to deposition. After the matrix was deposited,

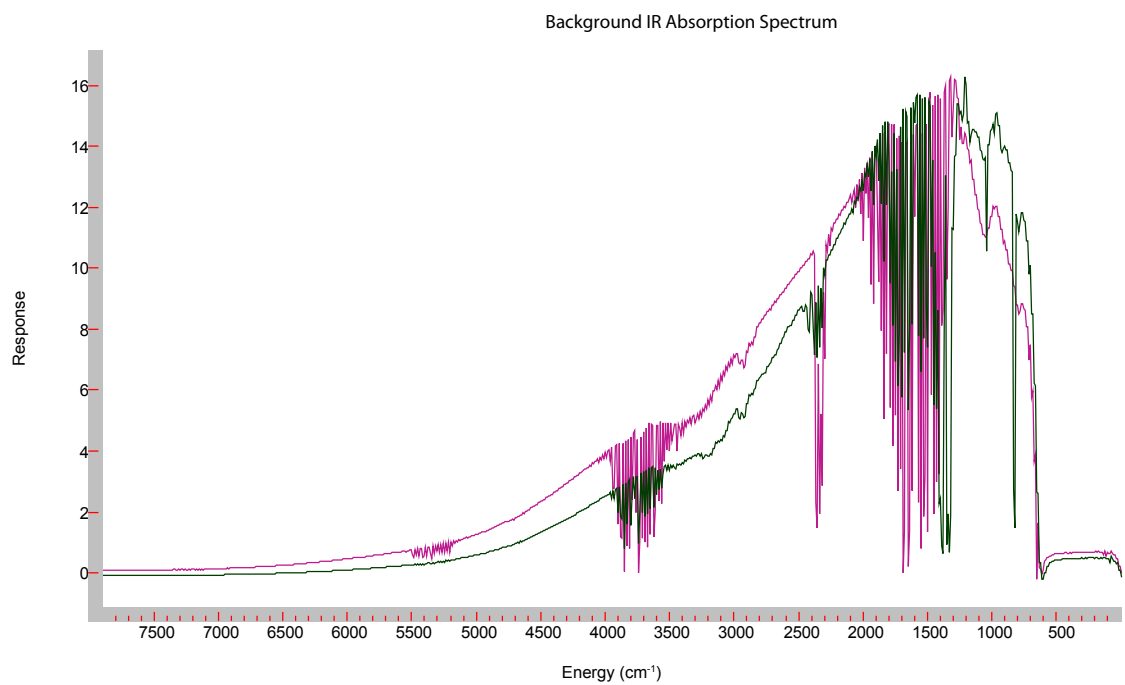


Figure 2.3: The effect of purging with N₂ on an IR background spectrum. The blue trace is the background recorded without purging. The black trace was recorded after purging both the external beam path and the spectrometer for a minimum of 30 minutes and clearly shows a decrease in the water absorptions.

a sample IR spectrum was recorded from which the previous background spectrum was subtracted. Following the sample IR spectrum, fluorescence spectra from fixed frequency and tunable excitation were recorded. Figure 2.2 (b) shows the configuration of the substrate used for recording UV / VIS spectra. If any photolysis or annealing experiments were performed, a new sample IR spectrum was recorded both immediately before and after these experiments because the IR throughput degraded rapidly with time. The next section will discuss how sample precursors for matrices were made. The term sample precursor refers to the molecules used to produce the sample molecules of interest frozen in Ar.

2.3 Sample Preparation

In the studies reported here, there are two main types of sample precursors used for the sample molecules frozen in an Ar matrix. The first type is any molecule that is gaseous at room temperature. The second type are molecules that are solid at room temperature and do not have sufficient room temperature vapor pressure to make it into a matrix in concentrations great enough to produce observable fluorescence. There is no magic number as to what the vapor pressure has to be in to order observe fluorescence, as fluorescence is dictated by the fluorescence quantum yield. If however, the vapor pressure is too low to trap enough sample in the matrix, then some heating or other vaporization process is necessary. The prior (precursors with high vapor pressure) will be discussed first because it is easiest to prepare a matrix from these precursors.

2.3.1 Room Temperature Gaseous Samples

Gaseous samples were prepared in either a 2 L glass gas collection flask or a 100 L small gas cylinder. The cylinder was ideal if sample precursors were abundant because a constant backing pressure could be maintained throughout the entire deposition, thus insuring a constant deposition rate without any valve adjustment. Often times when using the glass flask, the backing pressure would drop, and a valve adjustment was necessary to maintain a constant flow rate. For many sample precursors it was not practical to use the amount of precursor necessary to fill a cylinder.

The gas collection flasks contained a cold finger to either purify the sample precursor or control the vapor pressure during deposition. They were filled using a glass Walter's vacuum manifold (available from Ace Glass—not shown) connected to a Welch Chemstar mechanical pump with an ultimate vacuum of 0.1 mtorr. This pump was designed to handle the corrosive gasses in the higher concentrations used in sample preparations. Pressure in the manifold could be read to within a torr. First, the sample gas was added to the flask. If it contained impurities, it was purified by freezing it in the cold finger of the flask while pumping on the manifold. After pumping, the gas was allowed to warm to room temperature. Three of these cycles were usually sufficient to purify the gas. Second, the pressure inside the flask and manifold were adjusted so that when the Ar was added, one would have the proper sample concentration in Ar. Finally, Ar was added to bring the pressure inside the flask to near atmosphere. The pressure inside the flask was kept slightly negative to prevent the hollow ground glass vacuum stopcock on the flask from leaking.

Gas cylinders were prepared in a similar manner, but a brass gas mixing manifold replaced the glass one used for the flasks. A regulator was connected to the end of the manifold to read the pressure and to release the high gas pressures which built up in the manifold during cylinder preparation. A Welch Duo-Seal pump with an ultimate vacuum of 0.1 mtorr was used to evacuate the cylinder and manifold. The

total pressure inside the prepared cylinder was typically 1000 psi. Sample gases were added in order of increasing pressure. When the Ar was added, the Ar cylinder was connected directly to the manifold without a regulator.

2.3.1.1 Cl₂ Shakedown Experiments

Before work on this project was undertaken, the MI unit described above was in storage. The visible fluorescence spectrum of matrix isolated Cl₂ is useful in testing the cooling capabilities of the refrigerator. Such a spectrum was recorded and compared with the literature spectrum.[16] As shown in Figure 2.4, the fluorescence spectrum shows a Cl₂ ground electronic state vibrational progression. Bands five through ten are labeled in the spectrum. Each peak in the spectrum is a doublet with the lower intensity feature on the blue side corresponding to Cl₂ monomer and the dimer corresponding to the red shifted taller peak. A Cl₂ monomer is one Cl₂ molecule surrounded by Ar, and a Cl₂ dimer is two Cl₂ molecules, interacting with each other, surrounded by Ar. There should be a broad feature on the red edge of each band corresponding to higher order clusters of Cl₂. However, when making a matrix with a low concentration of Cl₂ primarily monomers and dimers are formed. As for using the spectra to test the refrigerator, if the refrigerator is not holding a constant low temperature around 12 K, Cl₂ molecules can congregate around one another forming higher order clusters in the matrix because the relative interaction strengths between two Cl₂ molecules is stronger than between Cl₂ and Ar.

2.3.1.2 Using a Microwave Discharge to Fragment Samples

As discussed in Section 2.1 MI spectroscopy is convenient for studying reactive species. To form such species from gas phase molecules, it is useful to pass either the matrix

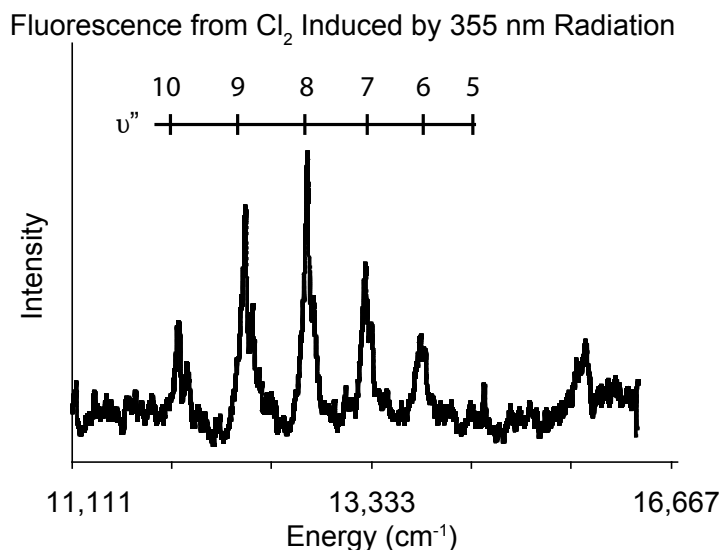


Figure 2.4: Cl₂ fluorescence. The fluorescence was induced by 355 nm light from a Nd:YAG laser. Splitting in each peak corresponds to the Cl₂ monomer and dimer, with the dimer being red shifted. The spectrum shows the $v(5) - v(10)$ bands.

host or the mixture of host and sample precursor through a microwave discharge cavity prior to deposition. The former is a “less harsh” way of fragmenting the sample, whereas the latter tears up the sample more. For the spectra for UF_x ($x < 6$) fragments isolated in Ar discussed in Chapter 7, a mixture of UF₆ and Ar was passed through a microwave discharge. Also, to form radicals from tightly bound molecules such as the formation of OH from water as described in Chapter 9, vacuum ultraviolet light, produced by the discharge is necessary. The problem with using a microwave discharge to form fragments is that there is limited control over what fragments are formed. This problem will be discussed in more detail when interpreting spectra in later chapters.

Figure 2.5 shows the specific details of the microwave discharge apparatus. The cavity of a microwave discharge power generator (Raytheon PGM-20 Series) was attached to a 1/2” OD glass tube inserted in the sample fill line. A brass plate with an O-ring sealed compression fitting connects the tube to the chamber. An O-ring

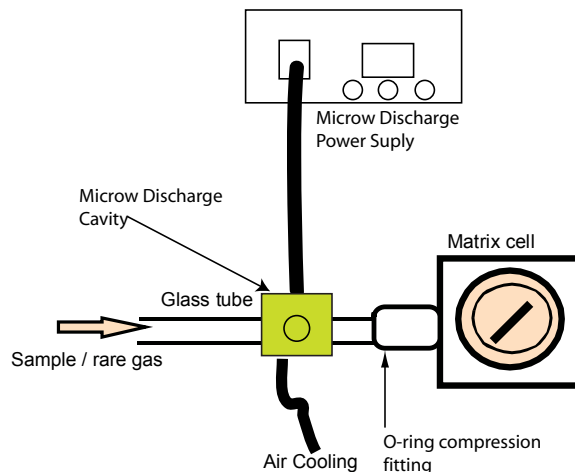


Figure 2.5: Microwave discharge setup. Note that the glass tube is restricted at the matrix end with a 1mm orifice to create enough gas pressure to sustain a discharge.

sealed compression union connects the other end of the tube to the fill line (not shown). The cavity is positioned on the tube as close to the chamber as possible without making contacts with the fittings. This position of the cavity provides the shortest path for the very reactive fragments to reach the substrate. Consequently, there is less of a chance of recombination and other processes before the fragments are frozen in the matrix. The glass tube is restricted at the matrix end with a 1mm orifice to create enough gas pressure to sustain a discharge. Compressed laboratory air was used for cooling the discharge cavity. When using the apparatus, the gas flow through the cavity was adjusted so that there were several milliliters of gas inside the glass tube. The power for the discharge was set to under 17 W, and the cavity was aligned for minimal reflectance which was around 2 W to prevent damage to the discharge power supply.

2.3.2 Room Temperature Solid Samples

Solid sample precursors are inherently harder to work with because they must be converted into a vapor before mixing with the rare gas during deposition. For metal precursors in the form of rods or disks, pulsed-laser vaporization is often used to ablate the metal. For powdered precursors, they are often heated to temperatures high enough to achieve a suitable vapor pressure to obtain adequate sample concentration in the matrix. Both of these techniques were used in this work and will be discussed in the next two sections.

2.3.2.1 Laser Ablation

Atoms from a solid piece of metal are ablated when a powerful laser beam is focused on the surface. Typically, either the fundamental or first harmonic (532 nm) from a pulsed Nd:YAG laser is used, though in some cases the second harmonic is more suitable than the first. For most of the experiments here, green laser-light was used because the IR of the fundamental is invisible to the naked eye posing a potential safety risk, though for some metals the second harmonic (355 nm) light was used to avoid such risks. When the light hits the metal surface, it forms a very hot and reactive plasma. A plume of metal atoms will come off in a direction perpendicular to the surface. These atoms are allowed to mix with an effusive gas flow before sticking to the matrix substrate. If the flow contains gases other than rare gases, the plasma is hot enough to cause reactions.

In his experiments with matrix isolated iron oxides, Michel Macler, a former member of the Heaven group, used a laser ablation apparatus made from a modified O-ring sealed compression tee similar to the one shown in Figure 2.6 (a).[15] A hole was bored in the center of the tee, and a microscope slide was epoxied there as a window to allow the laser to reach the target. A 1/2" OD glass or Cu tube connected the tee to

the matrix chamber via a brass plate retrofitted with a 1/2" ID O-ring sealed compression fitting. Because there is no motion of the metal target in this setup, the position of the focused YAG laser had to be moved constantly in order to maintain a plasma above the metal surface. Macler claimed this "freehand" movement of the beam caused some uncertainty in the concentration of the metal mixed with the rare gas making experimental data hard to reproduce, though all the results presented here were easily reproduced. In the more recent experiments presented here, a second flaw was discovered in the design of this apparatus. Because the mixture of the ablated metal and rare gas traveled through a narrow 1/2" OD glass or Cu tube at least 3" in length before reaching the substrate, a majority of the matrix isolated species collided with the walls of the tube and never made it to the substrate.

While some of the preliminary experiments to the work presented here used Macler's laser ablation apparatus, it was replaced with a different apparatus shown in Figure 2.6 (b) for the first of the experiments presented here. The new apparatus bolted directly to the chamber and eliminated the narrow coupling tube. The ID of the ablation cell matched the 1 1/2" window openings on the matrix chamber, which reduced the probability of the ablated atoms colliding with the cell before deposition. The cell was soldered directly to a brass plate so that it could couple directly to the matrix chamber. While this apparatus was an improvement over the prior design, it was still hard to trap heavy metals in the matrix for two main reasons. First, the direction of the vaporization beam would create a plume of metal atoms with the greatest velocity upwards towards the ablation window and not the cold substrate. Secondly, the target was still approximately 3" away from the substrate. A final design shown in Figure 2.6 (c) was created to fix the two flaws of the apparatus in (b). The design closely resembles the ablation setup used by Lester Andrews and positions the ablation source inside the shroud of the matrix chamber.[17] In this setup a sample rod was placed within a 1/2" of the matrix substrate. Soft steel was attached to the

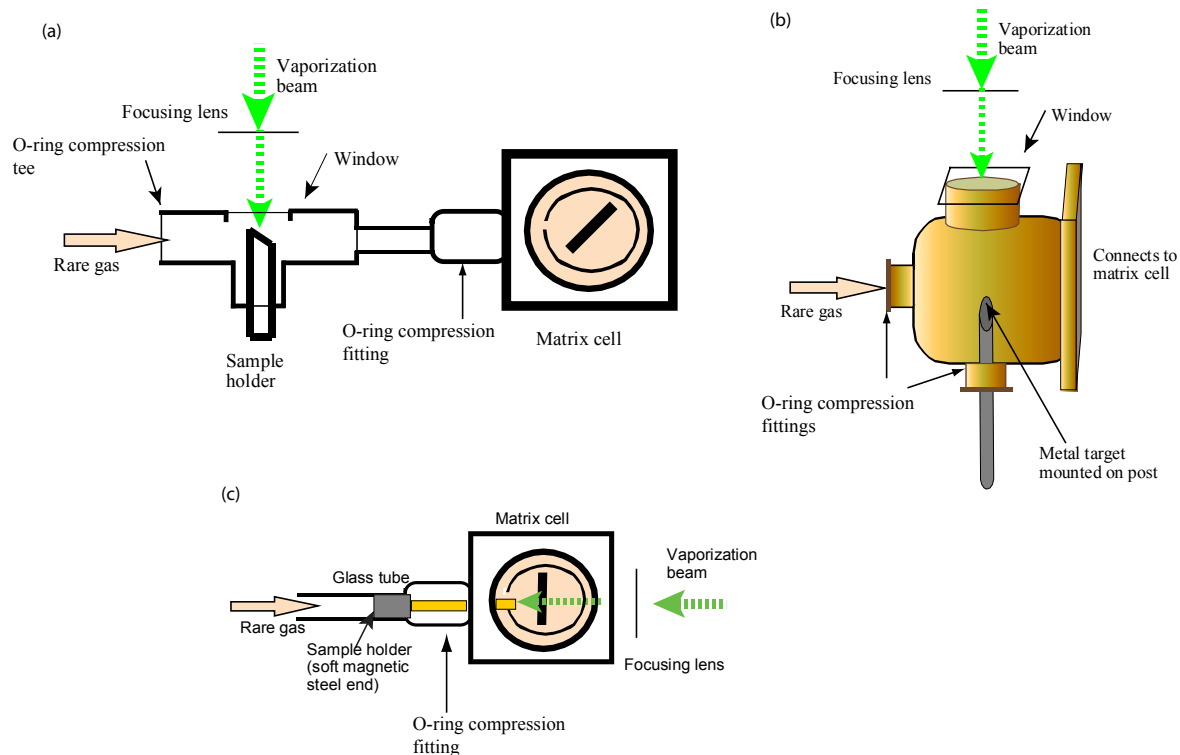


Figure 2.6: Various laser ablation apparatuses. (a) Shows the modified 1/2" ID O-ring compression tee used by Macler.[15] (b) Shows a new vaporization apparatus used because of the problems associated with the design in (a), this new vaporization cell was used. (c) shows a third apparatus constructed to fix the problems associated with (b), which follows a design used by Lester Andrews at the University of Virginia.[17].

back end of the rod to allow movement by a magnet so that the target could be moved outside the shroud, thus allowing the cold substrate to be rotated after deposition to obtain the various spectra. A 1/2" OD glass tube was attached between the sample fill line and the matrix chamber to hold the metal rod after deposition. A 1/16" hole was drilled in the CsI substrate to allow focused laser light to pass through. (CsI is soft enough that a hole can be drilled with fracturing the material). Light from the YAG laser was focused through the CsI onto the metal rod. The majority of the ablated metal atoms came off moving towards the substrate. This setup increased the number of metal atoms sticking to the substrate so a greater flow of matrix host gas was necessary. For some of the uranium experiments, a pure uranium rod was used. For all other ablation experiments, the sample metal precursor was attached to the end of a brass rod using high vacuum wax (Dow Corning) or epoxy (Hardman). All the ablation experiments discussed in this work which were performed after the acquisition of the FTIR used the ablation apparatus labeled (c) in this figure.

Cu Shakedown Experiments:

In order to test our laser ablation apparatus, spectra of Cu_2 and CuO were recorded because there was difficulty in reproducing the spectra of uranium oxides recorded several years earlier in the Heaven group. The fluorescence spectra of Cu_2 and CuO previously were published in the literature and were better understood than those of similar uranium compounds. Figure 2.7 shows the spectrum for Cu_2 isolated in solid Ar recorded during the course of this work. The matrix was made by ablating a piece of Cu metal from a gasket used in the vacuum system with the 532 nm light from the Nd:YAG laser. 0.5% D_2 was added to the carrier gas to favor dimer over oxide formation. There was no particular reason for using D_2 instead of H_2 other than it was more convenient at the time to prepare a flask with a D_2 / Ar mixture. The spectrum in the figure is in good agreement with the published spectrum by Mitchell, *et al.*[18] The spectra for CuO (not shown) were in equally good agreement with the

Fluorescence from Cu₂ Induced by 355 nm Radiation

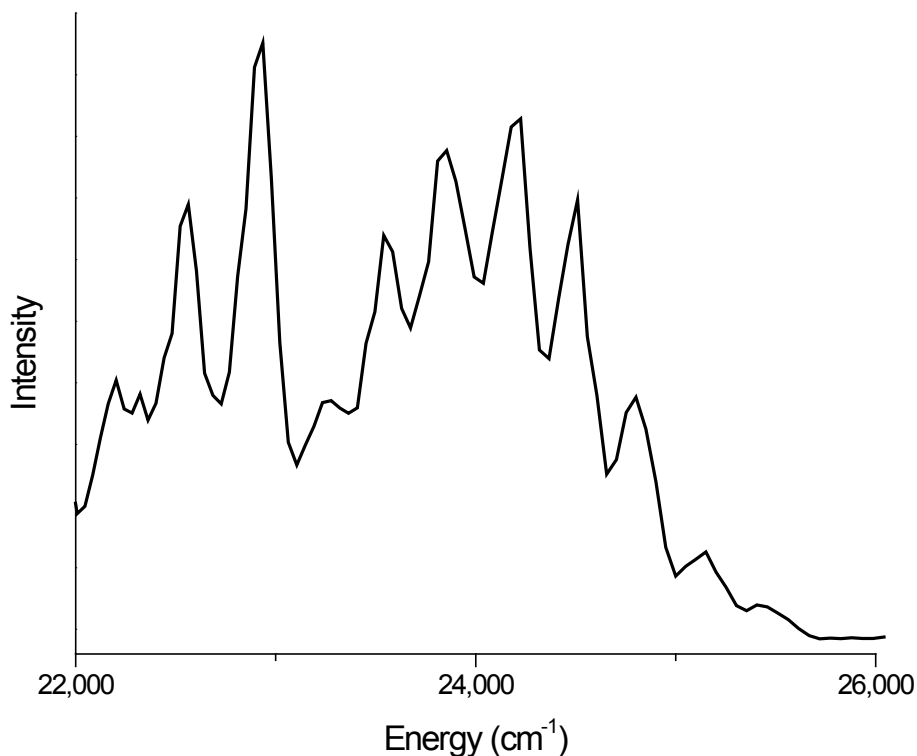


Figure 2.7: Cu₂ isolated in solid Ar. 0.5% D₂ was added to the carrier gas to favor dimer over oxide formation.

literature.

2.3.2.2 Thermal Processes

Refractory powders are not very suitable for laser ablation because of their physical nature. Heating these materials to high temperatures is often more effective. In order to work with powder sample precursors such as the UCl₄ discussed in Chapter 5, the apparatus shown in Figure 2.8 was used. 1/8" OD Cu tubing was wrapped around the O-ring compression fittings that seal the glass tube to the matrix chamber and sample fill line. Cooling water was flowed through the Cu tubing to prevent O-ring damage and leaking. Kalrez O-rings were used in the fittings because they could withstand

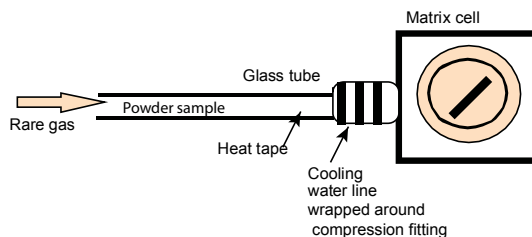


Figure 2.8: Thermal vaporization apparatus. This apparatus was used for vaporizing solid powders not suitable for laser ablation.

higher temperatures than the viton ones supplied with new fittings. Thermocouples (not shown), were used to measure the temperature of the glass tube wrapped in the heat tape as well as the external temperature of the O-ring compression fittings. The advantages of this apparatus were that it was easy to build and did not require a specialized furnace or Knudsen cell. As evident in the spectra shown in Chapter 5, it also worked. The downside to the apparatus was the inability to control the temperature accurately, which did not appear to be a major problem because matrices formed using this setup were reproducible based on the recorded spectra.

2.4 Data Collection and Processing

When this MI apparatus was first restored for the experiments discussed in this work, emission spectra were recorded using a boxcar integrator (Stanford Research Systems SR 250) connected to a personal computer (PC) with an analogue to digital converter (A/D) card (Measurement Computing PCI-DAS08). After recording many spectra, it was found that replacing the A/D card with a digital multimeter (HP 4100) interfaced to a computer by GPIB greatly improved the signal to noise ratio. Eventually an oscilloscope (TKTDS2014) was interfaced to the computer via GPIB to collect the data. In this case, the boxcar was not used, and data was processed inside

the computer. Both the boxcar and oscilloscope were triggered by either the thyatron sync output of the excimer laser or the Q-switch sync output of the Nd:YAG laser. Alternatively, a photodiode oftentimes was used as a trigger because there was a lot of jitter noise inherent in the sync output signals. Data collection was controlled using in house programs written with the LabVIEW programming package. For determining the lifetimes of decay curves, a fitting routine using the Levenberg-Marquardt theorem was used within LabVIEW or the data was exported to a data analysis package such as Origin.

Another important aspect of the data collection process was the integration of the PMT signal. When the oscilloscope was used to collect data, numerical integration was performed on the PC using the standard numerical integration subVI available in LabVIEW. The trapezoidal rule was used for integration. It is also of importance that the intensity (y) data downloaded to the PC was converted into actual absolute voltage prior to integration. By converting the y data into voltages the absolute intensity of peaks in different spectra could be compared directly once a simple baseline correction was made, regardless of the vertical resolution settings on the scope. However, there was no method to compare absolute peak intensities from two spectra when one was recorded with the boxcar and the other was recorded with the oscilloscope. Alternatively, the boxcar has a limited output range of ± 10 V, and it was necessary to adjust the vertical resolution of the boxcar so that the maximum output was not reached during integration. Therefore, absolute intensities of peaks in two spectra could not be compared unless the same vertical resolution was used, but the relative intensities of peaks in the same spectrum were meaningful. Of course the above discussion assumed that variables such as PMT bias were kept constant.

The experiment timing also was controlled by a personal computer. Subroutines written in LabVIEW were used to control both the ISA monochromator and the Lambda Physik dye laser. Specifically the monochromator was interface through the

serial port while the Lambda Physik dye laser was controlled by the digital outputs of the A/D card. There was no personal computer interface for the Quanta Ray dye laser, though scanning could be obtained using the MCI-1 dye laser controller. Unfortunately, the MCI-1 only operated in a continuous scanning mode. When scanning any instrument (laser or monochromator) in a continuous mode the box car and multimeter or A/D card were used to record data. A delay time based on the laser repetition rate and number of averages collected by either the oscilloscope or boxcar was used to ensure data was collected before the laser or monochromator grating was moved. For example, if the laser fired at 10 Hz, then a delay time of 3 s would be necessary for averaging 30 decays in the oscilloscope.

Part I

Electronic and Infrared Spectra of Actinide Compounds Isolated in Solid

Ar

Chapter 3

Introduction to Actinide Spectroscopy

3.1 Interests in Actinide Spectroscopy

Almost three quarters of a century ago, scientists discovered the neutron and nuclear fission. By 1943, the United States realized the potential of using such heavy atoms for weapons of mass destruction and embarked on the Manhattan project, led by a group of army scientists including Albert Einstein. This project has sparked interest in actinide chemistry through modern times. After the successful building of the atomic bomb, actinides were realized as a good source of domestic power. Coincidentally, actinides were used for domestic items such as the sensors in smoke detectors. Another item worth mentioning here is the promising new role of actinides in nanotechnology. Recently in 2006, scientists discovered a nanoparticle assembly mechanism used by bacteria to combat the toxic effects of actinide exposure.[19] In this mechanism, the bacteria assembled uranium or other actinides into nanocages, which prevented the actinides from harming the bacteria. This mechanism has allowed researchers to create a template for forming nanosized clusters of actinides. Additionally, scien-

tists have discovered the self assembling of actinyl peroxide nanospheres in uranium peroxide solutions.[20] These nanospheres automatically precipitated from solution in the laboratory. The ability to form nanoparticles from actinides is very intriguing because of their electronic, magnetic, and structural properties.

Returning to the topic of nuclear energy, one of the by-products of the Manhattan Project was the generation of large amounts of liquid radioactive waste, which is still present today. After the project ended, physicists continued to study the enrichment and fission processes heavily to maximize their energy harvesting capabilities. Traditionally, physicists separated radioisotopes used in nuclear reactors, e.g. uranium, by mass. However, during that time they carried out spectroscopic studies of uranium hexafluoride (the stable compound used in mass isotope separation) and its fragments in hopes of developing a new photochemical technique for separating the isotopes.[21, 22, 23, 24, 25, 26, 27, 1] However, after the accidents at Three Mile Island and other nuclear facilities, research on actinides was reduced because of public fear. Now, over half a century later, there is a renewed interest in actinides as a solution to providing clean energy to combat global warming and for novel uses. Scientists also know they must now find a solution for dealing with the nuclear waste remaining from the past endeavors such as the Manhattan Project. Specifically, scientist would like to be able to separate the radioactive metals from other metals in the waste. While the nonmetallic components of the waste such as HF and HCl are very dangerous, standard acid / base chemistry can eliminate their harmful effects.

One of the key questions researchers would like to understand about actinides is the role of f-orbitals in bonding. As one goes down the periodic table the atoms become more massive and have a greater nuclear charge. At the same time the added electrons do not shield the f electrons as efficiently, creating a greater effective nuclear charge than that caused by simply increasing the number of protons. For lanthanides, it has been found that the f-orbitals do not participate in bonding because of the

lanthanide contraction. The name lanthanide contraction comes from the fact that the f orbitals in lanthanide are contracted so much so that they do not participate in bonding. Coincidentally, the increased effective nuclear charge causes the valence electrons to move more rapidly around the nucleus. Specifically, a question researchers want to answer is whether the f orbitals in actinides are as contracted.

Back in 1995, Norman Edelstein wrote an article discussing the known differences in the electronic structure of lanthanides and actinides.[28] In the article, he states that the major difference between 4f and 5f electrons was that the 4f electrons were inert inner shell electrons, and as one moves across the lanthanide series, there is little change in the reactivity of the f-electrons. In the actinides, though, the 5f electrons are closer in energy to the 6d electrons, which do participate in bonding. However, as one moves across the actinide series the f-orbitals become more localized and play less of a role in bonding. A plot of the valence orbital distribution functions (plotted as intensities) as a function of distance from the nucleus for Nd^{3+} and the corresponding actinide, U^{3+} , taken from Edelstein's article is shown in Figure 3.1. Notice how the 5f orbitals are more delocalized than the 4f orbitals, giving them a greater potential for involvement in bonding. Also, notice how the spatial extent of s and p orbitals are almost identical in both lanthanides and actinides. However, the peaks of the 6s and 6p distribution functions are a little closer to the nucleus. The increased nuclear charge in actinides causes greater 6s and 6p character near the nucleus which means that there is less 5f character there and a greater spatial extension of the f-orbitals.[29] While the greater spatial extent of actinide f-orbitals is known, a question researchers want to answer is whether the f orbitals play a role in bonding.

Bursten and colleagues have proposed the "Feudal" model for describing actinide bonding.[30] "Feudal" is an acronym for "f's essentially unaffected, d's accommodate ligands." This model was created by comparing photoelectron spectroscopic studies with density functional theory calculations. Bursten found that, especially in organo

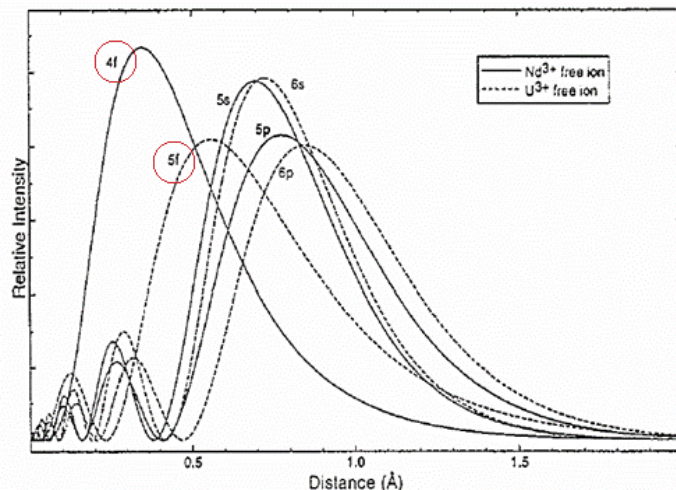


Figure 3.1: Spatial extent of Nd^{3+} and U^{3+} valence wavefunctions. Electron density is plotted as relative intensity.[28]

actinides, the actinide to ligand bond consisted of mostly 6d character and contained little of the U 5f orbitals. However, in the case of the highest occupied molecular orbital of Cp_3ThCl ($\text{Cp} = \eta^5 - \text{C}_5\text{H}_5$), which belongs to the C_{3v} point group, metal f orbital / ligand interactions are observed. Here, the Cp π_2 orbitals are of a_2 symmetry and are ligand-ligand antibonding. For a_2 symmetry, interactions between the actinide s, p, or d orbitals and the ligand are symmetry forbidden, while the interaction with the f-orbitals is allowed. Though the f-orbitals are usually not involved in ligand-actinide bonding (except for special cases such as the one above), Bursten's model proposed they do contain the 2 metal-localized electrons of U(IV) compounds. The spectroscopy of U(IV) compounds will be discussed further in Chapter 5. While this model provides a qualitative description of what is known so far concerning actinide bonding, there is so much more uncharted territory with regard to actinides, both experimental and computational, that a lot more studies are needed before researchers have a good understanding of the participation of the f-orbitals in actinide bonds.

Quantum-chemistry calculations now are reaching the point where they may accurately model simple actinide compounds and begin to answer some of the questions

concerning the electronic structure of actinides. A problem with current methods for calculations is that they are not generalized and must be tailored to specific molecules. Therefore, the results of such calculations must be validated with spectroscopic data. The most basic of these calculations describe single isolated molecules in the ground state, which are best studied experimentally using gas phase experiments at low pressures and temperatures. The problem is, however, that gas phase data are lacking. As the next best alternative, data from matrix isolation experiments have been used because the data are more plentiful and because such experiments directly probe the ground electronic state of molecules containing actinides. But, exactly how well do matrix spectra provide information about the properties of single isolated molecules? The rest of this chapter will discuss some of the challenges of actinide spectroscopy and some of the other questions the experiments discussed in Part I will try to answer, such as the strength of the interaction between actinide containing molecules and rare gases. For those wondering about the inherent risk associated with working with actinides, see the note about actinide radioactivity in Appendix A.

3.2 Theoretical Treatment of Actinides

3.2.1 Ligand Field Theory.

Often when one takes a qualitative look at bonding between a heavy metal and some ligand such as oxygen, one will find that the valence molecular orbitals (MO) are more like the orbitals of the free metal with small perturbations caused by the ligand(s). A simple model of metal-ligand bonding which primarily uses metal centered atomic orbitals (AO's) is called ligand field (LF) theory. In the model, interactions between the metal and the ligands are treated as Coulombic point charge interactions. For heavy metals a spin-orbit term is added to the Hamiltonian.

LF theory provides a traditional framework for an understanding of the electronic structures of transition metal compounds. While LF theory first was applied to transition metals, scientists now use it to describe lanthanide bonding because f-orbitals are not involved in bonding. However, it is still unclear if such a model will accurately describe actinides because of the possible participation of f-electrons in bonding. It is the f-electrons that make actinides challenging to study both experimentally and computationally. One of the main differences in a quantitative description of heavy metals compared to lighter transition metals is that spin-orbit coupling is strong, that is, the spin-orbit interaction is much stronger than the inter electron repulsion. (Spin-orbit interactions are greater than spin-spin and orbit-orbit interactions). A brief quantitative review of LF theory and spin-orbit interaction, taken from Levine's *Quantum Chemistry* [31] will be presented here. This description initially assumes a light atom, and then the differences for heavy atoms are described. For any atom the Hamiltonian can be written as follows:

$$\hat{\mathcal{H}} = \hat{\mathcal{H}}^0 + \hat{\mathcal{H}}_{rep} + \hat{\mathcal{H}}_{S.O.} \quad (3.1)$$

where $\hat{\mathcal{H}}^0$ is the sum of hydrogenlike Hamiltonians,

$$\hat{\mathcal{H}}^0 = \sum_{i=1}^n -\frac{\hbar^2}{2m_e} \nabla_i^2 - \frac{Ze'^2}{r_i}, \quad (3.2)$$

and $r_{ij} = (x_i^2 + y_i^2 + z_i^2)^{1/2}$, that is, the distance of electron i from the nucleus. The first term is the kinetic energy operator and the second term is the potential energy operator for an electron interacting with a nucleus. The $\hat{\mathcal{H}}_{rep}$ term describes inter-electronic repulsions caused by the interaction of the ligands with the central metal atom,

$$\hat{\mathcal{H}}_{rep} = \sum_i \sum_{j>i} \frac{e'^2}{r_{ij}} \quad (3.3)$$

where $r_i = [(x_i - x_j)^2 + (y_i - y_j)^2 + (z_i - z_j)^2]^{1/2}$, the distance between electrons i and j . $\hat{\mathcal{H}}_{S.O.}$ is the spin-orbit interaction term:

$$\hat{\mathcal{H}}_{S.O.} \approx \frac{1}{2m_e c^2} \sum_i \frac{1}{r_i} \frac{dV_i(r_i)}{dr_i} \hat{\mathbf{l}}_i \cdot \hat{\mathbf{s}}_i = \sum_{i=1}^n \xi_i(r_i) \hat{\mathbf{l}}_i \cdot \hat{\mathbf{s}}_i \quad (3.4)$$

where the $\xi_i(r_i)$ term describes the magnetic field felt by electron i as it moves through the electric field generated by the nucleus, which is based on the Coulombic potential, $V_i(r_i)$. $\hat{\mathbf{l}}_i$ and $\hat{\mathbf{s}}_i$ are the angular orbital momentum and spin orbital momentum operators for electron i and will be discussed more below. The spin-orbit energy for an one electron atom can be written as:

$$E_{S.O.} \approx \langle \psi | \xi(r) \hat{\mathbf{l}} \cdot \hat{\mathbf{s}} | \psi \rangle \quad E_{S.O.} \approx \frac{1}{2} \langle \xi \rangle \hbar^2 [j(j+1) - l(l+1) - s(s+1)] \quad (3.5)$$

For a many electron system, Bethe and Jackiw[32] showed that the spin-orbit interaction energy could be written as:

$$E_{S.O.} \approx \frac{1}{2} \gamma_{LS} \hbar^2 [j(j+1) - l(l+1) - s(s+1)] \quad (3.6)$$

where,

$$\gamma_{LS} = \sum_i \alpha(i) \beta(i) \quad (3.7)$$

and

$$\alpha(i) = \langle l || l_i || l \rangle$$

$$\beta(i) = \langle s || s_i || s \rangle. \quad (3.8)$$

In a classical picture, $\hat{\mathbf{I}}$ can be defined by the following:

$$l_x = yp_z - zp_y \quad (3.9)$$

$$l_y = zp_x - xp_z \quad (3.10)$$

$$l_z = xp_y - yp_x \quad (3.11)$$

$$\mathbf{l} \equiv (l_x, l_y, l_z); l^2 = l_x^2 + l_y^2 + l_z^2. \quad (3.12)$$

Similarly, $\hat{\mathbf{S}}$ can be defined as:

$$S_x = \frac{\hbar}{2} (|+\rangle \langle -| + |-\rangle \langle +|) \quad (3.13)$$

$$s_y = \frac{i\hbar}{2} (-|+\rangle \langle -| + |-\rangle \langle +|) \quad (3.14)$$

$$s_z = \frac{\hbar}{2} (|+\rangle \langle +| - |-\rangle \langle -|) \quad (3.15)$$

$$\mathbf{s} \equiv (s_x, s_y, s_z); s^2 = s_x^2 + s_y^2 + s_z^2, \quad (3.16)$$

with $|+\rangle$ and $|-\rangle$ being eigenkets of a spin operator.

When the term $\hat{\mathcal{H}}_{rep} \gg \hat{\mathcal{H}}_{S.O.}$, in Eq. (3.1), i.e., $\hat{\mathcal{H}} \approx \hat{\mathcal{H}}_0 + \hat{\mathcal{H}}_{rep}$, the L-S coupling scheme known as Russell-Saunders coupling is valid. That is, the vectors \mathbf{L} , \mathbf{S} , and \mathbf{J} can be expressed as follows:

$$\mathbf{L} = \sum_i l_i, \quad (3.17)$$

$$\mathbf{S} = \sum_i s_i, \quad (3.18)$$

and

$$\mathbf{J} = \mathbf{L} + \mathbf{S} \quad (3.19)$$

because $\hat{\mathbf{L}}$ and $\hat{\mathbf{S}}$ commute with $\hat{\mathcal{H}}$. Unfortunately, the approximation giving rise to (3.19) is only valid for light atoms because $\hat{\mathbf{L}}$ and $\hat{\mathbf{S}}$ do not commute with $\hat{\mathcal{H}}$ when the spin-orbit term is included. As one goes down the periodic table the value of the $\hat{\mathcal{H}}_{S.O.}$ term increases. A new coupling scheme, j-j coupling, must be introduced where \mathbf{L} , \mathbf{S} , and \mathbf{J} can be expressed as follows:

$$\mathbf{j}_i = \mathbf{l}_i + \mathbf{s}_i \quad (3.20)$$

and

$$\mathbf{J} = \sum_i \mathbf{j}_i. \quad (3.21)$$

The quantum number J does commute with $\hat{\mathcal{H}}_{S.O.}$, making this scheme useful when $\hat{\mathcal{H}}_{S.O.} \geq \hat{\mathcal{H}}_{rep}$. When dealing with atoms such as transition metals, the situation often is intermediate between Russel-Saunders and j-j coupling. Figure 3.2 illustrates the differences between L-S coupling and j-j coupling for a two electron system. In L-S coupling shown in (a), the electronic spin angular momentum for electron one (\mathbf{s}_1) and electron two (\mathbf{s}_2) combine to produce a total spin momentum \mathbf{S} . The same is true for the electronic orbital angular momenta \mathbf{l}_1 and \mathbf{l}_2 , which combine to give \mathbf{L} . \mathbf{L} and \mathbf{S} rotate around the total electronic angular momentum for the system (\mathbf{J}). In j-j coupling shown in (b), the electronic spin angular momentum for electron one (\mathbf{s}_1) and the electronic orbital angular momentum (\mathbf{l}_1) combine to give a total electronic angular momentum for electron one (\mathbf{j}_1). The same is true for electron 2. \mathbf{j}_1 and \mathbf{j}_2 combine to give the total angular momentum for the system (\mathbf{J}). It is of interest to note that while the quantum number M_L is not valid in the j-j coupling scheme, term symbols from L-S coupling still give a qualitatively good description for elements

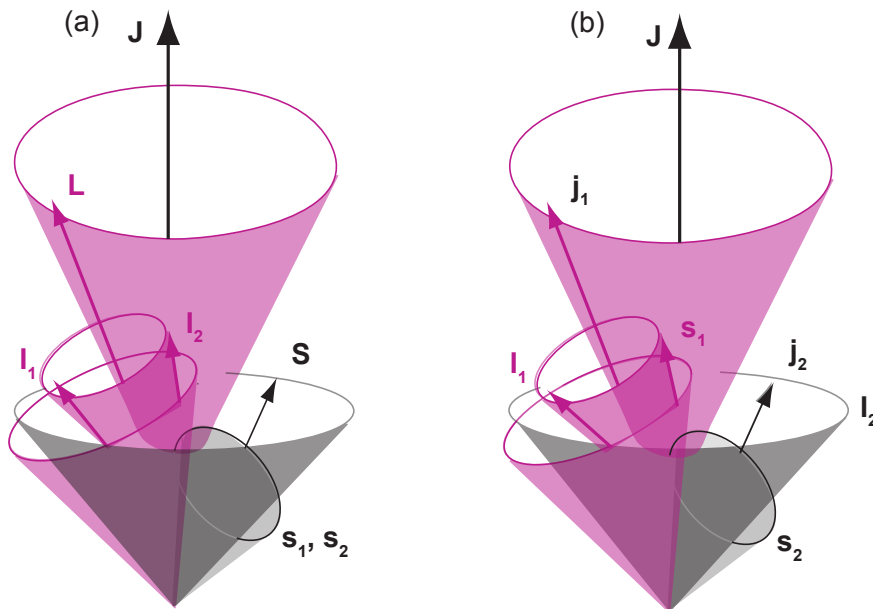


Figure 3.2: Two spin-orbit coupling schemes. The drawings are for a two electron system. (a) Russel-Saunders or L-S coupling . (b) j-j coupling.

which fall under the j-j coupling scheme and are often used. For example, the term symbol for U often is given as $^5L_6^O$. Figure 3.3 shows a correlation diagram for group IVA elements and the relationship of L-S term symbols to j-j coupling.

3.2.2 Other Theoretical Approaches

While ligand field theory may provide a simple description of metal ligand bonding in actinides, many research groups are developing *ab initio* (AI) and density functional (DF) methods for modeling them. These methods involve a full theoretical treatment of the polyatomic molecule which involves calculating the electronic wavefunction for a full range of parameters such as bond lengths and angles, though DF methods calculate the electron probability instead of the wavefunction. Roos and colleagues have been developing multi configurational configuration interaction methods specifically, complete active space (CAS) self consistent field (SCF) (CASSCF) and

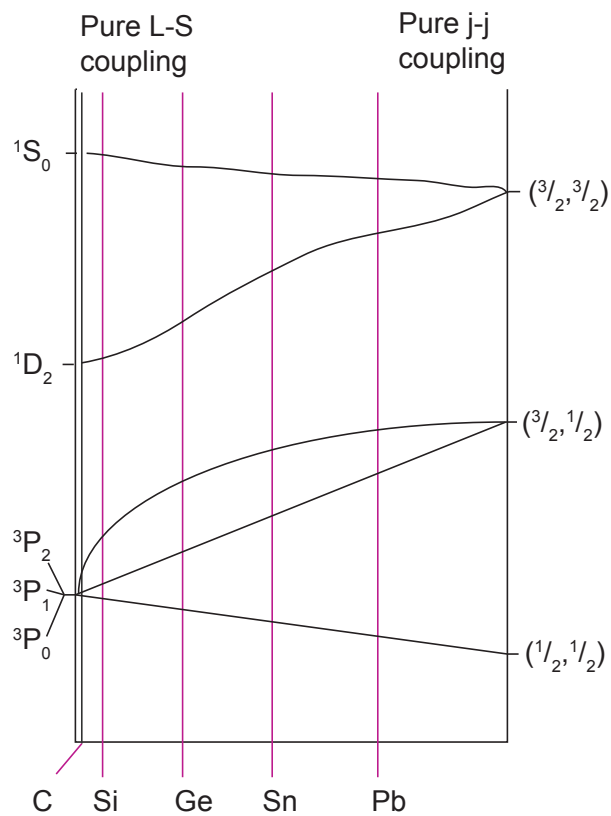


Figure 3.3: Correlation diagram for Group IVA elements. The diagram shows that L-S term symbols are qualitatively correct in the j-j coupling scheme. Note that the drawing is not to scale.

complete active space second order perturbation theory (CASPT2) methods. The later is a cheaper alternative to multi reference configuration interaction (MRCI) methods.[33] Coincidentally, Bursten and colleagues have been testing various DF methods for modeling actinides.[34, 11] Such calculations are very difficult because of the large number of electronic configurations resulting from open shell d and f orbitals as well as the need to account for the spin-orbit interactions and other relativistic effects. The next chapter will discuss some of these calculations pertaining to UO_2 and CUO . [35, 36, 37, 38, 33, 8, 6] Because electronic spectroscopy for these molecules was lacking, these papers mostly used ground state vibrational frequencies measured in MI experiments to test the theory, which often showed that theory was in agreement with the experiments. However, as mentioned earlier, a motivation for the experiments here was to provide experimentally measured electronic structure data to validate these calculations.

While the actinide spectroscopy had the primary goal of providing data to evaluate theoretical predictions, the calculations have advanced to the point where they may detect flaws in the experimental data and entice experimentalists to remeasure some fundamental properties. One such example is the determination of the ionization potential (IP) of UO_2 . Electron impact experiments dating back to 1974[39, 40, 41] provided a value of 5.49(1) eV for the first IP. Later, both Zhou *et al.*[8] (using B3LYP/pseudopotential method) and Gagliardi *et al.*[33] (using multiconfigurational wave functions CASSCF/CASPT2, together with a newly developed method to treat spin-orbit coupling) independently calculated the IP to be 6.27 eV and 6.2 eV respectively. Gagliardi *et al.* were confident enough of their results that they encouraged the experimentalists to reexamine the IP. Han *et al.*[42] repeated the measurements of the IP of UO_2 using resonant enhanced multiphoton ionization spectroscopy (REMPI) and recorded an IP of 6.128(3). It was determined that thermal population of UO_2 in the electron impact experiments caused earlier underestimations of the IP.[42, 33].

Despite what seemed to be an agreement between experimentalists and theoreticians on the IP for UO_2 , more recent *ab initio* calculations by Tyagi[29] using a 60-electron core potential with cc-pVDZ quality basis set gave an IP of 5.6 eV, about 0.6 eV lower than DFT. When double and single excitations out of 6p to 6s were allowed, the calculated value improved to 5.96 eV, but there was still a discrepancy. Tyagi speculated that the low level of electron correlation effects in her calculations as one possible source of error. As made evident by the discrepancy in various computational methods, a generalized theoretical model for actinides has not yet been achieved, and much more experimental data, such as the results presented here, will be needed to help theoreticians improve their computational methods.

3.3 Matrix Effects in Heavy-Metal Spectroscopy

MI spectroscopy has often been used for studying challenging molecules such as those containing actinides because it was often easier than gas phase spectroscopy. The rare gases used as matrix hosts, with the exception of Xe, were known to be inert and minimally perturbing to the sample molecules. Consequently, matrix experiments were thought of as complimentary to gas phase experiments, providing some data that was much harder to obtain in the gas phase. In 1985 and 1987 Marilyn Jacox published two studies which compared matrix shifts observed in both the IR and fluorescence spectra for various diatomic molecules.[43, 44] She reported that these shifts were less than 2% with the exceptions primarily being group Ia and IIIa halides as well as the open-shell van der Waals molecules. Even transition metal oxides had very small shifts. Therefore with the absence of sufficient gas-phase data for actinide containing molecules, researchers assumed that the matrix data were adequate for evaluating the theoretical predictions. However, for molecules containing heavy atoms, researchers

are learning that the matrix host can have unusually large perturbations on vibrational frequencies such as in the case for CUO[35, 36, 37, 38] isolated in solid Ar discussed in Chapter 4. These papers suggest that the perturbations are so strong that they reorder the low-lying electronic states of the actinide containing molecules. Hence, the concept of a rare gas / actinide chemical bond is a topic of current interest.

Chapter 4

Uranium Dioxide (UO₂)

4.1 Introduction

In the 1980's the matrix shifts in both electronic levels and in vibrational frequencies of small molecules were calculated.[43, 44] The shifts were found to be less than 1% and 2% for the electronic and ground vibrational levels respectively, with the exception of such species such as open shell molecules. Up until the mid 1990's the idea of small matrix shifts was thought to be valid even for molecules for which the shifts had not been calculated. However, Andrews and colleagues observed unusually large matrix shifts for UO, UO₂, and CUO when the host was changed from Ne to Ar.[45, 8, 46] For example, Andrews and colleagues[8, 47] observed the antisymmetric stretch of UO₂ at 914 cm⁻¹ in Ne and at 776 cm⁻¹ in Ar. Zhou *et al.*[8] used DFT to investigate the cause of this large effect. Their calculations were the first to indicate that UO₂ has a ³Φ ground state derived from the U(5f7s) configuration. Prior studies had concluded that the ground state was ³H, derived from U(5f²). Zhou *et al.*[8] found that the calculated vibrational frequency for the ³Φ state corresponded to the Ne matrix result, while the frequency for the ³H state agreed with the Ar matrix data. Consequently, they proposed that the guest-host interaction in Ar reversed the

ADF/PW91 Linear Transit Energy Curves for $\text{UO}_2 + 5\text{Ar} \rightarrow \text{UO}_2(\text{Ar})_5 (\text{D}_{5h})$

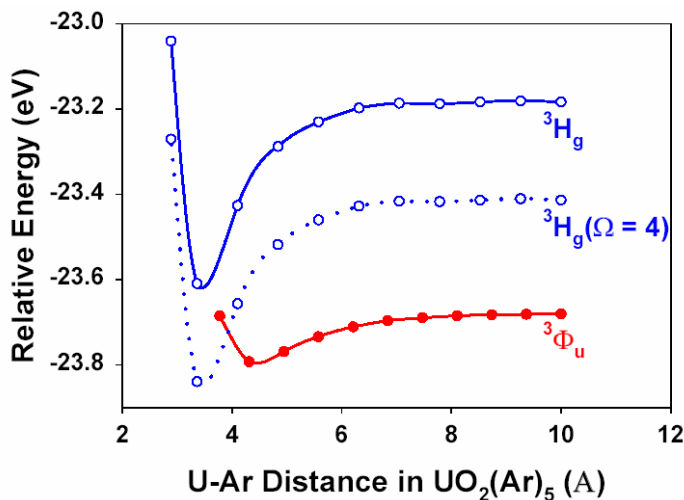


Figure 4.1: ADF/PW91 linear transit potential energy curves for $\text{UO}_2 + 5\text{Ar} \rightarrow \text{UO}_2(\text{Ar})_5 (\text{D}_{5h})$. [6] Differential spin-orbit stabilization stabilizes ${}^3\text{H}_g$ curve by 0.23 eV.

energy ordering of the ${}^3\Phi$ and ${}^3\text{H}$ states. Similarly, it had been proposed that the interaction between CUO and Ar was large enough to reorder the low-lying electronic states. [11, 48]

Also, to further support the theory of ground state reversal for UO_2 , Li *et al.* [6] calculated transit potential energy curves for both the ${}^3\Phi_u$ and the ${}^3\text{H}_g$ electronic states of UO_2 using scalar relativistic DFT calculations (see Figure 4.1). It is important to note that the results as indicated by the solid curves in the figure are for spin-free calculations. Even with the explicit addition of 5 Ar atoms, the ${}^3\Phi_u$ was lower in energy. However, the energy gap between the two states was small enough that when the 0.23 eV spin-orbit differential stabilization energy (relative to the ${}^3\Phi_u$ state) calculated by Gagliardi *et al.* [33] was added to the calculations, the ${}^3\text{H}_g$ became lower in energy. While the previous results leading up to these experiments presented here correlated the ground state frequencies for UO_2 in solid Ar with the ${}^3\text{H}_g$ electronic state, the ground state was never confirmed with electronic spectroscopy. The electronic (fluorescence) spectrum for UO_2 would be very telling

because one would observe a very different pattern of emission bands if the ground state configuration changed from $U(5f7s)$ to $U(5f^2)$. The experiments in this chapter probed the ground state electronic configuration for UO_2 isolated in solid Ar and investigated the rather large matrix shifts observed for actinides trapped in solid Ar.

4.2 Experiment Details

The source of uranium was uranium turnings (Johnson-Mathy) formed into a disk using an arbor press. Uranium dioxide was obtained in the gas phase by laser vaporization of the uranium metal target as discussed in Section 2.3.2.1. The ablated material was carried to the matrix chamber in a effusive flow of Ar that contained 0.1% O_2 . This mixture was chosen because it provided optimal yields of UO_2 in previous laser ablation studies.[8, 47] However, the target used in our matrix experiments was so heavily oxidized that good yields of UO_2 could be obtained without adding O_2 to the carrier flow, and hence, all the spectra shown in section 4.3 are from matrices made without additional O_2 . During these experiments, the FTIR spectrometer was not present, so the matrix setup with the Cu substrate was used. After deposition, spectra were recorded in the manner described in section 2.4. A 0.4 μs boxcar gate, delayed by 0.3 μs relative to the excitation pulse, was used to record dispersed fluorescence spectra.

Flourescence from Ablated U + O₂ Induced by 266 nm Radiation

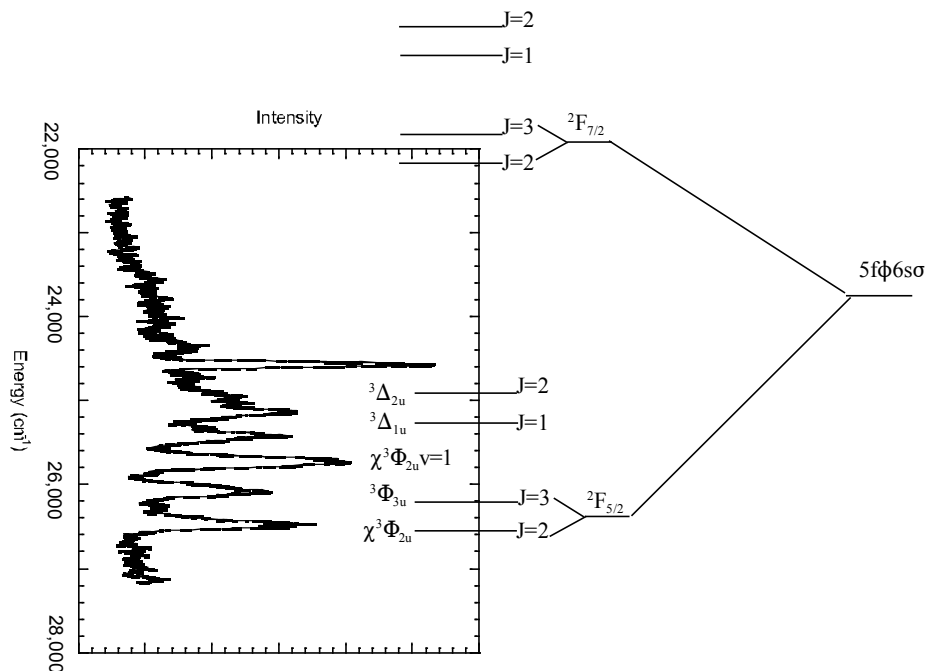


Figure 4.2: UO₂ fluorescence induced by 266 nm radiation. An energy level diagram for the U(5f7s) electronic configuration has been added to the right of the spectra for ease of interpretation.

4.3 Results

4.3.1 Fixed Wavelength Excitation

Figure 4.2 shows a dispersed fluorescence spectra induced by 266 nm radiation for a matrix formed from the products of an ablated U target mixed with Ar. The observed bands have been assigned to UO₂. The assignment of the ³Φ_u ground state is based upon a comparison with gas phase resident multi photon ionization (REMPI) spectra.[49] The labeling of the levels in the energy diagram on the right side of the spectrum is based on the predicted splitting in an U(5f7s) electronic configuration. Table 4.1 summarizes the observed bands for UO₂ and shows that they are in agreement with theory. These bands exhibited a line width of 150 cm⁻¹ [full width half maximum (FWHM)], which was broader than the resolution setting of the monochro-

Band Position (cm ⁻¹)	Energy (cm ⁻¹)	Theory (cm ⁻¹) Chang <i>et al.</i> ^a	Theory (cm ⁻¹) Gagliardi <i>et al.</i> ^b	Theory (cm ⁻¹) Gagliardi <i>et al.</i> ^c	Theory (cm ⁻¹) Infante <i>et al.</i> ^d	Assignment
27,036	0	0	0	0	0	X ³ Φ _{2u}
26,628	408	431	403	378	368	³ Φ _{3u}
26,265	771					X ³ Φ _{2u}
25,942	1,094	1,088	1,935	2,567	2,231	³ Δ _{2u}
25,635	1,401	1,566	2,340	2,908	2,588	³ Δ _{1u}

a=reference [50]; b=reference [33]; c= reference [51]; d=reference [52]

Table 4.1: Measured low-lying energy levels of UO₂ compared with theory.

U+Ablated O₂ Visible Fluorescence Induced by 266 nm Radiation

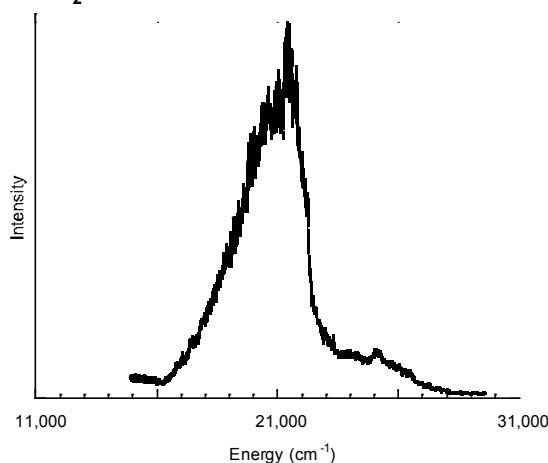


Figure 4.3: Visible UO₂ fluorescence induced by 266 nm radiation. There were no resolvable features in this broad band.

mator (estimated to be 70 cm⁻¹ in this wavelength range, based on the width of the scattered laser light when 355 nm excitation was used). It is probable that the resolution of the spectrum was limited by phonon wing broadening. Besides the UV fluorescence bands described above, there is a visible band in the spectrum of ablated U + O₂ isolated in an Ar matrix as shown in Figure 4.3.

Fluorescence decay curves were recorded for all of the resolved bands in Figure 4.2, (six different emission wavelengths) and four different regions of the broad emission feature in Figure 4.3 (21,053, 20,619, 19,608, and 17,452cm⁻¹). Beyond the scattered

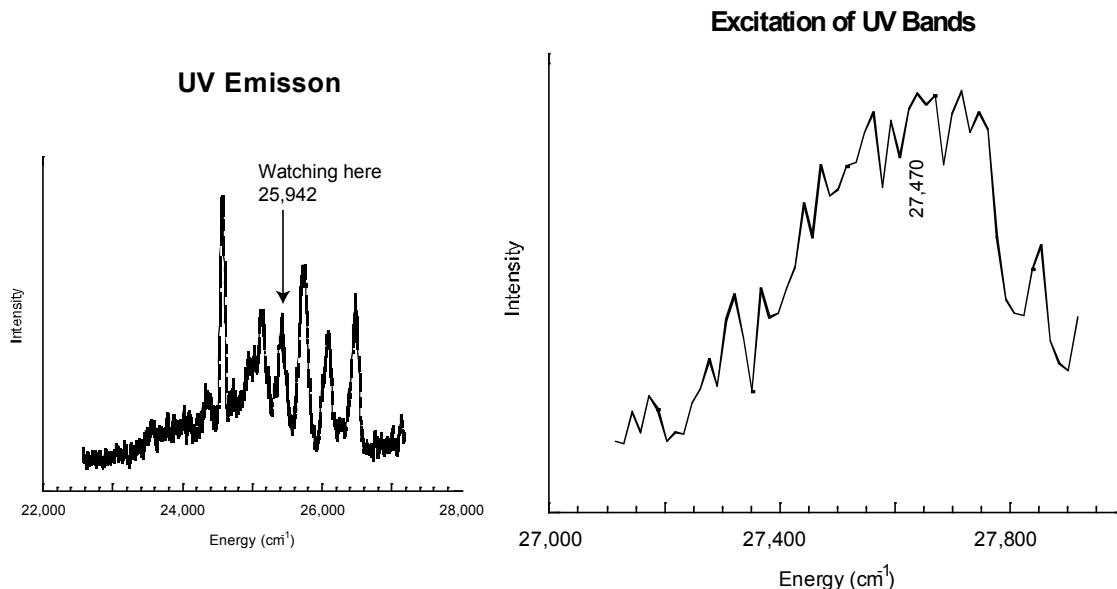


Figure 4.4: 25,942 cm^{-1} fluorescence induced by tunable radiation. The wavelength of the monochromator was set to the position indicated by the arrow in the left spectrum to record the excitation spectrum shown on the right. The tunable radiation was scanned over the energy region around of the ${}^3\Phi_u$ fluorescence band.

laser signals in the 0-0.100 μs range, the decay curves were single exponential, yielding a common fluorescence decay lifetime of $0.820 \pm 0.020 \mu\text{s}$.

4.3.2 Tunable Wavelength Excitation

Tunable laser excitation was used to investigate the excited levels that gave rise to the emission bands shown in Figure 4.2. Wavelength selected fluorescence excitation spectra were recorded by scanning the excitation wavelength while monitoring the light emitted by a specific emission band. The results from studies of gas-phase UO_2 were used to determine the range of excitation wavelengths examined.[49] A scan of the dye laser over the range from 27,778 to 26,881 cm^{-1} , with detection of fluorescence at 25,942 cm^{-1} , revealed a single broad excitation feature (Figure 4.4). This band was centered at 27,470 cm^{-1} with a FWHM of 400 cm^{-1} . The fluorescence decay

lifetime of the $25,942\text{ cm}^{-1}$ emission was examined using $27,470\text{ cm}^{-1}$ excitation. The beginning of the decay curve was obscured by intense scattered light from the laser that was partially transmitted by the monochromator, but fitting the tail of the decay signal yielded a lifetime of $0.120 \pm 0.030\ \mu\text{s}$.

An excitation spectrum, recorded using detection of the visible band emission at $20,833\text{ cm}^{-1}$, located two broad absorption features in the $27,778$ to $26,881\text{ cm}^{-1}$ region. One feature was identical to the one described above. The second feature was centered at $26,280\text{ cm}^{-1}$ with a FWHM of 420 cm^{-1} . Fluorescence decay curves for the $25,942\text{ cm}^{-1}$ emission, recorded using $27,470$ or $26,280\text{ cm}^{-1}$ excitation, yielded a lifetime of $0.090 \pm 0.030\ \mu\text{s}$.

A scan over the $30,303$ - $27,778\text{ cm}^{-1}$ range, with detection at $25,942\text{ cm}^{-1}$, yielded a broad absorption feature that was centered at $29,410\text{ cm}^{-1}$ with a FWHM of 420 cm^{-1} . The fluorescence decay lifetime was $0.310 \pm 0.020\ \mu\text{s}$. The visible emission band system was not present for $29,410\text{ cm}^{-1}$ excitation.

There were no features in the spectra obtained by UV excitation that could be assigned to U atoms or UO. To test for the presence of these species, matrices were excited using tunable radiation in the $17,606$ - $17,241\text{ cm}^{-1}$ range. From gas-phase studies, it is known that both U[53] and UO[54, 55] have strong absorption bands in this region. However, these experiments did not yield detectable emission from U or UO.

4.4 Analysis and Discussion

Evidence that the emitting species observed in these experiments was UO_2 was drawn from previous matrix experiments and complementary gas-phase studies. Hunt and Andrews[47] used IR spectroscopy to examine the range of species made by laser

ablating uranium metal into Ar/O₂ mixtures and trapping the products. They observed bands of UO, UO₂, and UO₃ in their matrices. Han *et al.* have examined the products produced by laser ablating an oxidized uranium target using mass spectrometry.[49, 42] Under the conditions of these matrix experiments, the products were found to be U, UO, and UO₂. As the visible excitation experiments did not show the presence of significant quantities of U or UO in the samples, it seems most likely that the emitting species was UO₂. This inference was further supported by the observation that the features of the fluorescence excitation spectra and the highest energy emission band recorded in the matrix correlate with a strong absorption feature in the spectrum of gas-phase UO₂.

REMPI with mass selected ion detection has also been used to characterize the electronic spectroscopy of UO₂. [42] The REMPI spectrum shows strong features at 27,260 and 29,669 cm⁻¹. The maximum of the 27,473 cm⁻¹ matrix band is blue-shifted relative to the gas phase bands by 210 cm⁻¹, which is typical for an electronic transition of a small molecule isolated in solid Ar.[44] Note that the red edge of the 27,473 cm⁻¹ band (at approximately 27,100 cm⁻¹) overlaps the blue edge of the 27,027 cm⁻¹ emission feature, which extends to 27,137 cm⁻¹. This is consistent with a single electronic transition that is phonon broadened (blue-shading on excitation and red-shading on emission, see Figure 4.5). The overlap of the excitation and emission bands indicates that the zero-phonon transition occurs at 27,120 cm⁻¹, just 140 cm⁻¹ below the position of the corresponding gas-phase band. The fact that the excitation and emission features overlap indicates that there is some inhomogeneous line broadening due to differences in local trapping sites. The maximum of the 29,412 cm⁻¹ excitation band is red-shifted 260 cm⁻¹ relative to the corresponding gas-phase band by 260 cm⁻¹. As noted above, this shift is within the range typically encountered for Ar matrices.

Overall, the pattern of low-lying electronically excited levels of UO₂ revealed by

Usually, in fluorescence spectroscopy, the red edge of the excitation band $27,240\text{ cm}^{-1}$ (bottom right) will correlate with the blue edge of the emission band $27,140\text{ cm}^{-1}$ (bottom left). However energy can be transferred to the matrix host through vibrations in the lattice called phonons, which produces lower energy emission as shown (top right).

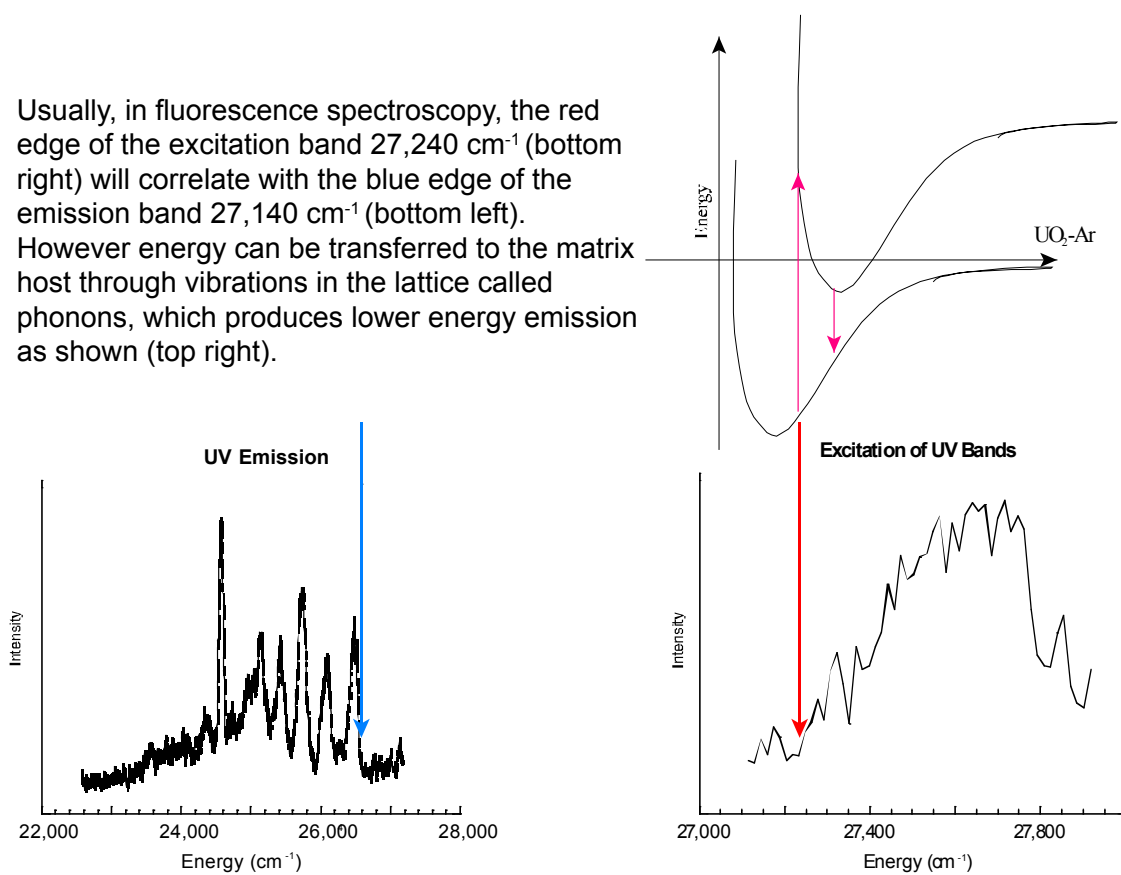


Figure 4.5: The phonon effect.

the matrix emission spectrum is in quasi agreement with the predictions of high-level theoretical calculations.[33, 50] It has been established that UO_2 is a linear, symmetric molecule in the ground and excited states. *Ab initio* studies of UO_2 excited states have been carried out by Chang[50] and Gagliardi et al.[33] In agreement with the DFT study by Zhou et al.,[8] these calculations predict that the lowest energy states are derived from the U (5f7s) configuration. The ground state is $X^3\Phi_{2u}$, with the $^3\Phi_{3u}$ component lying at approximately 420 cm^{-1} higher in energy (Han et al.[49] found that these levels are separated by 368 cm^{-1} in the gas phase). The calculations of Chang[50] and Gagliardi *et al.*[33] predict $\Omega = 1u$ and $2u$ levels, derived from the lowest energy $^3\Delta$ state, that lie about $1,500 \text{ cm}^{-1}$ above the $^3\Phi$ states. This pattern is readily discerned in Figure 4.2. Band assignments are given in Table 4.1, and the theoretically predicted energies are compared with the intervals derived from the spectrum. This assignment scheme carries the implication that the transitions originate from an $\Omega = 2g$ state. The emission band at $26,265 \text{ cm}^{-1}$ terminates on a level that is $771 \pm 10 \text{ cm}^{-1}$ above the ground state. This interval is consistent with excitation of the U-O stretch vibration. The asymmetric stretch fundamental of UO_2 in Ar[47, 56] is observed at 776 cm^{-1} . The symmetric stretch has been observed at 728 cm^{-1} for the mixed isomer $^{18}\text{U}^{16}\text{O}$. From this observation, Gabelnick *et al.*[56] derived a frequency of 765 cm^{-1} for U^{16}O_2 . The uncertainty in the vibrational interval from the emission spectrum is too great for assignment of the symmetry of the stretch mode. However, as it is unlikely that electronic excitation would break the inversion symmetry of the molecule, it is more probable that the symmetric stretch would be active in the emission spectrum. Also, the assignment of the $25,942 \text{ cm}^{-1}$ band to the $^3\Delta_{2u}$ electronic state is questionable based on the latest calculations by Infante *et al.*[52] Alternatively, they suggest that the band is one quanta of the stretching frequency for the $^3\Phi_{3u}$ excited electronic state. With this alternative assignment, it is possible that origin bands of $^3\Delta_{1u}$ and $^3\Delta_{2u}$ actually are observed in the congested

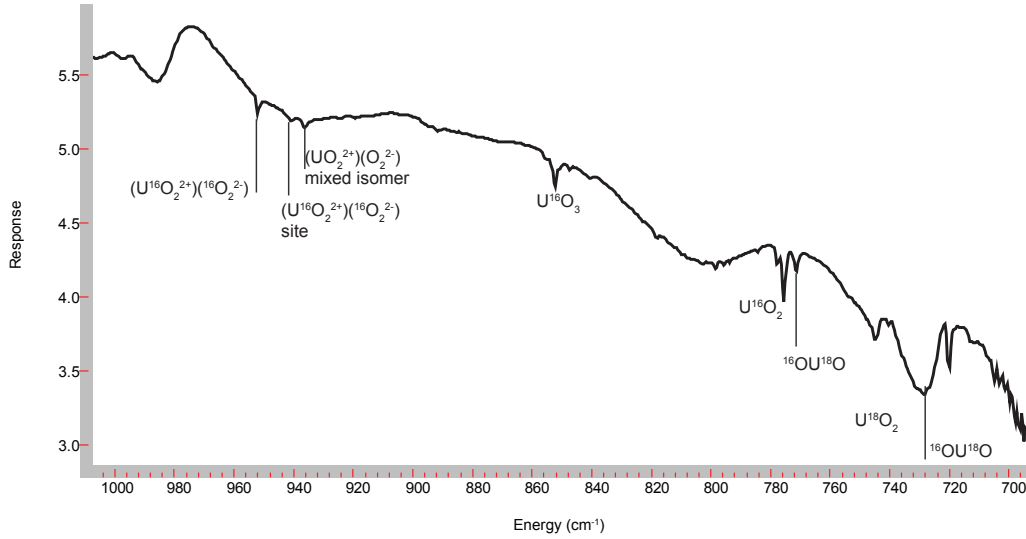


Figure 4.6: IR Spectrum of ablated U + ¹⁶O/¹⁸O (5/1) isolated in solid Ar. Assignments based on Hunt and Andrews’s spectra.[47]

25,510 -24,038 cm⁻¹ range of the spectrum because the most recent calculations by Gagliardi[51] and Infante[52] predict their energy levels approximately 1,000 cm⁻¹ higher than the previous predictions by Chang[50] and Gagliardi *et al.*[33]. With all the congestion, though, it is impossible to make any unambiguous assignments in this region, which may contain excited vibrational levels of the X ³Φ_{2u} and ³Φ_{3u} states as well.

It is also of interest to note here that in later experiments that attempted to look at UO₃ fluorescence (Section 6), the mixed isomer ¹⁸OU¹⁶O was observed using IR spectroscopy (See Figure 4.6). While the mixed isomer ¹⁸OU¹⁶O was observed by Gabelnick *et al.*[56], it was not observed by Andrews and colleagues[47]. The major differences between the two experiments is that Gabelnick used a Knudsen cell to vaporize the uranium atoms and Andrews used laser ablation. Andrews proposed the following insertion mechanism for UO₂ formation:



$$(\text{OUO})^* \rightarrow \text{OUO}. \quad (4.2)$$

He suggested that unlike in the experiment performed using a Knudsen cell, there was not enough energy to dissociate molecular oxygen because there was no mixed isomer of UO_3 trapped in his matrix, which would easily form from a mixture of ^{16}O and ^{18}O atoms. Also, if there were trapped O atoms in the matrix, they could form UO_2 during annealing, but the intensity of the UO_2 stretching absorption did not change much after annealing. The results of the experiments here, though, called to question the insertion mechanism for UO_2 formation because the mixed isotope was observed.

As for the upper state that gives rise to the UV fluorescence, Chang's calculations[50] provide two plausible candidates for the upper level of the near UV emission bands. The first is a state predicted to lie at a slightly higher energy ($33,092 \text{ cm}^{-1}$) that belongs to the $\text{U}(5f\phi 7p\sigma_u)$ configuration and has a wave function that is 77% ${}^3\Phi_{2g}$. The second candidate level, derived from $\text{U}(5f\phi 7p\sigma_u)$, is at $26\,222 \text{ cm}^{-1}$. It is composed of a mixture of singlet and triplet basis states (the leading terms are $48\% {}^1\Delta_{2g} + 30\% {}^3\Delta_{2g}$). It is apparent from both the energetics and the fluorescence decay kinetics that excitation of the UO_2 bands using wavelengths shorter than $27,778 \text{ cm}^{-1}$ proceeds via nonradiative relaxation processes. The observation that the near UV and visible emissions exhibit the same slow decay rate for excitation at 355, 308, and 266 nm indicates that a common bottleneck is encountered in the paths to both states. The shorter lifetimes obtained using longer wavelength excitation are likely to be much closer to the intrinsic lifetimes of the emitting levels. Excitation at 308 and 266 nm was found to be more effective than excitation at 355 nm, which suggests that the shorter wavelengths accessed transitions that had greater oscillator strengths. Photons with $\lambda \geq 308 \text{ nm}$ ($32,468 \text{ cm}^{-1}$) may have enough energy to reach the $\text{U}(5f\phi 7p\sigma_u) {}^3\Phi_{2g}$ state, while 355 nm light must rely on the weaker transition that excites $\text{U}(5f\phi 7p\sigma_u) {}^1\Delta/{}^3\Delta$ directly. Calculations for levels above $33,092 \text{ cm}^{-1}$

are not available, so we do not have information concerning the states that might be accessed by 266 nm excitation.

Excitation spectra show that the upper level of the visible emission band system lies at least $1,190 \text{ cm}^{-1}$ below the upper level of the near UV bands. Here, we consider two alternative assignment schemes for the visible bands, derived from the energy level calculations of Chang.[50] First, we assume that the upper level is directly excited by $26,281 \text{ cm}^{-1}$ light. Because the visible bands span the range from 21,277 to 16,667 cm^{-1} (cf., Figure 4.3), this assumption implies that the lower levels are 5,000-9,600 cm^{-1} above the $X^3\Phi_{2u}$ ground state, which is in reasonable agreement with the theoretical calculations that predict the following states (energies in cm^{-1} units given in parentheses): $3u(5,398)$, $4u(5,756)$, $2u(5,864)$, and $3u(6,514)$. The alternative interpretation is to assume that the upper level is populated by nonradiative transfer, which is then followed by radiative decay to the same group of lower levels that are accessed by the near UV emission bands. This interpretation would place the upper level of the visible bands at $21,280 \text{ cm}^{-1}$. Chang’s calculations[50] predict three plausible candidates for this level, all of which have good oscillator strengths for emission back to the ground state. The first two are a pair of $1g$ states at $20,262$ and $20,938 \text{ cm}^{-1}$, which are both derived from admixtures of the $^3\Delta_{1g}(5f\phi_7p\sigma_u)$ and $^3\Sigma_{1g}(5f\phi_u^2)$ states. The third state ($^3\Pi_{1g}(5f\phi_u 5f\sigma_u) + ^3\Pi_{1g}(5f\pi_u 5f\sigma_u)$) is at $22,190 \text{ cm}^{-1}$. At present, we do not have enough information to determine whether $26,281\text{cm}^{-1}$ light excites the visible bands by a direct or indirect process. However, Infante *et al.* [52] speculate that the $U(5f^1 6d^1)$ state may contribute to the observed fluorescence spectra based on results from Dirac-Coulomb intermediate Hamiltonian Fock-space coupled cluster (DC-IHFSCSD) calculations. This method provides the energies of all electronic configurations in one calculation rather than performing individual calculations for each configuration. The $U(5f^1 6d^1)$ was not considered in the previous CASPT2 calculations by Gagliardi *et al.*[33]

The analysis presented so far is based on the assumption that the electronic structure calculations for gas-phase UO_2 will also be valid for UO_2 isolated in solid Ar. This is usually a good approximation, but, as noted in Section 4.1, it has been suggested that the guest-host interaction in Ar matrices reorders the low-lying electronic states of UO_2 . Zhou *et al.*[8] propose that the ground state in Ar is $\text{U}(5f^2) {}^3\text{H}$. The present results are not consistent with this assignment. As the ground state would change from u to g symmetry, one would not expect to be able to correlate the gas-phase and matrix excitation spectra nor interpret the matrix emission spectra in terms of transitions to the lowest energy manifold of $\text{U}(5f7s)$ u states. Figure 4.7 (a) shows an illustration of the emission and excitation scheme consistent with an $\text{U}(5f7s)$ ground state. Figure 4.7 (b) shows an excitation scheme consistent with both the theoretical predictions by Zhou *et al.*[8] and the fluorescence spectrum shown in Figure 4.2. However if scheme (b) was correct, one would not be able to directly excite the ${}^1f^1p(g)$ because a $g \rightarrow g$ transition is forbidden. Also, the lowest energy states of the $\text{U}(5f^2)$ configuration are predicted to be the $\Omega = 4g, 5g,$ and $6g$ components of the ${}^3\text{H}$ term. In addition, there is a ${}^3\Pi_{1g}$ state just below ${}^3\text{H}_{6g}$ (which would not be optically accessible in an absorption-emission sequence that started from $\Omega = 4$). Chang's[50] calculations yield splittings between the ${}^3\text{H}$ levels of 3,850 ($5g-4g$) and 3,550 cm^{-1} ($6g-5g$). This same pattern of $\text{U}(5f^2)$ states was obtained by Gagliardi *et al.* (see Figure 2 of reference [33]). Clearly, the resolved bands of UO_2 in the 27,027-25,641 cm^{-1} range are not readily explained in terms of the $\text{U}(5f^2)$ energy levels.

From one perspective, it is not surprising to find that the ordering of the lowest energy UO_2 configurations is not reversed by UO_2 -Ar interactions. *Ab initio* calculations[33, 50] yield estimates for the energy separation between the ${}^3\Phi_2$ and ${}^3\text{H}_{4g}$ states of 8,389 and 4,200 cm^{-1} . DFT calculations that did not include spin-orbit coupling[8] gave a ${}^3\Phi$ - ${}^3\text{H}$ spacing of 1,930 cm^{-1} . It also is of interest to note, as mentioned previously, that the calculations by Li *et al.*[6] predict a ${}^3\text{H}$ state close

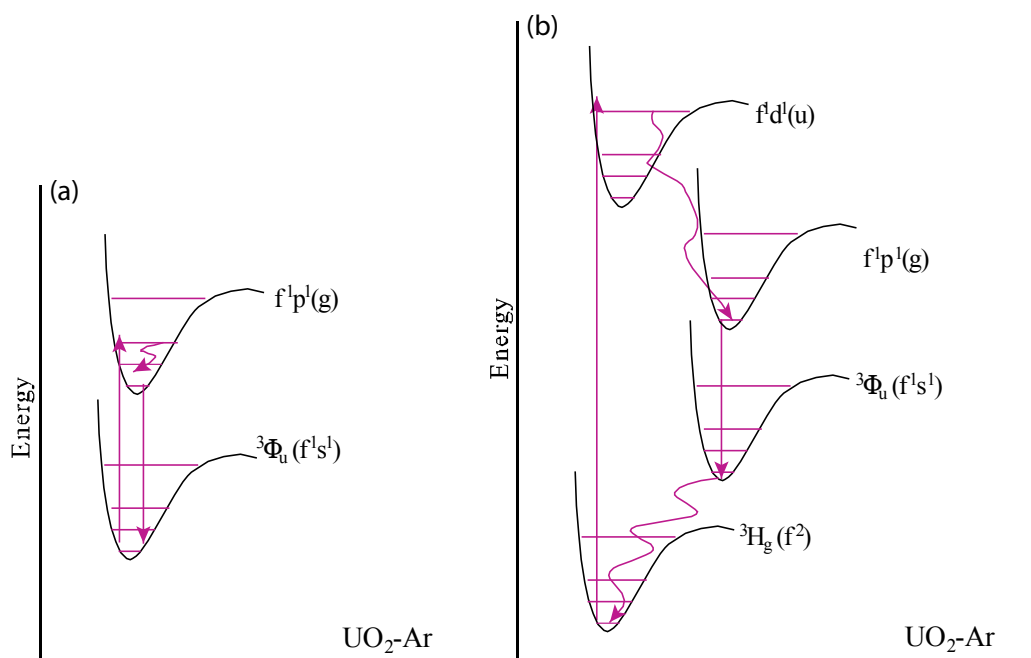


Figure 4.7: Two possible electronic configurations for UO_2 to describe the UV emission. (a) This diagram is the most simple explanation for the observed fluorescence from UO_2 isolated in Ar, which corresponds to ${}^3\phi_u$ being the ground state. (b) If the ground electronic state has a 3H_g configuration, then this diagram shows how electronic transitions from the ground state could be allowed.

enough in energy to the $^3\Phi$ ground state that spin-orbit effects can lower it below the $^3\Phi$ ground state. However, more recent calculations by Infante *et al.*[52] using DC-IHFSCCD predict a gap of $10,914\text{ cm}^{-1}$ between ^3H and the ground state, which is too large to be reordered by the interaction with multiple Ar atoms. It seems unlikely that interactions with Ar would be able to produce such large differential shifts in the energies of the $^3\Phi$ and ^3H states. In this context, it is of interest to consider the analogous results for CUO. Spin-free DFT calculations yielded a closed-shell $^1\Sigma^+$ ground state with a $^3\Phi$ state just 240 cm^{-1} higher in energy.[48] The C-UO stretching frequency was predicted to be $1,049$ and 902 cm^{-1} for the singlet and triplet states respectively. Calculations for CUO-Ar at the same level of theory yielded $^3\Phi$ as the ground state, with a C-UO stretching frequency of 887 cm^{-1} . These results were used to account for the anomalous change in the C-UO vibrational frequency in going from Ne ($1,047.3\text{ cm}^{-1}$) to Ar (852.5 cm^{-1}) matrices. Table 4.2 summarizes both these experiments and calculations for CUO. Roos *et al.*[37] raised doubts concerning this interpretation. They carried out *ab initio* calculations for CUO that included spin-orbit coupling (CASSCF/CASPT2/SO). At this level of theory, the spin-orbit interaction was found to be large for the triplet state, such that the $^3\Phi_2$ component lies about $4,000\text{ cm}^{-1}$ below $^1\Sigma^+$ for unperturbed CUO. Because the interaction with Ar stabilizes the triplet state relative to the singlet, it would not lead to state reordering in going from Ne to Ar matrices. However, *ab initio* calculations of Bursten *et al.*[34], carried out at the CCSD(T) level of theory, predict that the $^1\Sigma_0^+ - ^3\Phi_2$ splitting ($5,500\text{ cm}^{-1}$) is large enough that spin-orbit coupling would not be able to push $^3\Phi_2$ below $^1\Sigma_0^+$. The latest calculations by Visscher *et al.* at the DC-CCSD(T) level of theory, which included spin-orbit coupling, also predicted a $^1\Sigma_0^+ - ^3\Phi_2$ splitting of $4,865\text{ cm}^{-1}$, which was small enough to be re-ordered by the interaction of CUO with Ar in a matrix. While it was clear that there were unusually large matrix shifts for CUO in solid Ar and that the low-lying electronic states were close enough to be re-ordered,

Experimental			Calculated (relativistic DFT)		
$\nu_{\text{obs}} (\text{cm}^{-1})$	$^{12}\text{C}/^{13}\text{C}$	$^{16}\text{O}/^{18}\text{O}$	$\nu_{\text{calc}} (\text{cm}^{-1})$	$^{12}\text{C}/^{13}\text{C}$	$^{16}\text{O}/^{18}\text{O}$
Ne matrix			CUO($^1\Sigma^+$)		
872.2	1.0020	1.0554	874	1.0023	1.0549
	1.0361	1.001		1.0357	1.0019
			CUO($^3\Phi$)		
			843	1.0127	1.0514
			902	1.0260	1.0052
Ar matrix			CUO(Ar)($^3A''$)		
804.3	1.0196	1.0469	834	1.1025	1.0520
852.5	1.0188	1.0092		1.0260	1.0045
			CUO(Kr)($3A''$)		
803.1			832	1.0140	1.0512
851			885	1.0247	1.0076
			CUO(Xe)($3A''$)		
801.3	1.0202	1.0466	830	1.0155	1.0506
848	1.0181	1.0095	979	1.0233	1.0061

Table 4.2: Measured and calculated vibrational frequencies for CUO.[11] See the reference for further details on the computational methods used. As is seen in the tables the ground electronic state for CUO in Ne is $^1\Sigma^+$ and ground electronic state for CUO in Ar is $^3\Phi$.

State	Stretching Frequency (cm ⁻¹)		Method	Reference
	σ_g	σ_u		
³ Φ	874	931	B3LYP	a
³ Φ	896	913	MP2	b
³ Φ	927	958	CCD	b
³ Φ_{2u}	948	923	CASPT2/S0	c
³ H	792	814	B3LYP	a

a=reference [8]; b=reference [57]; c=reference [33]

Table 4.3: Theoretical predictions for the stretching vibrational frequencies of UO₂.

it was still unclear if there was a reordering of the low-lying electronic states when changing the matrix host from Ne to Ar. Because both the ground and first excited states have the same symmetry, it would not be as easy as with UO₂ to determine which electronic state was the ground state using electronic spectroscopy. As the present results for UO₂ do not indicate a reordering of states in Ar, it is difficult to explain both the low vibrational frequencies observed in Ar and the Ne/Ar matrix shifts. Vibrational frequencies for UO₂ obtained from DFT and *ab initio* calculations are collected in Table 4.3. In all cases, the frequencies for ³ Φ_2 are significantly larger than the matrix results ($\sigma_g=765$, $\sigma_u=776$ cm⁻¹).

4.4.1 Conclusions

It is evident from experiments and theoretical predictions that the configuration of the ground electronic state for UO₂ is a ³ Φ_{2u} state and that the interaction between UO₂ and Ar in a cryogenic matrix is not strong enough to re-order the low-lying electronic states. However, the interaction is strong enough to cause unusually large matrix shifts. For CUO, theoretical predictions indicate that the two lowest lying electronic

states are close enough in energy that the interaction with Ar in a cryogenic matrix could re-order these states. Unfortunately, because both the ${}^3\Phi_2$ and the ${}^1\Sigma_0^+$ have the same symmetry it would be hard to determine the ground state in a similar manner as was done here for UO_2 , though selection rules should make the observed fluorescence very different. Leaving the ground state mystery behind, it is apparent, from the anomalous matrix shifts, that both UO_2 and CUO exhibit unusually strong interactions with Ar and heavier rare gas atoms. This is an intriguing phenomenon that deserves further experimental and theoretical attention.

Chapter 5

Uranium Chlorides

As was stated in the prior chapters, the most stable oxidation state of U is the 6+ state, such as U(VI) in UF_6 . UF_6 was studied previously not only because it was stable (aside from being hygroscopic), but also because it was a gas at room temperature and could be used for gaseous diffusion. However, to obtain complete information on the electronic structure of U for use in developing theoretical models, other oxidation states of U have to be studied. The next most stable oxidation state of U is the 4+ state found in UCl_4 . Less than a handful of studies dating back to the 1960's were published on the electronic spectroscopy of this compound[58, 59, 60], and no one had ever reported fluorescence from UCl_4 . The experiments described below were an attempt to characterize electronic structure of UCl_4 using visible fluorescence spectroscopy.

5.1 UCl₄ and Its Chemical, Physical, and Spectra Properties

UCl₄ is obtained as an emerald green powder that is very hygroscopic and is often stored and handled in a glove box containing a N₂ atmosphere. It also has a very low vapor pressure given by the following:

$$\log(P_{atm}) = \frac{(-7233 \pm 15)}{T} + 6.77 \pm 0.02 \quad (5.1)$$

At room temperature the vapor pressure is 1.77×10^{-15} torr, and at 200 °C the vapor pressure is 2.27×10^{-6} torr, which is approaching a usable vapor pressure for creating a matrix. It is obvious, then, from Eq. 5.1 that UCl₄ must be vaporized for either gas phase or MI spectroscopy. The usual vaporization technique is thermal vaporization because UCl₄ is a powder. The first laboratory spectra of UCl₄ was published by McLaughlin in 1962.[60] He recorded single-crystal spectra (at liquid He temperatures to avoid thermal broadening) and was able to assign roughly 100 lines to their corresponding electronic states. The electronic ground state (³H; ^{2s+1}L) and D_{2d} symmetry were proposed based on comparison of the spectra with splitting parameters obtained from crystal field theory.

Results from a second experiment investigating the spectra of molten UCl₄ were published by Morrey a year later.[58] However, this experiment, at best, only provided information on the coordination chemistry of U (IV). The only gas-phase spectra of UCl₄ were published in 1966, also by Morrey *et al.*[59] The spectra were hot spectra recorded at temperatures between 950 to 1,250 K and were compared with the previous single-crystal spectra. Morrey had proposed a tetrahedral (T_d) geometry for gaseous UCl₄ claiming that it was possible for the distortions in crystallized UCl₄ to favor the D_{2d} geometry. He also noted that all vibrational modes should occur around

300 cm^{-1} . Unfortunately, his spectra were not resolved enough for him to confirm his proposal. UCl_4 was not spectroscopically studied again until a 1984 study by Arthers and Breattie in which they recorded the IR spectra of UCl_4 molecules isolated in an Ar matrix.[61] Unfortunately, in terms of providing more background for the UCl_4 experiments in this chapter, their paper spent more time on ThCl_4 . The authors, though, did propose a distorted C_{2v} geometry for UCl_4 . A similar study was carried out in 1994 by Hunt *et al.* in which they recorded the IR absorptions for the products of ablated U atoms mixed with Cl_2 trapped in solid Ar.[2] While there were many different molecules in his resulting “soup,” Hunt *et al.*'s[47] measurements for UCl_4 were in good agreement with Arthers and Breattie.[61] Table 5.1 lists the peak assignments for spectra recorded by Arthers and Breattie and Hunt *et al.*. These two experiments were a confirmation that UCl_4 had only low frequency vibrational modes, which were outside the energy range of the MCT detector. Hence IR spectra cannot be used to confirm the identity of UCl_4 in the MI experiments presented in this chapter.

5.2 Experiment Details

UCl_4 was obtained from Los Alamos National Laboratory or prepared in house (see Appendix B) and was stored and handled in the nitrogen atmosphere of a glove box because it is very hygroscopic. In order to make UCl_4/Ar matrices, 0.07g UCl_4 was placed in a 1/2" OD tube as described in Section 2.3.2.2. Samples were heated to approximately 400° C, and the subsequent vapor was mixed with Ar and allowed to flow at a rate of 3 mmol/h for about 3 hours onto a cold CsI or Cu plate held at 12 K. Usually, IR spectra were recorded immediately following deposition, though for the preliminary experiments the IR spectrometer was not present, and no IR spectra

UCl _x in Ar Absorptions		
Assignment	Position (cm ⁻¹) ^a	Position (cm ⁻¹) ^b
UCl ₄	355	
UCl ₄	353	
UCl ₄	346.2	346
UCl ₄	344.8	
UCl ₄	341.4	
UCl ₄	337.6	337
UCl ₄	334.9	
UCl ₄	330.4	
UCl ₄	328	
UCl ₄	327	
UCl ₄	322.8	323
UCl ₂		312
UCl ₂		308

(a)=reference[61]; (b)=reference[2]

Table 5.1: UCl_x IR absorptions. The table shows that there are no IR active modes for UCl₄ above 360 cm⁻¹.

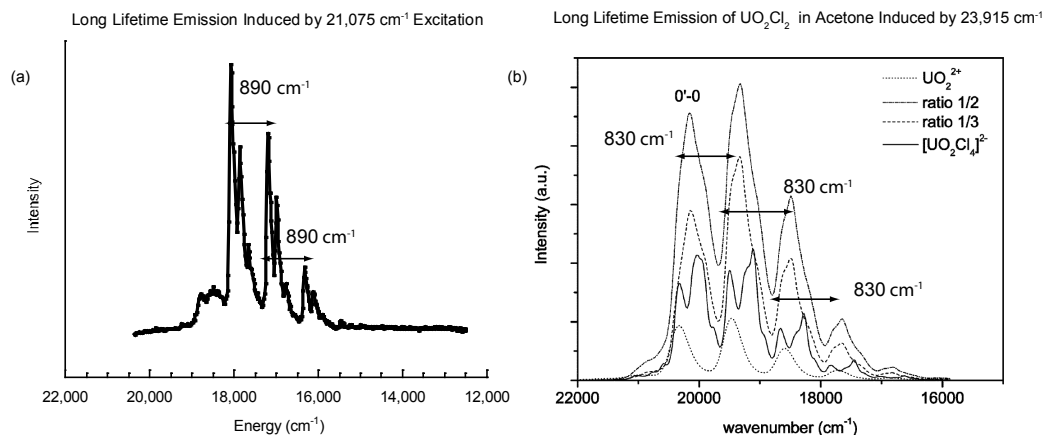


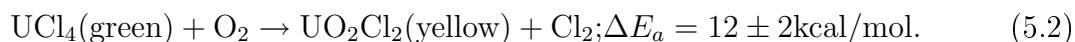
Figure 5.1: Comparison of UCl_4 trapped in solid Ar with UO_2Cl_2 in acetone. (a) Spectrum of thermally vaporized UCl_4 trapped in solid Ar. (b) Spectrum of UO_2Cl_2 in acetone recorded by Goerller-Walrand *et al.*[62] Notice the similarity between the spectra.

were recorded. Following the recording of the IR spectra, the matrices were excited using light from various pulsed laser sources.

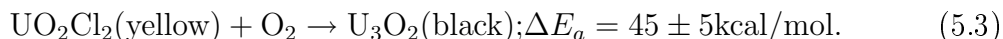
Figure 5.1 (a) shows a fluorescence spectrum of a matrix containing thermally vaporized UCl_4 in Ar recorded for the experiments presented here. Notice how there is an observed stretching frequency of approximately 890 cm^{-1} , which was not observed in any prior IR spectra for UCl_4 . During a search of the literature for information on UCl_4 the spectrum in Figure 5.1 (b) was found for UO_2Cl_2 in acetone, which is very similar to the spectrum in (a) with an apparent blue shift possibly caused by the acetone.[62] The four different traces in (b) are for different uranyl to chloride ratios ranging from UO_2^{2+} to $[\text{UO}_2\text{Cl}_4]^{2-}$. If the fluorescence spectrum in Figure 5.1 (a) is from UO_2Cl_2 , how easy is it to form UO_2Cl_2 from UCl_4 ?

5.3 The Uranyl Ion and the Oxidation of UCl_4 to Form UO_2Cl_2

With UO_2Cl_2 as a possible candidate for the molecule producing the fluorescence observed in the preliminary experiments, it is useful to understand how UO_2Cl_2 forms from UCl_4 and some of its properties. UO_2Cl_2 is the partially oxidized form of UCl_4 and is formed by the following reaction[63]:



UO_2Cl_2 can be further oxidized by the following reaction:



The product of Eq. 5.3 is black in color and has barely any vapor pressure compared with UCl_4 and UO_2Cl_2 at the same temperature. Similar reactions under aqueous conditions would produce liquid HCl.

When interpreting spectra containing UO_2Cl_2 it is best to think in terms of a uranyl ion, UO_2^{2+} , and 2Cl^- “spectator ions” which only slightly perturb the spectrum of the uranyl ion. No matter what counter ions are present, all spectra of the uranyl ion look similar. For example, Souter and Andrews[64] reported the antisymmetric stretching frequency for UO_2F_2 at 939.6 cm^{-1} which is 20 cm^{-1} red shifted from the same mode for the bare UO_2^{2+} , which is at 952.3 cm^{-1} . Common characteristics to fluorescence spectra containing the uranyl ion include absorption in the UV, violet, and blue regions of the spectrum ($\nu > 20,000 \text{ cm}^{-1}$), which gives rise to a yellow color and green, yellow, and orange fluorescence ($20,000 < \nu < 15,000 \text{ cm}^{-1}$).[62]

One of the first “modern” spectroscopic studies of the uranyl ion was in 1938 by Conn and Wu.[65] Since that time, there have been several spectroscopic studies of

uranyl containing species, most focusing on IR absorptions.[66, 67, 68, 62, 47, 69, 70, 71, 72, 73] The most extensive of these studies were those by Denning and colleagues in which the uranyl ion was studied experimentally in the crystalline form CsUO_2Cl_2 and $\text{CsUO}_2(\text{NO}_3)_2$. [69, 70, 73] While the crystal stabilized the UO_2^{2+} ion, the crystal field effect should have caused perturbations in the spectra that were so large that Denning’s experiments should not have been worth comparing to the matrix experiments presented here. However, they provided test data for later calculations performed by Pitzer’s group.[74, 75, 76] For the calculations, they used a relativistic effective core potential approximation and spin-orbit configuration interaction with various basis sets such as the U *cc*-pVDZ. Because the calculations were based on Denning’s crystalline experimental work, they would not be a good comparison for matrix or gas phase experiments. Probably, the most useful spectroscopic data published concerning the uranyl ion at the time these experiments were performed were the spectra of UO_2Cl_2 in acetone[62], though still very much different from data describing single isolated molecules. However, since that time there have been more extensive theoretical predictions for the electronic states of the uranyl ion, all of which include spin-orbit coupling and relativistic effects.[52, 77] Unlike the previous calculations, these calculations described single isolated molecules, and were suitable for comparison with the MI experiments presented here.

5.4 Further Experiments

5.4.1 IR Absorption Spectra

Figure 5.2 shows the products trapped in a matrix formed from thermally vaporized UCl_4 in Ar. The spectrum shows two predominant stretching frequencies at 896 ± 0.5 and 972 ± 0.5 cm^{-1} . The insert shows the R(0) line for HCl, a product of the oxida-

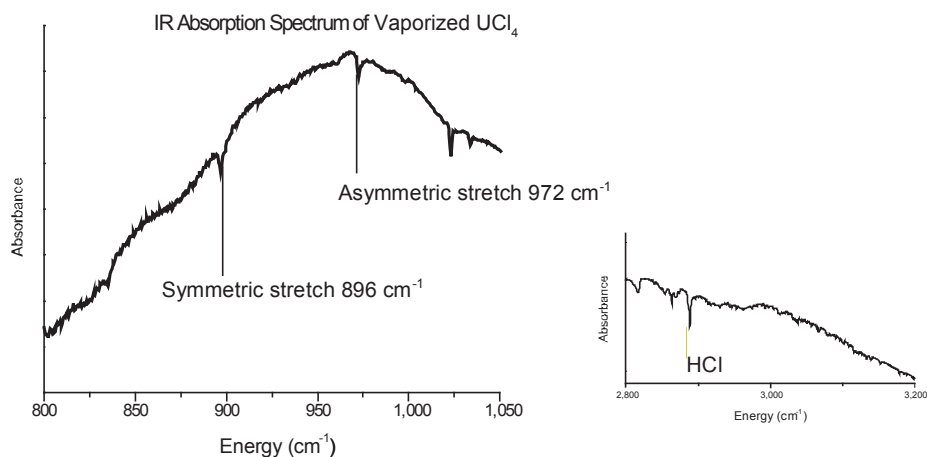


Figure 5.2: IR absorptions of thermally vaporized UCl_4 trapped in solid Ar. Two predominant stretching frequencies at 896 ± 0.5 and $972 \pm 0.5 \text{ cm}^{-1}$ are observed. The insert shows the R(0) line for HCl, a product of the oxidation / hydrolysis reaction of UO_2Cl_2 .

tion/hydrolysis reaction of UCl_4 . There is a curved baseline in both the spectrum and the insert because there was no background subtraction. Only when the absorption of interest overlapped with a component of air did background subtraction clarify a spectrum. Furthermore, the IR spectra for the experiments discussed in this chapter were collected before the purge box was constructed (see Section 2.2). Consequently, when such a large background was present, extra care was needed when subtracting the background to avoid “losing” the absorptions of interest, and the extra effort was not necessary for these experiments.

5.4.2 Fixed Frequency Excitation

Various fixed frequency UV pulsed lasers were used to excite the matrix. While 266, 308, and 355 nm excitation all produced strong fluorescence in the green and yellow regions of the visible spectrum, the fluorescence induced by 355 nm excitation was the best resolved. Laser excitation of the matrix at 355 nm produced the emission spectra

shown in Figure 5.3. By varying the time delay during which the fluorescence was recorded from 0.20 μs to 15 μs , it was determined that a group of resolved features in the 18,750-16,250 cm^{-1} range (Figure 5.3 (a)) were long-lived ($\sim 50\mu\text{s}$). The bands that are shown in Figure 5.3 (b), originating at 18,122 cm^{-1} , have an interval of 884 ± 7 cm^{-1} . The average of the two spacings observed for the mode was reported because the energy difference between the $2_1^0 \leftarrow 0_0^0$ and $1_2^0 \leftarrow 1_1^0$ transitions was less than the error in the measurement of vibrational energy. A second vibrational frequency of 230 ± 7 and 230 ± 7 cm^{-1} was also observed, with the higher frequency corresponding to the $2_1^0 \leftarrow 0_0^0$ transition. Another similar band system, originating at 18,504 cm^{-1} , showed intervals of 865 ± 12 and 109 ± 12 cm^{-1} . The frequency for the latter was an average of all four measured values because the values only differed within the error of the measurement.

Excitation at 355 nm also produced short-lived ($\sim 1.5 \mu\text{s}$) fluorescence in the 21,360-18,640 cm^{-1} region (see Figure 5.3 (a)). One band system with a roughly 360 ± 8 cm^{-1} vibrational progression begins at 21,115 cm^{-1} . Another emission band system begins at 19,390 cm^{-1} with a similar 360 ± 8 cm^{-1} progression. Additionally, there were three red fluorescence bands best induced by 308 nm excitation recorded with a short delay (0.2 μs) and gate (0.2 μs) (Figure 5.4). The bands were spaced roughly 550 cm^{-1} apart from each other.

Fluorescence decay curves were recorded for all of the bands in Figures 5.3 and 5.4. Figure 5.5 (a) shows a typical decay curve for what is tentatively β_1 fluorescence, which has a lifetime of $55.57 \pm 0.07\mu\text{s}$. Figure 5.5 (b) shows a decay curve for 18,504 cm^{-1} (β_0) fluorescence, which has a lifetime of $54.52 \pm 0.06\mu\text{s}$. Figure 5.5 (c) shows the fluorescence from the short-lived band located at 21,119 cm^{-1} has a lifetime of $1.328 \pm 0.004 \mu\text{s}$. Figure 5.5 (d) shows the band located at 19,390 cm^{-1} has a lifetime of $1.310 \pm 0.004 \mu\text{s}$. As was the case with all decay curves fitted for this work, much more error arose from the data collection than the actual fitting routine, which was

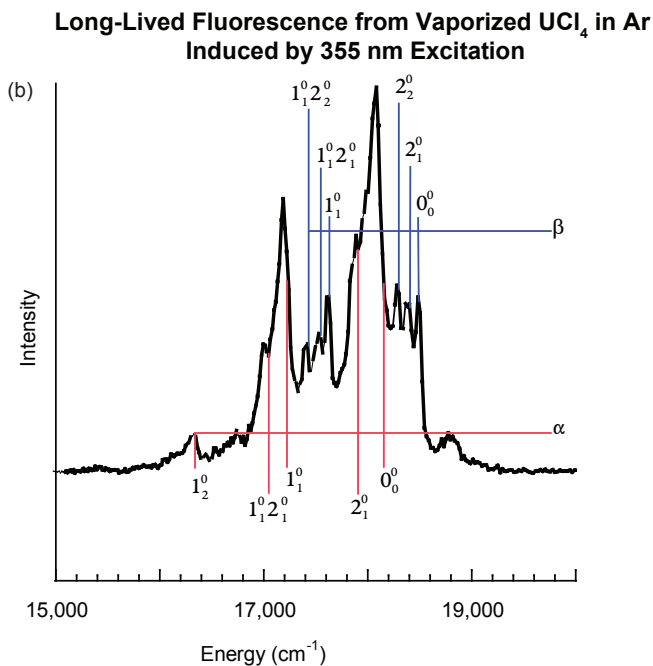
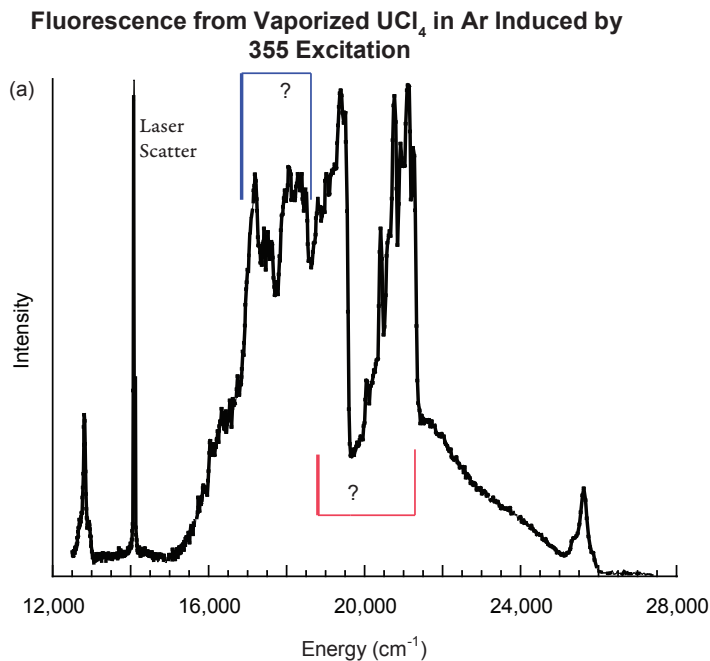


Figure 5.3: Fluorescence from thermally vaporized UCl_4 in solid Ar induced by 355 nm radiation. (a) The short-lived fluorescence shown here was recorded using a 0.200 μs delay and a 0.300 μs gate width with respect to the laser firing. Features showing characteristics of the uranyl ion are in blue, and features initially unassigned are in pink. (b) The long-lived fluorescence shown here was recorded using a 15 μs delay and a 15 μs gate width with respect to the laser firing. The α and β labeling scheme is discussed in Section 5.5 .

Short Lifetime Emission Induced by 308 nm Excitation

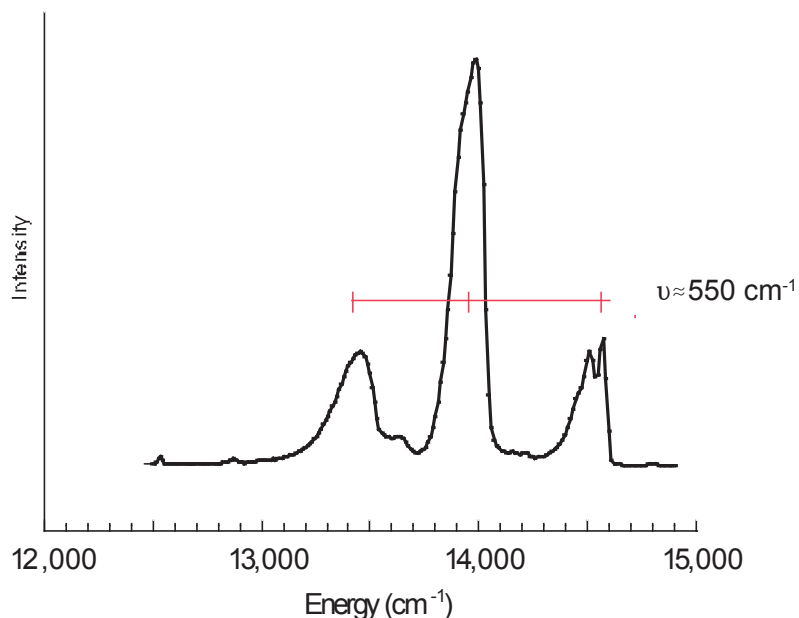


Figure 5.4: Short-lived fluorescence induced by 308 nm radiation. The spectrum was recorded with a 0.2 μs gate delayed 0.2 μs with respect to the laser firing.

estimated to be tens of microseconds. Consequently, there is no significant difference between the lifetimes of the α and β fluorescence. The steplike features near the baseline are an artifact of low oscilloscope resolution.

5.4.3 Tunable Excitation

Tunable laser excitation was used to investigate the excited levels that gave rise to the long-lived emission bands shown in Figure 5.3 (b). Wavelength selected fluorescence excitation spectra were recorded by scanning the excitation wavelength while monitoring the light emitted by the 18,122 cm^{-1} emission band, which was chosen because it is the blue-most of the long-lived bands (α_0). The excitation spectrum consists of a band system beginning at 21,027 cm^{-1} and exhibits both a $750 \pm 20 \text{ cm}^{-1}$ and a $150 \pm 20 \text{ cm}^{-1}$ progression (Figure 5.6 (a)). Exciting the matrix with 21,076 cm^{-1}

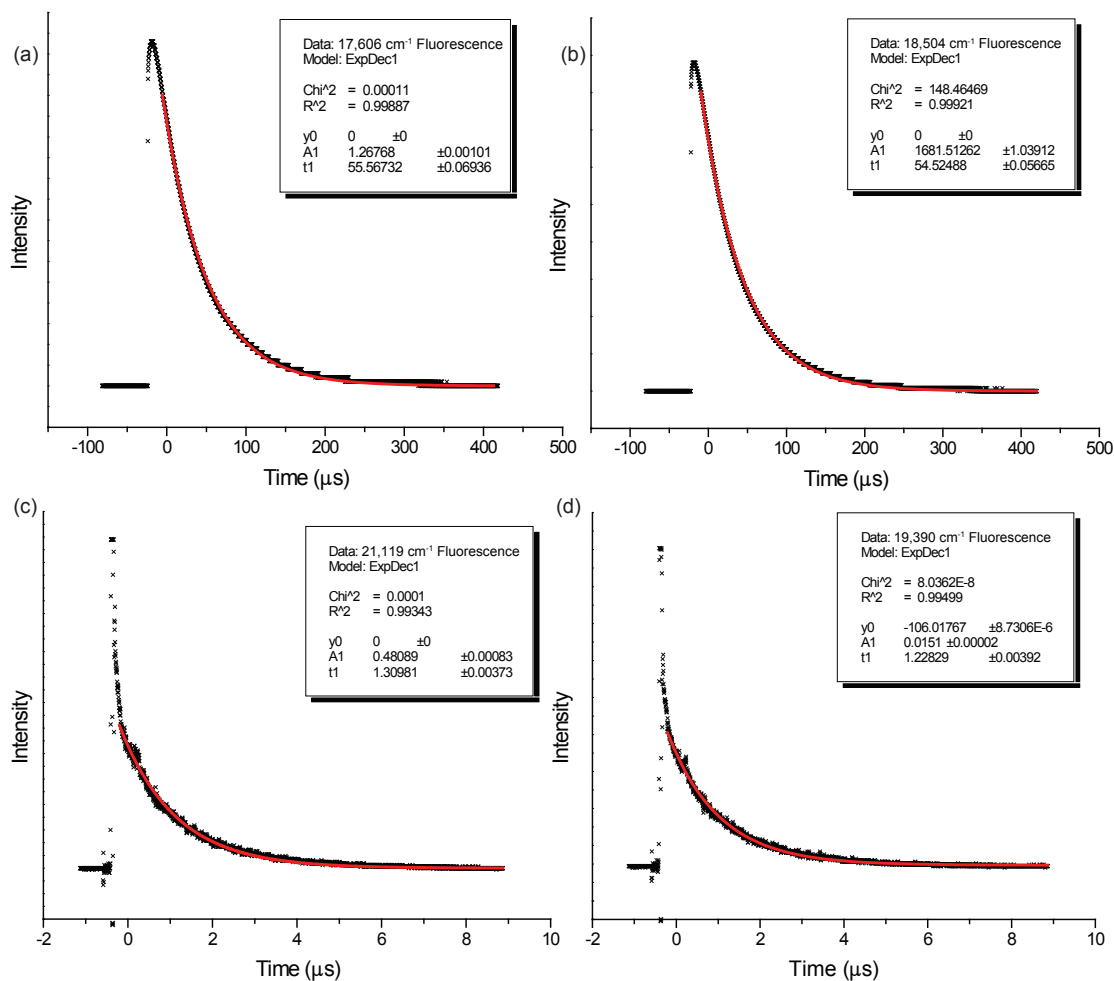


Figure 5.5: Fluorescence decay curves from thermally vaporized UCl_4 in solid Ar induced by 355 nm radiation. (a) 17,606 cm^{-1} fluorescence (β_1) from has a lifetime of $55.57 \pm 0.07 \mu\text{s}$. (b) 18,504 cm^{-1} fluorescence (β_0) from has a lifetime of $54.52 \pm 0.06 \mu\text{s}$. (c) 21,119 cm^{-1} fluorescence has a lifetime of $1.310 \pm 0.004 \mu\text{s}$. (d) 19,390 cm^{-1} fluorescence has a lifetime of $1.28 \pm 0.004 \mu\text{s}$.

light produces a much sharper emission spectrum (Figure 5.6 (b)). The short-lived bands observed in the 355 nm induced fluorescence spectrum are labeled ϕ in this spectrum. Notice how the weaker intensity of the ϕ fluorescence relative to the α fluorescence confirms the shorter lifetime of the ϕ bands.

Tunable laser excitation also was used to investigate the excited levels that gave rise to the short-lived emission bands shown in Figure 5.3 (a). Wavelength selected fluorescence excitation spectra were recorded by scanning the excitation wavelength while monitoring the light emitted by the 19,390 cm^{-1} emission band (ϕ). Two doublets were observed at 21,433 and 21,833 cm^{-1} , with a nearly identical splitting of $40 \pm 3 \text{ cm}^{-1}$ within each doublet (Figure 5.7 (a)). The energy between the doublets was $400 \pm 18 \text{ cm}^{-1}$. Again, exciting the matrix with 21,433 cm^{-1} light produced a more resolved spectrum (Figure 5.7 (b)). However, what appears to be structure on the red side of the large peak was attributed to random noise because it was not repeatable. The peaks at 14,600 cm^{-1} are the same short-lived features seen in Figure 5.4.

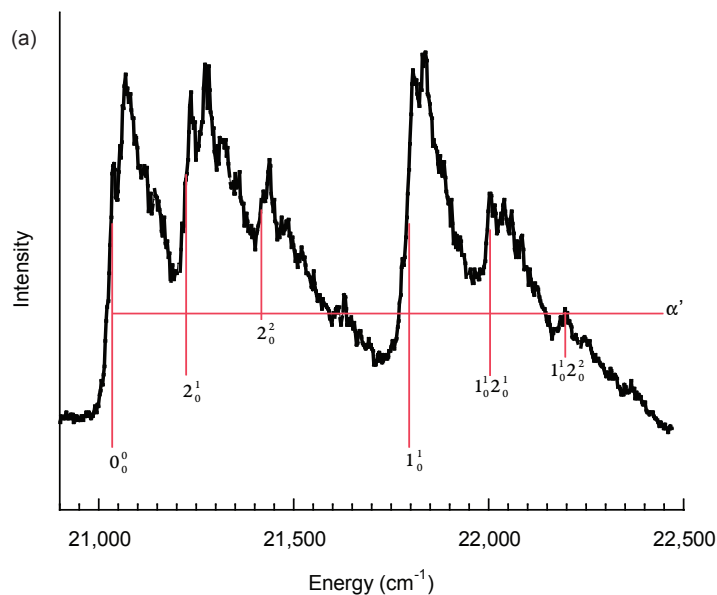
Fluorescence decay curves were also recorded for each of the bands in Figures 5.6 (b) and 5.7 (b). The lifetimes for the fluorescence induced by tunable excitation were almost identical to the ones for fixed frequency excitation. Because of lower dye laser power, the decay curves were much weaker and consequently are not shown.

5.5 Analysis and Discussion

5.5.1 Long-Lived Fluorescence

While the quick comparison of the long-lived fluorescence recorded here with the fluorescence observed by Goerller-Walrand[62] (Figure 5.1) would suggest this fluorescence was coming from UO_2Cl_2 there are some major problems with this as-

Excitation Spectrum from Vaporized UCl_4 in Ar
Recorded by Monitoring Long-Lived $18,122\text{ cm}^{-1}$ Fluorescence.



Long-Lived Fluorescence From Vaporized UCl_4
in Ar Induced by $21,076\text{ cm}^{-1}$ Excitation

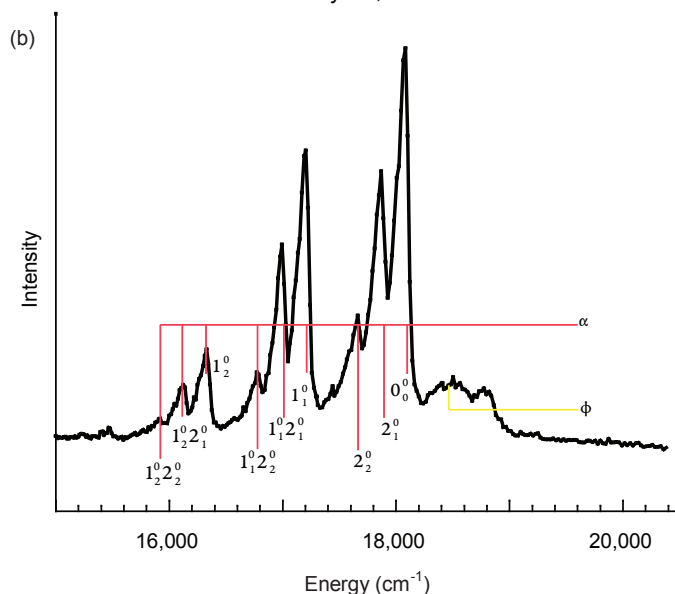
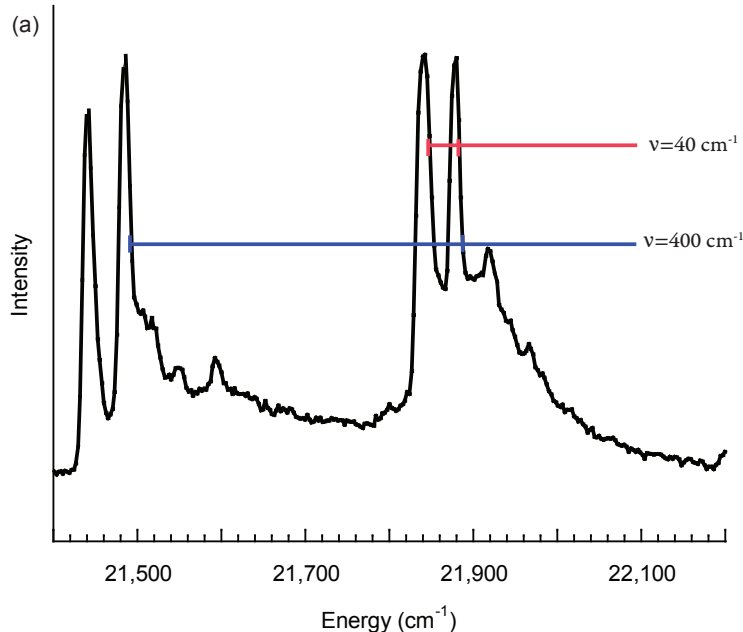


Figure 5.6: Excitation spectrum of thermally vaporized UCl_4 trapped in solid Ar recorded by monitoring long-lived fluorescence. (a) Excitation spectrum produced while observing $18,122\text{ cm}^{-1}$ fluorescence. Fluorescence recorded using a $15\ \mu\text{s}$ delay and a $20\ \mu\text{s}$ gate width with respect to the laser firing. A $\nu_1 = 760 \pm 20\text{ cm}^{-1}$ and a $\nu_2 = 360 \pm 20\text{ cm}^{-1}$ progression was observed for the excited state. (b) Fluorescence produced by $21,076\text{ cm}^{-1}$ excitation. Fluorescence recorded during the same time window as in (a). ϕ refers to the short-lived bands observed in the 355 nm induced fluorescence spectrum.

Excitation Spectrum from Vaporized UCl_4 in Ar
Recorded by Monitoring Short-Lived $18,832\text{ cm}^{-1}$ Fluorescence.



Short-Lived Emission from UCl_4 Induced by $21,487\text{ cm}^{-1}$ Excitation

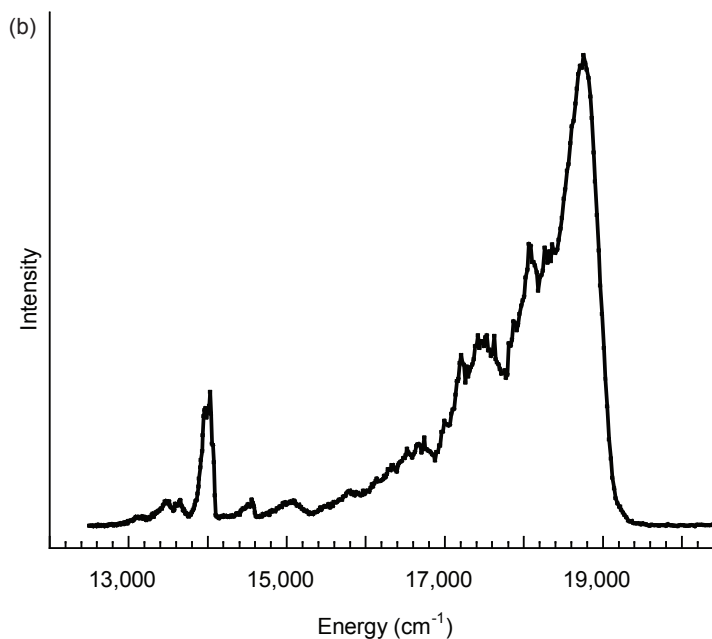


Figure 5.7: Excitation spectrum of thermally vaporized UCl_4 trapped in solid Ar recorded by monitoring short-lived fluorescence. (a) Short-lifetime wavelength selected excitation spectrum. Spectrum produced while observing $18,832\text{ cm}^{-1}$ fluorescence (ϕ). The spectrum was recorded with a $0.200\text{ }\mu\text{s}$ delay and a $0.300\text{ }\mu\text{s}$ gate width with respect to the laser firing. Intervals of $400\pm 18\text{ cm}^{-1}$ and $40\pm 3\text{ cm}^{-1}$ were observed. (b) Short-lived fluorescence induced by $21,487\text{ cm}^{-1}$ excitation. The spectrum was recorded with the same time window as in (a).

signment. First, the measured symmetric stretching frequency for UO_2Cl_2 in acetone is approximately 830 cm^{-1} . [62] This value is almost identical to the symmetric stretch (also about 830 cm^{-1}) measured by the same authors for $\text{UO}_2\text{Cl}_2(\text{TBP})_x$ (TBP=tributylphosphate) in methyl-*i*-butylketone. The symmetric stretch for the solvated molecules also is very close to the value reported by Barker *et al.* [78] for crystalline $\text{Cs}_2\text{UO}_2\text{Cl}_4$ ($\nu_1 = 832\text{ cm}^{-1}$). However, Krupa *et al.* [79] observed the symmetric stretch for single crystal UO_2Cl_2 at 875 cm^{-1} , though there was no mention of the discrepancy with the earlier crystalline experiments. What is clear is that the symmetric stretch reported here is some $15\text{-}60\text{ cm}^{-1}$ larger at $890\pm 7\text{ cm}^{-1}$ than all previous experiments. It seems highly unlikely that, if the symmetric stretching frequency remains virtually unchanged when going from an organic solvent to a crystal lattice, interactions with Ar in a matrix would produce such a shift. The second problem with assigning the long-lived fluorescence as coming from UO_2Cl_2 is the position of the $0' \rightarrow 0$ emission band. In the spectrum of UO_2Cl_2 in acetone [62], it appears at $20,136.9\text{ cm}^{-1}$. In Barker *et al.* [78] and Krupa *et al.* [79] it appears at $20,095\text{ cm}^{-1}$ and $20,549$ respectively. The energy for the same transition reported here is $18,122\text{ cm}^{-1}$. Again, with the shifting of the $0' \rightarrow 0$ emission band due to solvent or crystal field effects at most 454 cm^{-1} , it seems highly unlikely that interactions between UO_2Cl_2 and Ar would cause a $1,973\text{ cm}^{-1}$ shift.

With both UO_2Cl_2 and UCl_4 , unlikely candidates for producing the observed fluorescence, it is of interest to examine other possible intermediate compounds formed in the oxidation or hydrolysis of UCl_4 . Figure 5.8 was borrowed from a report by Hass of Oak Ridge National Laboratory [80] and shows the thermodynamic stability of all the possible compounds observed in the oxidation, reduction, and chlorination of U. From the figure, UOCl_2 , UOCl_3 , UOCl_4 , UO_2Cl , and UO_2 are all possible intermediates in forming UO_2Cl_2 , and hence, candidates for producing the fluorescence. The spectrum for UO_2 was discussed previously in Chapter 4 and is ruled out as the molecule pro-

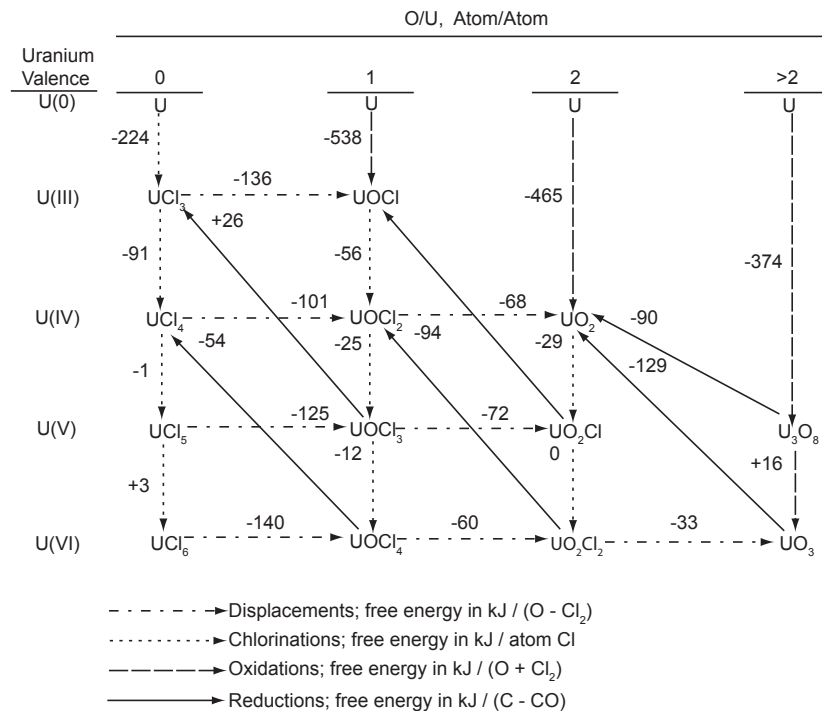


Figure 5.8: Conversion reactions for U-O-Cl compounds and free energy at 900 K.[80]

ducing this fluorescence. Also, as mentioned in Section 5.3, the experiments by Souter and Andrews[64] on the UO_2F_2 analogue are quite revealing. In those experiments the vibrational frequencies of UO_2F_2 and UO_2F in Ar, were reported as 939.6 and 867.8 cm^{-1} respectively. In this analogue to the U-O-Cl system it appears that removing a fluorine lowers the stretching frequency significantly. Therefore, UO_2Cl is ruled out as a carrier because the proposed molecule has one less chlorine and the symmetric stretching frequency observed here is greater than that of UO_2Cl_2 . Consequently, it is quite likely that the molecule producing the fluorescence has one less O than UO_2Cl_2 . In a 2006 paper, Goncharov *et al.*[81] reported the symmetric stretching frequency for UO^+ at approximately 912 cm^{-1} which is close to the $890 \pm 7 \text{ cm}^{-1}$ observed here. UO^+ can be considered the one oxygen analogue to UO_2^{2+} . While the remaining candidates each contain the UO subunit, looking at the free energies given in Figure 5.8, it is reasonable to say that fluorescence is coming from either UOCl_2 or UOCl_3

because the formation of UO_2Cl is more favorable than the formation of UOCl_4 . Additionally, the IR spectrum showed the R(0) line for HCl, a byproduct of the UCl_4 hydration reaction (Figure 5.2). Further support comes from a 1965 investigation by Selbin and Schober[82] of products derived from the hydrolysis of UCl_4 using IR spectroscopy. In the investigation UCl_4 was dissolved in deoxygenated water, the solution was heated, and the resultant vapor was investigated with IR spectroscopy. In the spectra several U-Cl complexes were observed, each complexed with OH and water. The molecule UOCl_2 was also observed, though all assigned vibrations to the UO stretch (719 cm^{-1}) were well below the value observed here ($890\pm 7\text{ cm}^{-1}$). It is quite possible that the amount of water vapor surrounding the UOCl_2 could cause a rather large redshift in the vibrational frequency. Unfortunately, most of the other experiments published concerning the decomposition of UCl_4 focused on the oxidation mechanism and not the hydrolysis mechanism. Consequently, more theoretical predictions are necessary to determine exactly how many Cl atoms are contained in the molecule.

It is also of interest that some IR and fluorescence spectra of thermally vaporized UCl_4 in Ar recently were recorded that were different from the ones reported here.[83] Lacking from the IR spectra is the pronounced symmetric and antisymmetric stretching frequency at 895 ± 0.5 and $972\pm 0.5\text{ cm}^{-1}$ respectively. What is observed is an IR vibration at $835\pm 0.5\text{ cm}^{-1}$. In the fluorescence spectra a strong progression reassembling the one seen by Goerller-Walrand *et al.* [62] begins at $20,290\text{ cm}^{-1}$ and shows a symmetric stretching frequency of $835\pm 2\text{ cm}^{-1}$. These spectra more closely resemble the spectra observed in previous experiments for UO_2Cl_2 [62, 79, 78], and have been assigned to that molecule. Further support comes from the fact that the lifetime for this new fluorescence is on the order of magnitude of $100\ \mu\text{s}$ versus $50\ \mu\text{s}$.

A closer examination of the 355 nm induced fluorescence spectrum (Figure 5.3 (b)) also supports the assignment of either UOCl_2 or UOCl_3 as the fluorescing molecule,

and the molecule will be referred to as UOCl_x in the future. In the figure, transitions from the first observed excited state to the ground state are labeled as α . Common spectroscopic notation is used for numbering the vibrational progressions contained in the α band system with 0_0^0 being the origin band. Nearly identical frequencies for both the ν_1 , UO stretch ($890 \pm 7 \text{ cm}^{-1}$), and ν_2 , UO bend ($150 \pm 20 \text{ cm}^{-1}$) are observed in the fluorescence induced by 355 nm and tunable (blue) radiation. The bands labeled β can then be assigned to transitions from a different excited state to a low-lying electronic state which is not the ground state. Unlike UO_2Cl_2 , UOCl_x contains lone pair electrons around the U, which can easily interact with chlorine p electrons to produce closely split low-lying states. The UO symmetric stretch of $865 \pm 7 \text{ cm}^{-1}$ for β is significantly different from the $890 \pm 7 \text{ cm}^{-1}$ measured for the α fluorescence, and it would be hard to explain this difference if the α and β transitions terminated on the same electronic state. Figure 5.9 shows the absorption and fluorescence scheme observed here for UOCl_x . The black arrow on the left represents the 308 nm excitation up to an excited state. Then the electron relaxes via non-radiative decay to either the α or β excited states from which fluorescence to either the ground state or another low-lying state is observed. Note that the absolute position of the pink arrow with respect to the blue one cannot be determined from the present data. However the β level is high enough above the α level that the fluorescence indicated by the pink arrow was not observed when the α electronic state was directly excited. The electronic excitations shown in the diagram are probably ligand to metal charge transfer excitations, where an O 2p electron is excited to a vacant metal orbital. More energy is required than produced by a single photon from the laser to excite a U electron to a vacant metal orbital. Additionally, this description can explain the relatively long lifetime of the UOCl_x fluorescence. During excitation an electron is promoted from a singlet state to a triplet state. The electron then becomes “trapped” in the triplet state, which leads to the long lifetime.

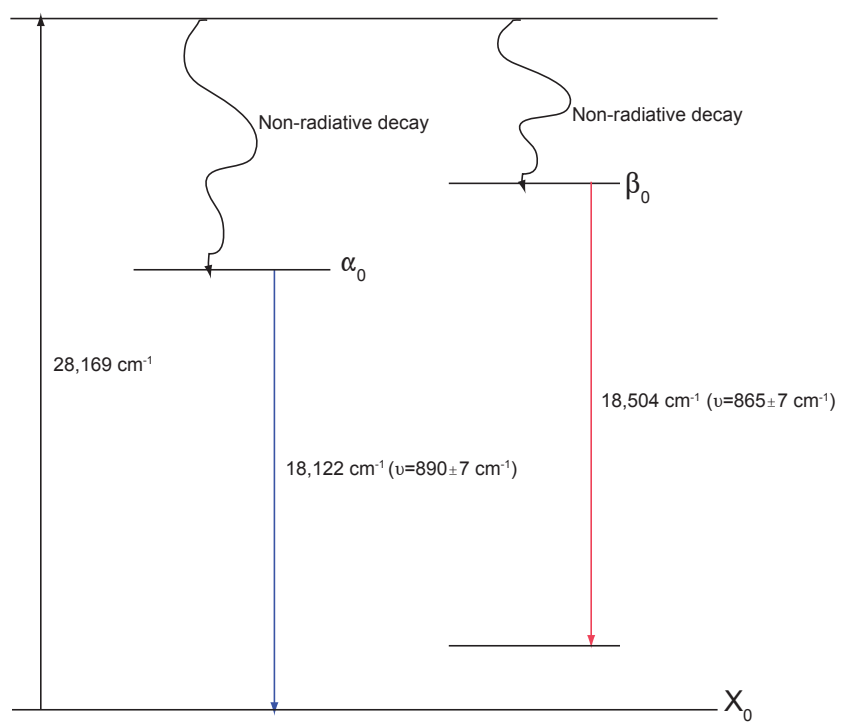


Figure 5.9: Energy level sketch of the absorption and fluorescence of UOCl_x .

5.5.2 Short-Lived Fluorescence

The assignment of the short-lived fluorescence is a little more tentative. Evidence that this fluorescence belongs to UCl_4 was drawn from (a) the lacking of a UO or OOU stretch in the fluorescence spectra and (b) the short lifetime ($\sim 1.5\mu\text{s}$) of the fluorescence. The $360\pm 8\text{ cm}^{-1}$ vibrational progression that is observed for the band at $19,390\text{ cm}^{-1}$ does not match any of the predicted UCl stretches for UO_2Cl_2 predicted at 326 and 332 cm^{-1} . [84]. And, while there are no predictions for UCl stretches in UOCl_x , one would expect the frequencies to be similar to the UCL stretches UO_2Cl_2 . Rather, the frequency is much closer to the 355 cm^{-1} IR absorption measured by Hunt *et al.*[2] for UCl_4 . Unfortunately, the vibrational frequencies for ground state of UCl_4 could not be measured here directly using IR spectroscopy because of the limited range of the MCT detector. The above findings make it highly unlikely that the short-lived fluorescence comes from UO_2Cl_2 or UOCl_x . This unlikelihood combined with studies on the decomposition of UCl_4 [63, 85] makes UCl_4 the most probable fluorescing species. The short-lived fluorescing species at $21,115\text{ cm}^{-1}$ may also be coming from UCl_4 because it has the same lifetime. However, an excitation spectrum similar to the one recorded for the $19,390\text{ cm}^{-1}$ fluorescence should be observed for this feature. Unfortunately, due to experimental conditions, the scattered light from the dye laser was too great at $21,115\text{ cm}^{-1}$ to record an excitation spectrum. New experiments are planned to resolve this problem, which will include better filters to block laser scatter and realignment of the optical path so that the most intense scattered light is slightly off the axis of the fluorescence focused into the monochromator.

As for a detailed analysis of the short-lived fluorescence emission and excitation spectra, there has been very little theoretical investigations concerning UCl_4 . For the spectra of UO_2 presented earlier, it would have been impossible to assign the electronic states involved in the fluorescence without such predictions. The spacing ($1,725\text{ cm}^{-1}$) between the two band systems assigned to UCl_4 (Figure 5.4) is large

enough that the most probable explanation is that the fluorescence is coming from two different upper states. All the vibrational modes of UCl_4 are much too low in energy for this spacing to be related to vibrations. Additionally, UCl_4 is a closed shell molecule for which it would be unusual to find closely spaced low-lying electronic states. As was observed for UOCl_x , it is possible for emission from different excited states to have lifetimes indistinguishable by the method used here to record decay curves and calculate lifetimes. Unfortunately, without theoretical predictions it is nearly impossible to determine the actual states involved in the fluorescence. It is hoped that when this work is eventually published, it will inspire theoreticians to perform more calculations on the electronic energy levels of uranium chlorides.

Lastly, there are three short-lived red fluorescence bands yet to be discussed. If the primary matrix isolated species identified so far that are capable of fluorescing are UCl_4 and UOCl_x , it would be appealing to assign these bands to UCl_4 based solely on a lifetime argument. The frequency measured between the blue most peaks in Figure 5.3 is $565 \pm 8 \text{ cm}^{-1}$, while the other observed frequency is $524 \pm 8 \text{ cm}^{-1}$. The observed anharmonicity of the vibrational progression is unusual because as one goes higher in energy within the potential the vibrational interval often decreases slightly. Also, there are no vibrational modes predicted for UCl_4 above 360 cm^{-1} , and exciting a combination of modes would require at least 600 cm^{-1} . Based on the lifetime measurements, it is also just as unlikely that UOCl_x is the fluorescing species, though there are no theoretical predictions for the vibrations of these molecules. Unfortunately, the assignment of this red fluorescence to UO_2Cl_2 is just as troubling. There are no modes predicted by Pitzer[84] which could be assigned to this progression. And in the new spectra assigned to UO_2Cl_2 , these bands are not present.[83]

5.6 Conclusion

A detailed analysis of the fluorescence spectra from the products of thermally vaporized UCl_4 isolated in solid Ar has been presented. The fluorescence spectra reported here appear to be from two different carriers, UOCl_x and UCl_4 . The UOCl_x fluorescence is long-lived ($55.6 \pm 0.07 \mu\text{s}$) and shows a OU stretch of $890 \pm 7 \text{ cm}^{-1}$. The OU symmetric stretch is a common feature to the fluorescence observed from all molecules containing U and O. While it is easy to rationalize the transitions giving rise to the fluorescence, more theoretical predictions are necessary to confirm the number of Cl atoms in the molecule and the exact electronic states involved.

Based on the current understanding of the decomposition of UCl_4 the most probable candidate for the carrier of the shorter lived fluorescence ($1.2 \pm 0.004 \mu\text{s}$) is UCl_4 . There are no high frequency modes observed in this fluorescence common to fluorescence from molecules containing U and O. While this may be the first report of UCl_4 fluorescence, there are many anomalies in the fluorescence spectra from UCl_4 that warrant further investigations. Additionally the theoretical predictions for the electronic levels of the UCl_4 are scarce compared to those published for UO_2Cl_2 , which makes the interpretation of the spectra all the more challenging. It is hoped that data from electronic structure calculations for UCl_4 will be available to guide future experiments.

Chapter 6

UO₃ and Higher Order Oxides

6.1 Introduction

Most of the gas phase and MI experiments pertaining to uranium oxides have focused on UO and UO₂. The higher order uranium oxides such as UO₃ have not received the same attention in terms of spectroscopy. Unlike UO₂, there is only a handful of papers in the literature pertaining to the gas phase spectra of UO₃. While the dominant fluorescence in Chapter 4, obtained by ablating a target comprised of uranium turnings, was attributed to UO₂, an attempt was made here to observe fluorescence from higher order oxides. The idea was that adding more oxygen to the Ar gas mixture would favor the formation of higher order oxides. With an increase in O₂ concentration during ablation, a likely candidate formed from the ablation of U metal in the presence of O₂ is UO₃, if not only because it is a neutral molecule containing three O atoms and because it is stable under atmospheric conditions. It is of interest to note the proposed structure of UO₃ as shown in Figure 6.1. In terms of the electronic structure, UO₃ consists of an uranyl cation (UO₂²⁺) subunit perturbed by an association with an O₂²⁻ anion. In Chapter 5, the concept of the uranyl ion was introduced as a dominant feature in the spectroscopy of molecules containing O and

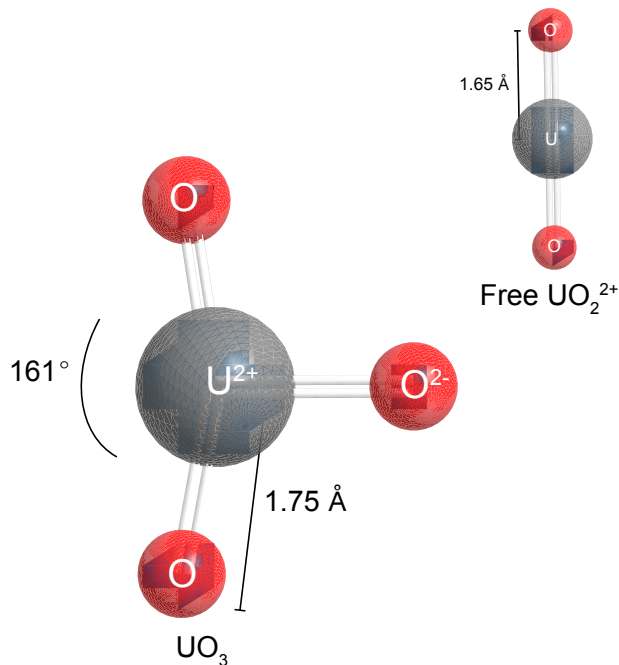


Figure 6.1: Predicted geometry of UO_3 . The insert shows the geometry of isolated UO_2^{2+} for comparison.

U using uranyl chloride as the example molecule. Here one can envision replacing the chlorine atoms of uranyl chloride with an additional O. Figure 6.1 shows the predicted geometry of UO_3 . The original calculations by Pyykkö *et al.*[7] predicted that one of the UO bonds was longer, but more recent calculations by Zhou *et al.* [8] predict equal UO bond lengths. Also note that the geometry of UO_2^{2+} in UO_3 is no longer linear, but rather bent by approximately 20° .

The first spectroscopic identification of UO_3 was in the FTIR study of the products of U, thermally vaporized at 1,800 K in the presence of O_2 , isolated in solid Ar.[86, 56, 87] The first two papers published from this study focused on the stretching frequency region of the IR spectrum. The geometry of UO_3 was proposed as T-shaped, belonging to the C_{2v} point group, and the frequencies of three modes were calculated to be: $\nu_1(A_1) = 843.5(0)$, $\nu_2(A_1) = 746.2(0)$, and $\nu_4(B_1) = 852.7(5) \text{ cm}^{-1}$. [86, 56] The latter two also were measured experimentally using an FTIR with $\nu_2 = 745.6(5)$ and $\nu_4 = 852.6(0) \text{ cm}^{-1}$. Assignments were made with the help of isotopic substitution. In

the third paper, three low frequency vibrational modes (C_{2v} symmetry) were observed: $\nu_3(A_1) = 186.2(1)$, $\nu_5(B_1) = 211.6(1)$, and $\nu_6(B_2) = 151.5(1)\text{cm}^{-1}$. [87] Over a decade later, Hunt *et al.* studied the products of ablated $\text{U} + \text{O}_2$. [47] Among the UO_2 bands discussed in the previous section, he found that the two observed bands for UO_3 (852.5 and 745.5 cm^{-1}) were in good agreement with earlier experiments.

The IR experiments above provided useful data about the ground state geometry of UO_3 , but IR experiments in general cannot provide direct information about the electronic structure of a molecule. Instead, IR spectra can be compared with theoretical predictions of the vibrational frequencies for various low-lying electronic states. This comparison can lead to the assignment of the ground electronic state of the molecule, but does not provide information concerning other low-lying excited states. Therefore, it is necessary to complement IR spectroscopy with electronic spectroscopy to obtain sufficient data to thoroughly test calculations. In the case of UO_3 , no fluorescence spectra for either the gas phase or matrix isolated molecule have been reported in the literature. The following experiments were an attempt to survey the low-lying electronic states of uranium oxides. While UO_3 is likely to be observed in the spectra, as mentioned previously, it is very hard to control what products are formed during laser ablation. What can complicate matters further is that many U compounds containing O all contain subunits closely resembling the uranyl ion, which in turn can make the spectra very similar for all such compounds.

6.2 Experiment Details

A uranium rod (Oak Ridge National Laboratory) was used as a source of uranium atoms. The rod was fed into the matrix chamber through the glass tube of the sample fill line described in Section 2.3.2.1. During the ablation, the U atoms were

mixed with an effusive flow (approximately 3mmol/h) of a gaseous O₂ / Ar mixture. The oxygen in most of the experiments was not enriched and contained only the natural abundance (0.2%) of ¹⁸O. Later, though, enriched O₂ (20% ¹⁸O) was used as is evident in the IR spectrum shown in the following section. The materials were deposited for 3 hours onto the cold CsI substrate. Matrices were made with different O₂/Ar concentrations ranging from 0.1% to 2%. The spectra described here were from matrices with a 1% O₂/Ar concentration. Immediately following deposition, IR absorption measurements were made. Afterward, the matrices were excited using light from various pulsed laser sources. IR absorption measurements also were made later to observe the effects of photolysis.

6.3 Results

6.3.1 Infrared Absorption Spectra

Figure 6.2 shows the IR absorption spectrum recorded after deposition of an U+¹⁸O₂/¹⁶O₂ (1/5)/ Ar mixture as well as the IR absorption spectrum recorded following a minimum of 1 hr UV photolysis. The various species observed were assigned using the spectra recorded by Andrews and colleagues.[47] The black trace was recorded immediately following deposition. The purple trace was recorded after one hour of 266 nm photolysis. No quantitative measurements were made for the IR absorptions because the signal strength is so sensitive to alignment conditions and the extra effort required to make such measurements would not provide much useful data. Qualitatively, though, the absorption belonging to UO₃ is unchanged after photolysis. The absorption belonging to UO₂ decreases, while there is an increase in the absorptions for the complex (UO₂)²⁺(O₂)²⁻. Figures 6.3 and 6.4 show an enlargement of the (UO₂)²⁺(O₂)²⁻ and UO₃ stretching regions respectively.

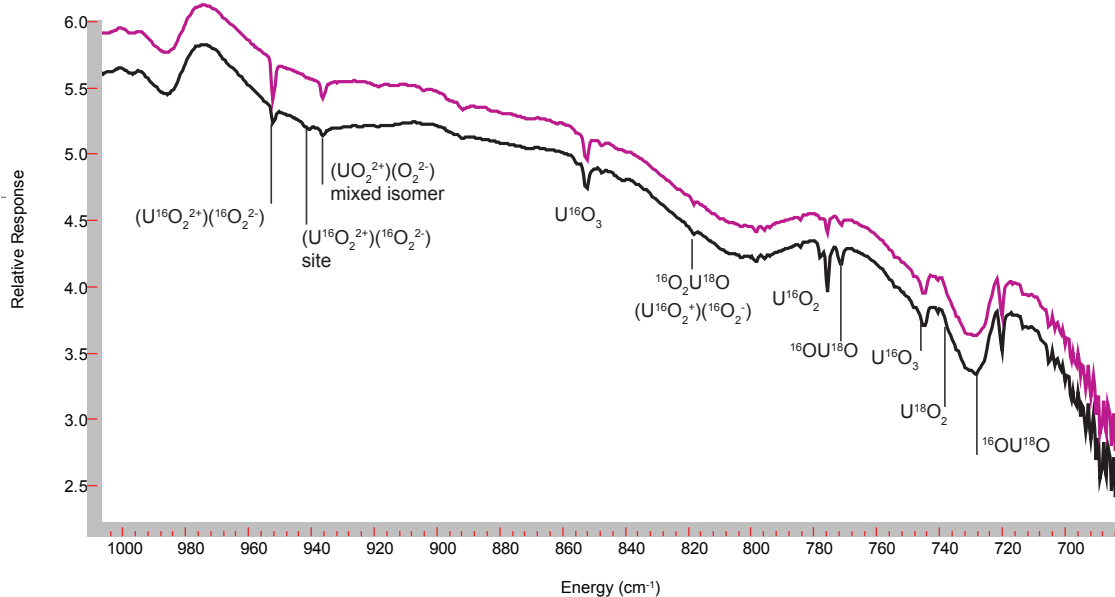


Figure 6.2: IR absorption spectra for ablated U + $^{18}\text{O}_2/^{16}\text{O}_2$ (1/5) in Ar. The black trace was recorded immediately following deposition. The pink trace was recorded after one hour of 266 nm photolysis. Note that the absolute response for the pink trace has been shifted for ease in distinguishing the two spectra. Assignments based on spectra recorded by Hunt *et al.*[47]

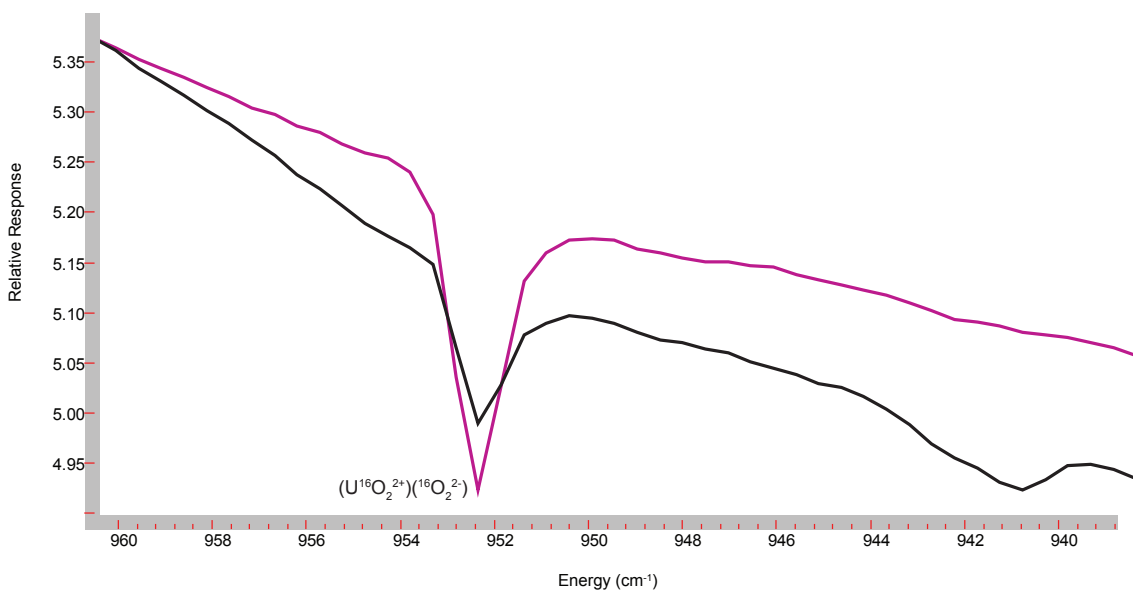


Figure 6.3: Enlargement of the $(\text{UO}_2)^{2+}(\text{O}_2)^{2-}$ stretching region.

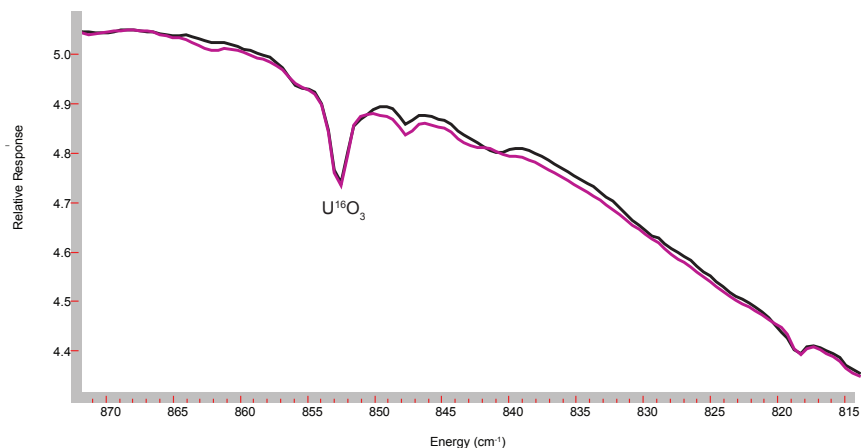


Figure 6.4: Enlargement of the UO_3 stretching region.

6.3.2 Fixed Wavelength Excitation

Laser excitation of the matrix at 355, 308, and 266 nm produced an emission spectrum with long lived fluorescence that consisted of a group of resolved features in the 16,300-13,000 cm^{-1} range. While the shape of the observed features was the same for all three wavelengths, 308 nm excitation induced stronger fluorescence than the other two wavelengths, and the fluorescence spectrum induced by 308 nm radiation is shown in Figure 6.5. The bands show 849 ± 8 and 292 ± 8 cm^{-1} progressions. It is worth noting that progressions were not harmonic and exhibited different spacing between the different vibrational levels as labeled in Figure 6.5. Also, the peaks to the left of the α_2 band are probably a continuation of the α and β progressions, but were too weak to be accurately labeled. No attempt was made to observe short-lived fluorescence (ns) similar to what was observed for UO_2 as described in Section 4.3.1 because it was best induced by 266 nm radiation, which also produced short-lived (ns) interfering fluorescence from the CsI substrate. Fluorescence decay curves were recorded for all the bands shown in Figure 6.5. All the peaks had similar lifetime of approximately 59.6 ± 0.1 μs . Figure 6.6 (a) shows a typical decay curve for fluorescence induced by 266 nm radiation.

Long-Lived Fluorescence Induced by 308 nm Radiation

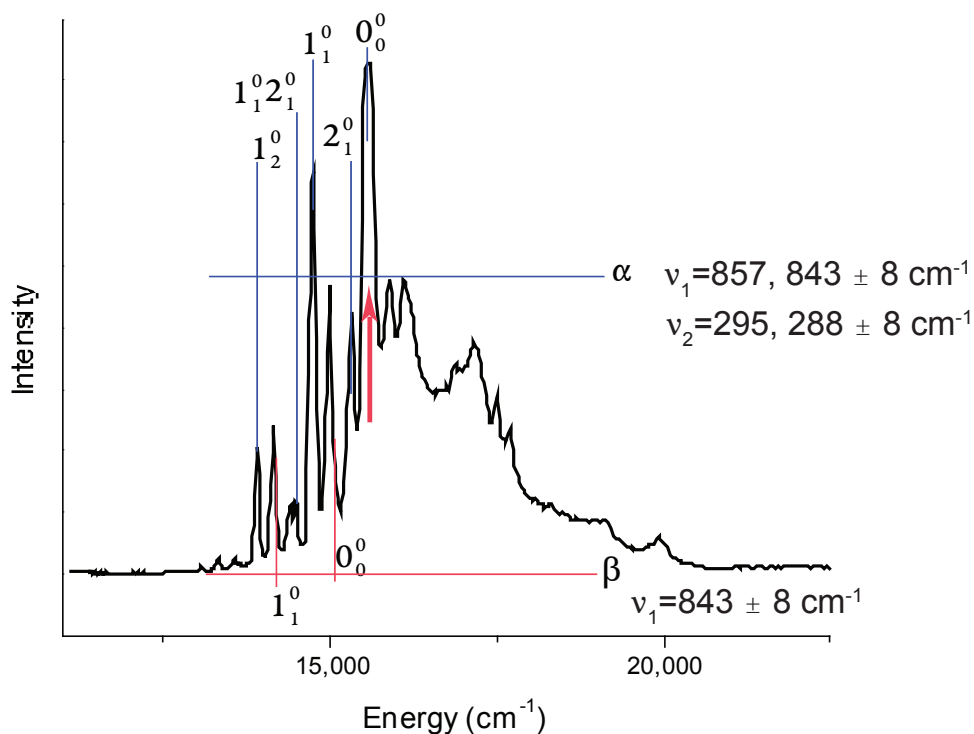


Figure 6.5: Long-lived fluorescence from ablated U + 1% O₂ in Ar induced by 308 nm radiation. α bands represent emission from the first observed electronically-excited state, while the β bands are emission from the second observed electronically-excited state. The pink arrow indicates the energy of the observed fluorescence in the excitation spectrum shown in Figure 6.7 (a).

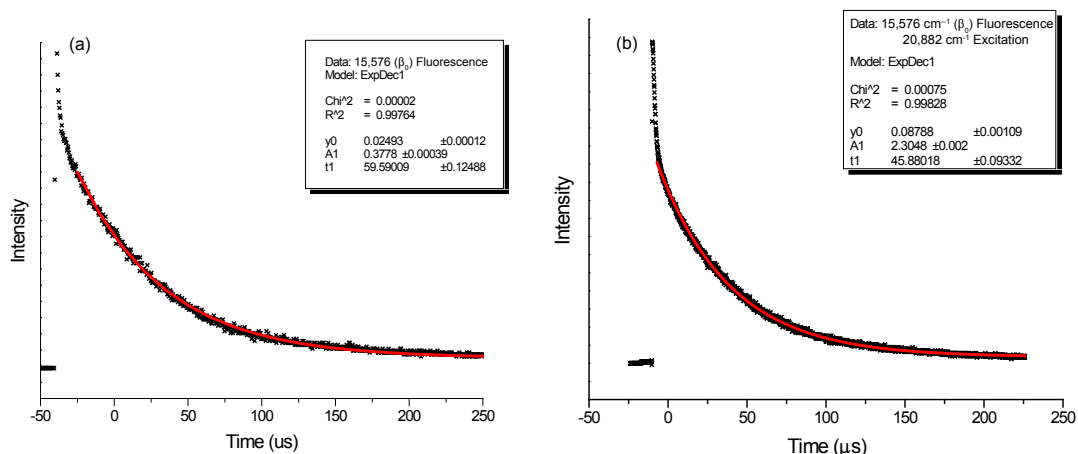
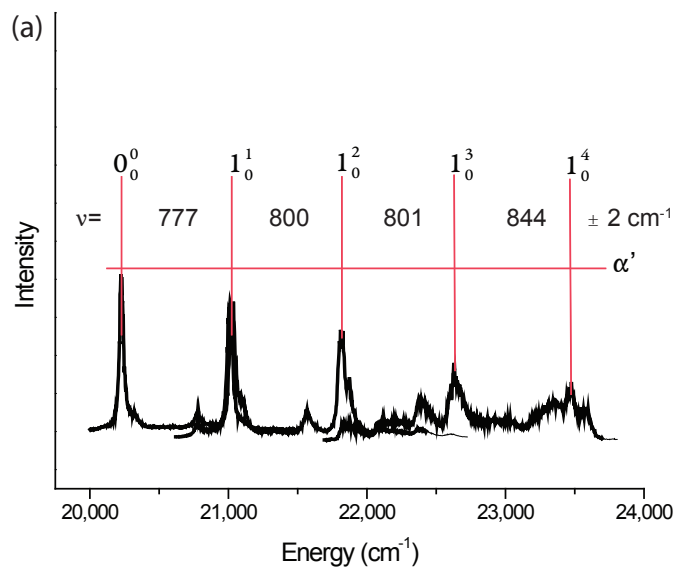


Figure 6.6: Lifetimes of fluorescence from ablated U + 1% O₂ in Ar. (a) 15,576 cm⁻¹ (α_0) fluorescence induced by 308 nm radiation has a lifetime of 59.6 μ s. (b) 15,576 cm⁻¹ (α_0) fluorescence induced by 20,882 cm⁻¹ radiation has a slightly shorter lifetime of 45.9 μ s.

6.3.3 Tunable Excitation

Tunable laser excitation was used to investigate the excited levels that gave rise to the long-lived emission bands shown in Figure 6.5. Wavelength selected fluorescence excitation spectra were recorded by scanning the excitation wavelength while monitoring the light emitted by the center of the α_0 emission band ($15,566\text{ cm}^{-1}$). α_0 was chosen because it was the most intense band in the emission spectra. The excitation spectrum (Figure 6.7 (a)) contains a vibrational progression beginning at $20,210\text{ cm}^{-1}$ with an $806\pm 2\text{ cm}^{-1}$ spacing. As in the fixed frequency UV excitation spectrum, the progression is not harmonic, and the frequencies for the spacing between the various vibrational excited states are labeled in Figure 6.7 (a). Exciting the matrix at any of the excitation peaks produced the same fluorescence observed with fix frequency UV radiation (Figure 6.7 (b)), though much weaker because of the lower power of the dye laser compared with the excimer laser. Fluorescence decay lifetimes were also measured for each of the peaks in Figure 6.7 (a). All of the peaks had similar lifetimes around $45.8\pm 0.1\ \mu\text{s}$. Figure 6.6 (b) shows a typical decay curve using tunable excitation. While the lifetimes as determined by the least squares fitting procedure are significantly different for the fixed frequency and tunable excitation, the reported error limits are only for the least squares fitting and not other systematic error which was usually estimated to be $\pm 10\ \mu\text{s}$. All the observed emission and excitation peaks are listed in Table 6.1 and are labeled using the notation described in the discussion section. One should note that the energies listed in the table are for the blue edge of the indicated emission band and the red edge of the indicated excitation band because the observed bands were so broad. However, the band centers were used when obtaining wavelength selected excitation spectra. Also, the peaks, corresponding to a combination of the stretching mode and one quanta of the bending mode for the β electronic state, overlap the stretching progression for the α state and are not labeled on the spectrum or listed in the table.

Excitation Spectra Recorded by Monitoring Long-Lived Fluorescence



Long-Lived Fluorescence Induced by 21,022 cm⁻¹ Radiation

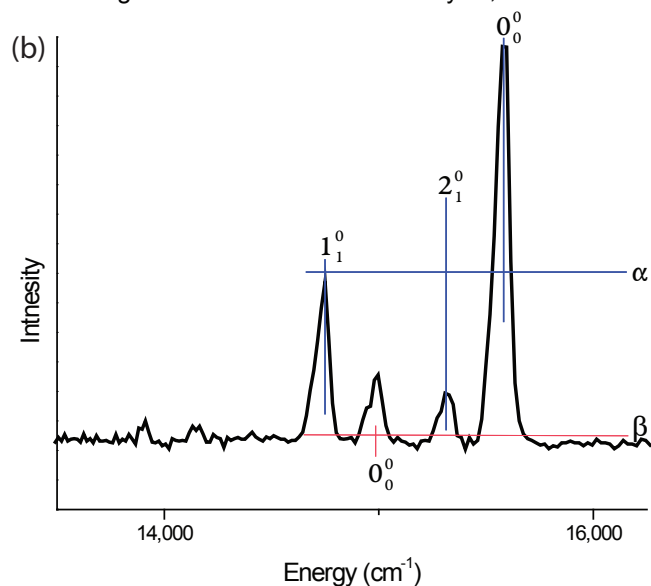


Figure 6.7: Excitation spectra of ablated U + 1% O₂ in Ar recorded monitoring long-lived fluorescence. (a) Excitation spectrum produced with various dyes in the blue and violet regions of the spectrum while observing the center of the α_0 fluorescence (15,566 cm⁻¹) indicated by the arrow in Figure 6.5. The 1_1^0 band was excited and the fluorescence in Figure (b) was recorded.

Emission			Excitation		
Peak ($\pm 8 \text{ cm}^{-1}$)	Assignment		Peak ($\pm 2 \text{ cm}^{-1}$)	Assignment	
15,654	0_0^0	α	23,433	1_0^4	α'
15,359	2_1^0	α	23,256		
15,033	0_0^0	β	22,589	1_0^3	α'
14,797	1_1^0	α	22,344		
14,509	1_1^0 2_1^0	α	21,788	1_0^2	α'
14,196	1_1^0	β	21,544		
13,954	1_2^0	α	20,988	1_0^1	α'
			20,755		
			20,211	0_0^0	α'

Table 6.1: UV/visible bands from ablated U +1% O₂ in Ar.

6.4 Analysis and Discussion

Evidence that the emitting species observed in these experiments was $(\text{UO}_2)^+(\text{O}_2)^-$ was drawn from a comparison of the IR spectrum with a similar spectrum recorded by Andrews *et al.*[47], and then, correlating the IR spectrum with the visible fluorescence spectra induced by 308 nm radiation and the wavelength selected fluorescence excitation spectra (Figures 6.2, 6.5, and 6.7). As was previously mentioned, Andrews produced primarily UO, UO₂, UO₃, the $(\text{UO}_2)^+(\text{O}_2)^-$ complex, and the $(\text{UO}_2)^{2+}(\text{O}_2)^{2-}$ complex by ablating U in an Ar/O₂ mixture. Because the fluorescence spectra did not show evidence of UO or UO₂, the observed bands were presumed to be coming from UO₃, $(\text{UO}_2)^+(\text{O}_2)^-$, or $(\text{UO}_2)^{2+}(\text{O}_2)^{2-}$. Unfortunately, the vibrational frequency of $849 \pm 8 \text{ cm}^{-1}$ observed in the visible fluorescence spectrum (Figure 6.5) could be assigned to any of the three molecules within the error limits of matrix broadened line

widths. Therefore, photolysis experiments were used to help identify the molecule that gave rise to the fluorescence. The change in intensities of the IR absorptions after photolysis for the spectrum in Figure 6.2 did not match the changes reported by Hunt *et al.*[47] In their experiments, Hunt *et al.* observed a roughly 20% increase in the absorptions belonging to UO_2 and $(\text{UO}_2)^{2+}(\text{O}_2)^{2-}$ after 30 min UV photolysis. The increase in UO_3 absorptions was a marginal 10%, while there was a decrease of about 50% for the $(\text{UO}_2)^+(\text{O}_2)^-$. Here, in contrast, after photolysis, the IR absorptions belonging to UO_2 decreased. There was no obvious change in UO_3 absorptions. Also, the absorptions in the proper position to be assigned to $(\text{UO}_2)^+(\text{O}_2)^-$ were initially so weak that neither a definite assignment could be made nor could an observed change after photolysis be observed. The only similarity between this work and Hunt *et al.* was the increase in the $(\text{UO}_2)^{2+}(\text{O}_2)^{2-}$ absorptions. For the fluorescence spectra, despite efforts to keep experimental conditions constant, it was not possible to determine if there was any change in fluorescence intensity after photolysis without modifying the experimental setup to allow direct measurement of the excitation laser power, because the change should have been small based on the IR spectra recorded for this work. In the experiments presented here, it was not warranted to make such modifications. With the discrepancy between this work and the work by Hunt *et al.* and the uncertainty in fluorescence intensity in this work, photolysis experiments could not be used to determine the fluorescing species. Therefore, a closer investigation of the fluorescence spectra was needed to determine the fluorescing species.

The fluorescence spectrum in Figure 6.5 is labeled as follows: transitions from an excited upper state to the ground state are labeled as α ; transitions from the same upper state to a low-lying excited state are labeled β . Common spectroscopic notation is used for numbering the vibrational progressions contained in both the α and β band systems with 0_0^0 being the origin band. α emission is long lived (50 μs) and shows the O-U-O symmetric stretch frequency between 847 ± 8 and 855 ± 8 cm^{-1}

and a low frequency bending progression between 288 ± 8 and 295 ± 8 cm^{-1} . The β emission has a similar lifetime and also exhibits the symmetric stretch. The label α' is used for the progression in the excitation spectrum because the observed fluorescence was the α_0 band in the fluorescence spectrum induced by fixed frequency radiation, though the spectrum could also have been recorded while observing the β_0 line. An indication of the fluorescing species was the observation of the 292 ± 8 cm^{-1} bending mode. Section 6.1 discussed the known vibrational modes of UO_3 . The vibration in question here does not fit any of those modes. Also, both α and β emission have a similar lifetime, which indicates a common upper state that gives rise to the fluorescence rather than two upper states and a common ground state. Because UO_3 is a closed shell molecule, it would be very hard to rationalize how it would have some closely spaced low-lying electronic states. $(\text{UO}_2)^{2+}(\text{O}_2)^{2-}$ is also a closed shell species and would probably not have two closely spaced low-lying electronic states. Alternatively, the interaction between an oxygen 2p electron and a metal 5f electron in $(\text{UO}_2)^+(\text{O}_2)^-$ could cause closely split low-lying electronic states. Consequently, $(\text{UO}_2)^+(\text{O}_2)^-$ is the most probable fluorescing species. What is troubling with this assignment is that the presence of $(\text{UO}_2)^+(\text{O}_2)^-$ in the matrix could not be confirmed with the IR spectra. This finding is not all that surprising after the fact that the results of the photolysis experiments do not match the results reported by Hunt *et al.*[47] Additionally, many species may have a fluorescence quantum yield that is much greater than the IR absorption strength, which makes it possible to observe fluorescence from species not seen in the IR spectra.

There are no explicit theoretical predictions for the electronic states of $(\text{UO}_2)^+(\text{O}_2)^-$ and the predictions for the electronic structure of the closed shell $(\text{UO}_2)^{2+}(\text{O}_2)^{2-}$ complex cannot be used for a comparison. However, it is expected that the excitations that give rise to the fluorescence are charge transfer transitions occurring from an occupied oxygen 2p orbital to a vacant metal centered orbital. Direct excitation of

a metal centered electron would require much more energy than could be found in a single photon from any of the lasers used here. Alternatively, the oxygen 2p electrons lie much closer in energy to a vacant metal orbital. This charge transfer causes the reduction in the stretching frequency from $848 \pm 8 \text{ cm}^{-1}$ in the ground state to $806 \pm 2 \text{ cm}^{-1}$ in the excited state (see Table 6.2). Denning's methodology[88] used to explain the charge transfer excitations in CsUO_2Cl_4 is also applicable to $(\text{UO}_2)^+(\text{O}_2)^-$. Denning says that electronic excitations for CsUO_2Cl_4 occur by promoting an O 2p (either $\sigma_u, \sigma_g, \pi_u$, or π_g) electron to an empty U orbital (δ_u or ϕ_u). Specifically in the visible region of the spectrum a σ_u electron is promoted, which weakens the UO bond, thus causing a lower stretching frequency.

While there have been no explicit calculations for the electronically excited levels of $(\text{UO}_2)^+(\text{O}_2)^-$, Zhou *et al.* [8] published theoretical predictions for the ground state stretching frequencies for $(\text{UO}_2)^+(\text{O}_2)^-$ to complement their IR spectra of uranium oxides isolated in solid Ne. Calculations were carried out using the B3LYP variant of DFT. Table 6.2 compares the calculated frequencies with experiment. It should be noted that Zhou *et al.* did not provide frequencies for the low frequency modes. Consequently, there is no assigned symmetry to the $292 \pm 8 \text{ cm}^{-1}$ mode observed in the fluorescence spectra. Also, it should be noted that the calculations are for isolated gas phase species and do not take into account matrix effects as is evident by comparing the calculated versus the experimentally measured frequency for the b_2 mode. Therefore, it is surprising to find the frequency for the a_1 mode measured in this work in such good agreement with the theoretical prediction. Further calculations are necessary to confirm all the observable frequencies for $(\text{UO}_2)^+(\text{O}_2)^-$.

Lastly, there are some features in the fluorescence spectrum induced by 308 nm radiation (Figure 6.5) and in the wavelength selected excitation spectrum (Figure 6.7 (a)) that have not been discussed. Among them is the broad fluorescence that lies higher in energy ($\nu > 15,700 \text{ cm}^{-1}$) in the 308 nm induced spectrum. This fluorescence

Mode	Frequencies	
	Calculated (cm ⁻¹)	Experiment (cm ⁻¹)
		292 ± 8 ^b
a1	529 ^a	
a1	854 ^a	848 ± 8 ^b / 806 ± 2 (excited state) ^b
b2	925 ^a	892.3 ^c , 886.1 (site) ^c
a1	936 ^a	

(a)= reference [8]; (b)= this work (fluorescence); (c)= references [47];

Table 6.2: Comparison of experimentally observed (UO₂)⁺(O₂)⁻ vibrations with theory. Modes are labeled assuming c_{2v} symmetry. All frequencies are for the ground state unless otherwise indicated.

was not observed in the 21,022 cm⁻¹ induced spectrum shown in Figure 6.7 (b), and hence that region of the spectrum was not shown. It also is worth mentioning that the choice of excitation wavelengths in the blue and violet region was because of the known spectral properties of the UO₂²⁺ subunit, which is a common fluorescing subunit of many uranium oxide molecules. No effort was undertaken to scan further into the UV while attempting to observe the $\nu > 15,700$ cm⁻¹ fluorescence. The other unassigned features are some bands in the tunable excitation spectrum (see Table 6.1). The spacing between these bands do not fit with a bending progression in the excited state. More spectroscopic studies are necessary to determine the nature of these bands.

6.5 Conclusion

The low-lying electronic states for what is presumed to be (UO₂)⁺(O₂)⁻ isolated in solid Ar have been mapped using UV/VIS fluorescence spectroscopy. While there were

no explicit calculations predicting the electronic energy levels for $(\text{UO}_2)^+(\text{O}_2)^-$ the assignment was made by eliminating other possible candidates based on experiments and theoretical predictions for the uranyl ion. Further theoretical studies are needed to fully interpret the fluorescence spectra presented here. Also, investigating the blue most absorption bands using REMPI coupled with a mass spectrometer should help identify the mass of the fluorescing species. A major complication in this experiment is that $(\text{UO}_2)^+(\text{O}_2)^-$ and other charged species may only be stable when frozen in a matrix and may not be observed in gas phase spectroscopy. Therefore, it is possible that $(\text{UO}_2)^+(\text{O}_2)^-$ may not be observed in REMPI experiments, but could still exist in a rare gas matrix. A final important point from these experiments is that they demonstrate how critical experimental conditions are when forming a matrix and when recording spectra. Evidence of this point is shown in the correlation of IR spectra taken for this work with the spectra recorded by Andrews *et al.*[47, 8] Though a useful tool in MI spectroscopy, IR spectroscopy cannot always be used to identify the fluorescing species in a matrix.

Chapter 7

Uranium Fluorides

7.1 Introduction

The 6+ oxidation state of U found in UF_6 is the most common oxidation state of U. Except for being hygroscopic, UF_6 is very stable. As mentioned in Section 3.1, UF_6 was the molecule used for enriching uranium because it is easily vaporized making it suitable for mass isotope separation. As a result, huge waste containers of depleted UF_6 remained, which made the material readily available for scientific experiments. [Obtaining a small quantity (50g), though, for a spectroscopic study proved much more challenging than obtaining a 50 gal drum]. LIF spectra of UF_6 isolated in solid Ar were recorded in the late 1970's by Andrews and colleagues.[1, 89] However, there was no such study of the electronic spectra for the fragmented UF_6 , namely UF_x ($x < 6$). IR spectra, though, were recorded by Andrews in the 1990's for a variety of actinide compounds including UF_x isolated in solid Ar, formed by ablating U atoms in an Ar/ F_2 mixture.[2]

To complement the experimental studies mentioned in the previous paragraph, researchers have performed several *ab initio* studies on UF_6 and UF_x dating back as early as the late 1970's.[90, 91, 92, 93] The first of these studies examined UF_5 .[90]

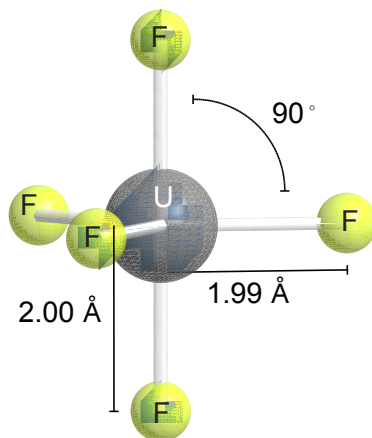


Figure 7.1: The geometry of UF_5 . [90]

In the study, Wadt and Hay found two possible geometries for the ground state, C_{4v} and D_{3h} . Calculations including spin orbital coupling concluded that the D_{3h} geometry was roughly 350 cm^{-1} lower in energy. However, the geometry easily can fluctuate between C_{4v} and D_{3h} with only small amounts of internal energy. Wadt and Hay's predicted structure for the D_{3h} geometry is shown in Figure 7.1. Note that the geometry was optimized without spin-orbit coupling. The ground state for this geometry was calculated to be $^2E''$. The authors also note that while the lowest energy transitions are $f \rightarrow f$ and are dipole forbidden for the U atom, most are allowed for the molecule. Unlike many of the other actinide containing molecules, there are allowed low-lying metal centered transitions for UF_5 .

Over two decades later, Federov *et al.* [92] reported *ab initio* theoretical predictions for the lowest 18 Ω levels of UF. The calculations, SO-CASCI, predicted $^6\Lambda_{11/2}$ as the ground state. Unfortunately, Federov *et al.* did not report any information on the transition probabilities between the low-lying states, quite possibly because there had been little published on the electronic spectrum of UF at the time. Fluorescence spectra are still necessary to obtain spectroscopically a complete picture of the low-lying electronic states and to test the theoretical predictions. The primary goal for the experiments presented here was to create a low resolution spectral map for studying

the low-lying electronic states of UF_x , which could guide future gas phase experiments.

7.2 Experiment Details

There are two primary methods for producing UF_x , either by passing UF_6 through a microwave discharge or by mixing ablated U atoms with F_2 gas. The former method will be discussed first, while the latter will be discussed in Section 7.3.2.

7.2.1 Formation of UF_x by Passing UF_6 through a Microwave Discharge.

The sample precursor for UF_x was UF_6 (obtained from Oak Ridge Laboratory via United States Enrichment Corporation) added to a 2 L gas collection flask as described in Section 2.3.1. Ar was then added to the flask so that the UF_6 concentration was 0.5%. One of the complications with working with fluorine compounds is that F_2 is so electronegative that it can attack the glass or metal surfaces common in most spectroscopic chambers. Eventually, F_2 will react with the entire surface to form a coating that is resistant to further reaction with more F_2 . This process of forming such a coating is called passivation, and the resistant surface is said to have been passivated. Any surface will remain passivated until it is exposed to water vapor or air. Therefore the flask and Walters vacuum apparatus were passivated with either a F_2/Ar mixture or UF_6 prior to filling the flask with the sample precursor (UF_6) and matrix host (Ar). Once the flask was connected to the MI apparatus, gas from the flask was allowed to flow through the system in order to passivate it. As a check for system passivation and to ensure the equipment was working properly, the LIF spectrum of UF_6 was recorded.

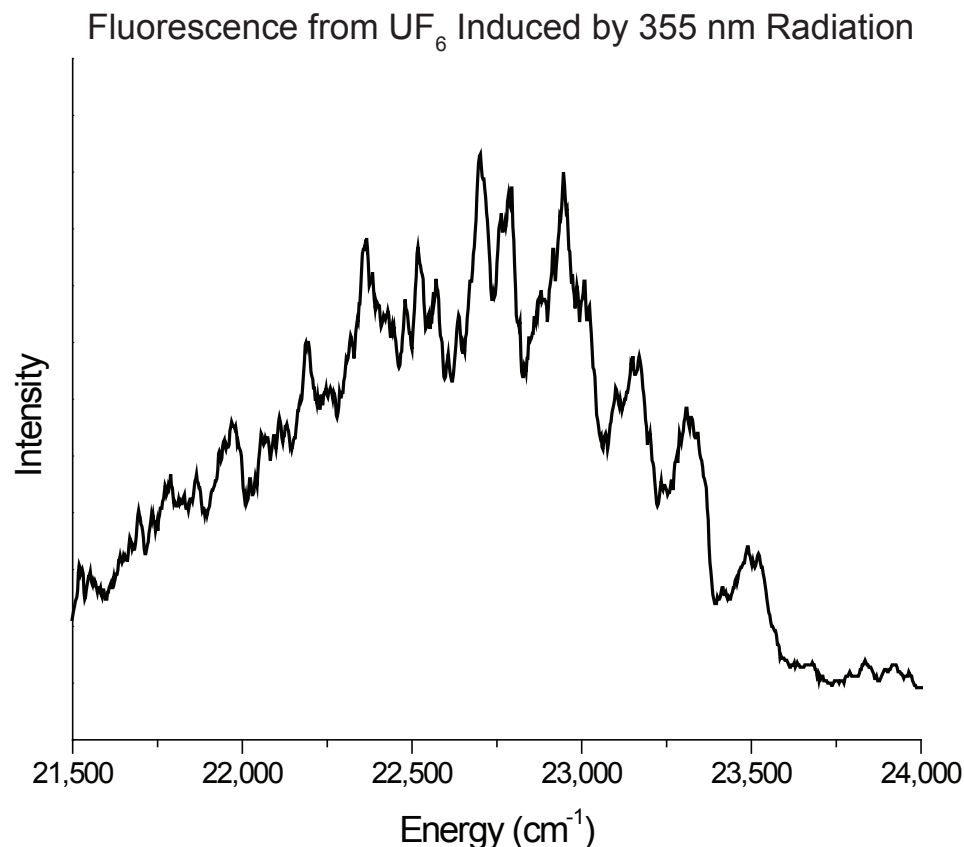


Figure 7.2: Visible fluorescence from UF₆ induced by 355 nm Radiation. The peak assignments, made by a comparison with Grzybowski and Andrews's[1] spectra, are listed in Table 7.1 rather than being labeled on the actual spectrum because of the close proximity of the peaks.

7.2.1.1 Preliminary Spectra of UF₆

To make the matrix, the gas from the sample flask was deposited onto a cold (12 K) Cu mirror at a rate of approximately 3 mmol/h for 3 h. The spectrum of UF₆ was recorded and is shown in Figure 7.2. Because of the close proximity of the spectral features, they are listed in Table 7.1 rather than labeled on the spectrum. The values from Grzybowski and Andrews's[1] spectra are also listed in the table for comparison. The table shows that the data from this experiment were in good agreement with the data reported in the literature, and any discrepancy probably arises from either a poor signal to noise ratio or the resolution of the spectrum recorded here.

Specifically, the notations used in the table are as follows: the various vibrational progressions are labeled with a letter and number, e.g. A(0); A(0) means the first band in the first observed vibrational progression; B(0) means the first band in the second observed vibrational progression; a double value listed for each series indicates a splitting caused by matrix site effects; a dash indicates a broad feature in Figure 7.2 which overlaps the area of a sharp peak identified by Grzybowski and Andrews; a "?" next to the series label indicates uncertainty in the identification; "Not seen" refers to peaks unidentifiable in Figure 7.2, but were present in Grzybowski and Andrews's spectra. After analyzing the various vibrational progressions observed, Grzybowski and Andrews determined that there were three active modes: $\nu_1 = 661 \pm 2 \text{ cm}^{-1}$, $\nu_5 = 198 \pm 2 \text{ cm}^{-1}$, and $\nu_6 = 144 \pm 2 \text{ cm}^{-1}$. From the spectrum in Figure 7.2, one can assume that the system was properly passivated, even though there were some discrepancies in the assignments of the bands. Because the primary goal for the experiments presented here was to study the spectroscopy of UF_x and not UF_6 no effort was spent to resolve the discrepancies. Additionally, the signal to noise ratio was much poorer than in Grzybowski and Andrews's spectra, and there was broad background fluorescence producing a curved baseline, all of which could affect the identification of bands in the spectrum recorded here.

Once the MI system was passivated, the gas mixture (prepared above) was then allowed to pass through a microwave discharge (Section 2.3.1.2) and was deposited onto a cold (12 K) Cu substrate at a rate of approximately 3 mmol/h for approximately 3 h. After deposition, the matrices were excited using light from various pulsed laser sources. IR absorption measurements were not made on these matrices because the IR spectrometer was unavailable.

Series	Peak Values (Andrews) ^a (cm ⁻¹)		Value in Spectrum ^b (cm ⁻¹)	Series	Peak Values (Andrews) ^a (cm ⁻¹)		Value in Spectrum ^b (cm ⁻¹)
A(0)	24,649	24,641	Not seen	C(1)	23,790	23,783	23,798-23,801
A'	24621		24,625	C'	23,764		23,762
A(1)	24,450	24,443	24,435-24453	C(2)	23,592	23,585	23,579
A'	24,423		24,420	C'	23,566		23,568
A(2)	24,253	24,246	24,237-24260	C(3)	23,394	23,387	23,406
A'	24,227		24,225	C'	23,367		23,370
A(3)	24,055	24,049	24,047-24,053	C(4)	23,194	23,188	23,196-23,207
A'	24,030		24,033	D(0)	23,844	23,837	23,832
A(4)	23,857	23,852	23,861	D(1)	23,647	23,640	23,646
A(5)			23657-23669	D'	23,621		
A'	23,630		23,635	D(2)?	23,448	23,441	23,466
B(0)	24,505	24,498	24,494-24,507	D'	23,423		23,427
B(1)	24,307	24,300	Not seen	D(3)	23,248	23,242	23,242-23,248
B(2)	24,109	24,103	24,102-24,108	D'	23,225		23,226
B'	24,084		24,073	D(4)	23,049	23,043	23,052-23,062
B(3)	23,911	23,905	23,901 23,915	D'	23,026		23,015-23,023
B'	23,887		23,875	E(0)	23,326		23,329
B(4)	23,712	23,707	23,708	E(1)	23,129	23,121	
B'	23,688		23,694	E(2)	22,931	22,924	22,931
B(5)	23,511	23,506	23,510	F'	23,157		23,156
B'	23,489		23,499	F(1)	22,985	22,978	
B'	23,291		23,288-23,294	F'	22,960		22,954
B(7)	23,114			F(2)			22,792-22,779
B'	23,092			F(3)	22,588	22,581	22,586
C(0)	23,988	23,981	23,998	G(0)	22,665		22,668
C'	23,962		23,966				

(a)=reference [1] (b)= Figure 7.2

Table 7.1: Peak assignments for UF₆.

7.2.2 Formation of UF_x by Mixing Ablated U with F_2

Matrices containing UF_x also were made by mixing ablated U atoms with an F_2/Ar mixture. The IR spectra from such matrices were recorded earlier by Andrews *et al.*[2], but no visible fluorescence was recorded. The thought was that Andrews *et al.*'s experiment, however, could help in the identification of the various products that could be formed from the sample precursor.

The source for U in these experiments was the same U disk described in Section 4.2. The metal was vaporized with the green light of the Nd:YAG laser (10 Hz / 40 mJ/pulse) using the ablation cell in Figure 2.6 (b). The resultant vapor was mixed with 0.5 % F_2 / Ar mixture and allowed to deposit on the cold Cu mirror at a rate of 3 mmol/h for approximately 3 h. After deposition, the matrices were excited using light from various pulsed laser sources. As mentioned previously, the FTIR spectrometer was not available during these experiments.

7.3 Results

7.3.1 Spectra for UF_x Products Generated by Passing UF_6 through a Microwave Discharge.

7.3.1.1 Fixed Frequency Excitation

Fixed frequency excitation was performed by exciting the matrices with the 355 nm light from the Nd:YAG laser, and the resultant spectrum is shown in Figure 7.3. The spectrum contains a number of fluorescence features, none of which has been assigned to UF_6 . The fluorescence from $23,225\text{ cm}^{-1}$ to $20,014\text{ cm}^{-1}$ is definitely not from UF_6 and is tentatively assigned to some other U and F containing species. Although this feature appears to contain a vibrational progression, it is not resolvable

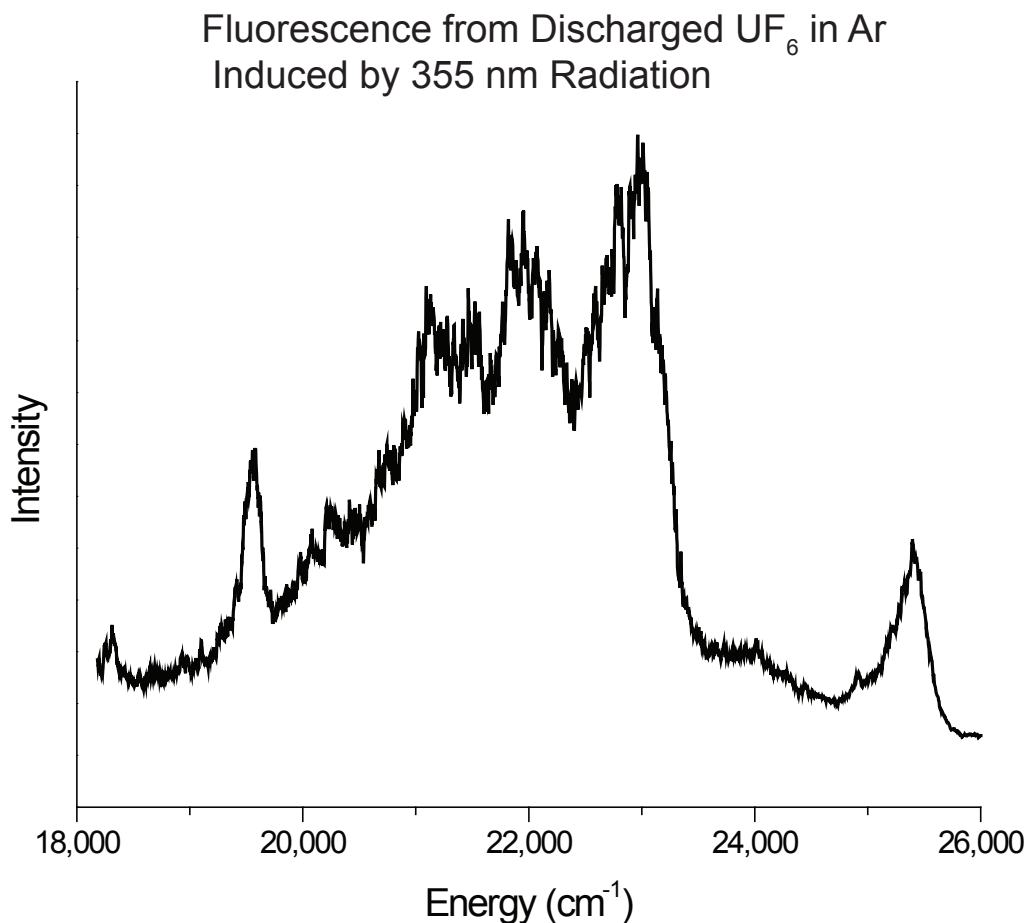


Figure 7.3: Fluorescence from UF₆, passed through a discharge and frozen in Ar, induced by 355 nm radiation. The spectrum was recorded with a 0.20 μ s gate delayed 0.10 μ s with respect to the laser firing.

enough to determine the frequency of the observed mode, especially because the fluorescence may be coming from more than one species. Fluorescence decay lifetimes were measured at different energies in the spectrum and are listed in Table 7.2. All the recorded lifetimes were several hundred microseconds. The error indicated in the table is purely from the least squares fitting routine and does not reflect other systematic errors. Because the signals were weak and the resolution of the scope was only 8 bits, the decay curves had a lot of noise from digitization, which was a much larger source of error in the fits.

Fluorescence Detected (cm^{-1})	Lifetime ($\pm 0.004 \mu\text{s}$)
355 nm excitation	
22,989	0.419
22,090	0.260
21,299	0.428
21,137	0.378
20,325	0.418
19,546	0.489
430 nm excitation	
21,368	0.355
20,408	0.682

Table 7.2: Fluorescence lifetimes for UF_6 , passed through a discharge and frozen in Ar.

7.3.1.2 Tunable Excitation

Tunable laser radiation was used to investigate the energy levels giving rise to the fluorescence bands in Figure 7.3 in order to better resolve them and to determine how many different species or electronic states of the same species were involved. Wavelength selected fluorescence excitation spectra were recorded by scanning the excitation wavelength while monitoring the light emitted by the $21,277 \text{ cm}^{-1}$ emission band (Figure 7.4). The dye tuning curve was also recorded to make sure features in the spectrum were real and not an artifact of laser power. In addition, a spectrum with the same profile, though less intense, was recorded for the $21,368 \text{ cm}^{-1}$ emission band. Another spectrum was recorded for the $20,408 \text{ cm}^{-1}$ emission band (Figure 7.5 (a)). Notice the red edge of the spectrum is very sharp and the blue edge decays with laser power. Lifetime measurements also were made for the fluorescence induced by tunable radiation and are given in Table 7.2. The $20,408 \text{ cm}^{-1}$ fluorescence has a longer lifetime ($0.682 \pm 0.004 \mu\text{s}$) than most of the other fluorescence. The error

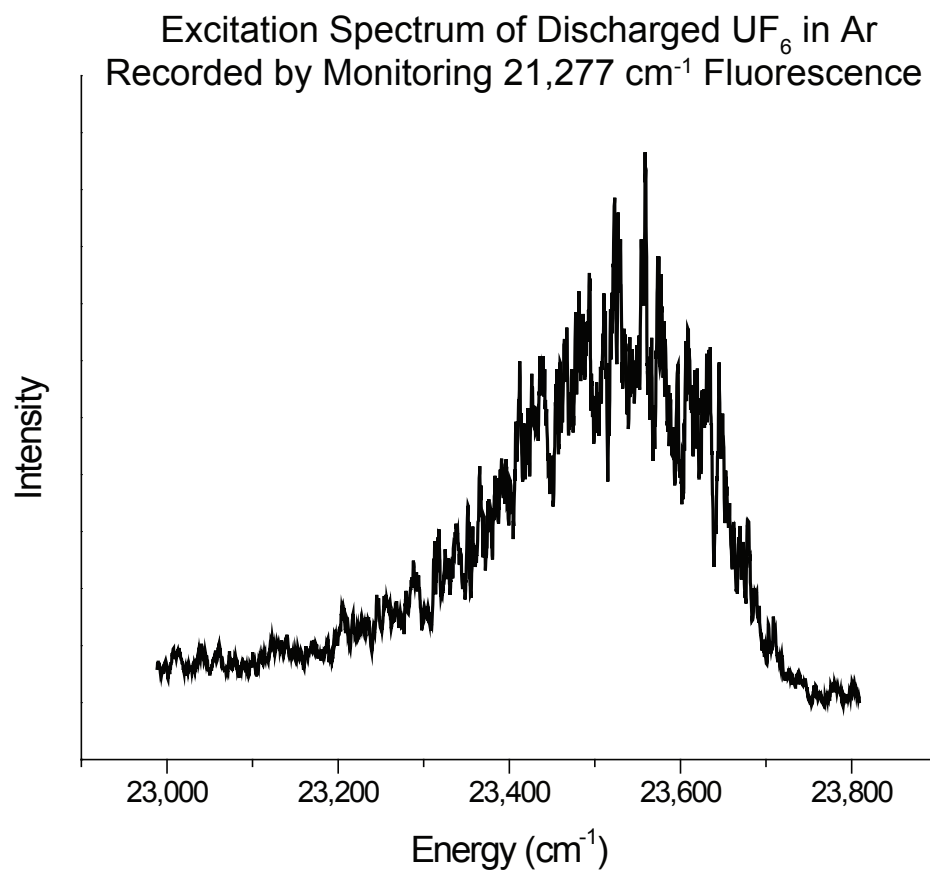


Figure 7.4: Excitation spectra of UF₆, passed through a discharge and frozen in Ar recorded by monitoring 21,277 cm⁻¹ fluorescence. The spectrum was recorded with a 0.20 μs gate delayed 0.10 μs with respect to the laser firing.

Excitation Spectra of UF_x in Ar Recorded by Monitoring
 $20,408 \text{ cm}^{-1}$ Fluorescence

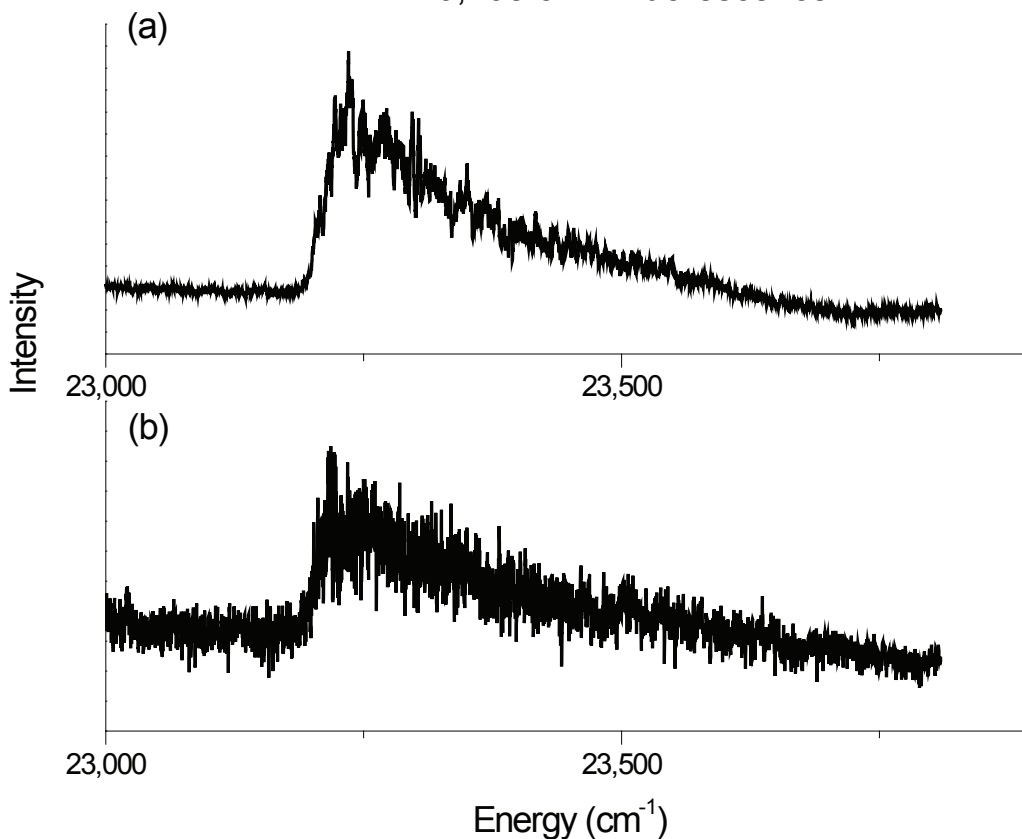


Figure 7.5: Excitation spectra of UF_x in Ar recorded by monitoring $20,408 \text{ cm}^{-1}$ fluorescence. Both spectra were recorded with a $0.20 \mu\text{s}$ gate delayed $0.10 \mu\text{s}$ with respect to the laser firing. (a) Matrix formed by passing UF_6 in Ar through a microwave discharge. (b) The same spectrum recorded from a matrix made from ablated $\text{U} + 0.5\% \text{ F}_2/\text{Ar}$. The bands in (a) and (b) are identical except less of the emitting species is present in (b), which causes a weaker intensity.

indicated in the table is purely from the least squares fitting routine and does not reflect other systematic errors. Because the signals were weak and the resolution of the scope was only 8 bit, the decays curves had a lot of noise from digitization, which was a much larger source of error in the fits.

7.3.2 Spectra from the Formation of UF_x by Mixing Ablated U with F_2

7.3.2.1 Fixed Frequency Excitation

Fixed frequency excitation was performed by exciting the matrices with the 355 nm light from the Nd:YAG laser, and the resultant spectrum is shown in Figure 7.6. The broad band in the middle of the spectrum is from some species containing U and F, but is quite different than the fluorescence observed in the discharge experiments. It is possible that hidden beneath this broad feature are the bands seen in Figure 7.3. The peak at $14,085\text{ cm}^{-1}$ is the second order of the 355 nm excitation laser, and the two peaks on the far left are second order of the two peaks on the right side of the spectrum.

7.3.2.2 Tunable Excitation

Tunable laser radiation was used to investigate the energy levels giving rise to the fluorescence bands in Figure 7.6 in order to determine if the sharper fluorescence bands from the discharge experiments were still present in the ablation experiment. Wavelength selected fluorescence excitation spectra were recorded by scanning the excitation wavelength while monitoring the light emitted by the $21,277\text{ cm}^{-1}$ emission band (Figure 7.4 (b)), as it was the most intense feature in the discharge experi-

Fluorescence from Ablated U + 0.5% F₂ in Ar Induced by 355 nm Radiation

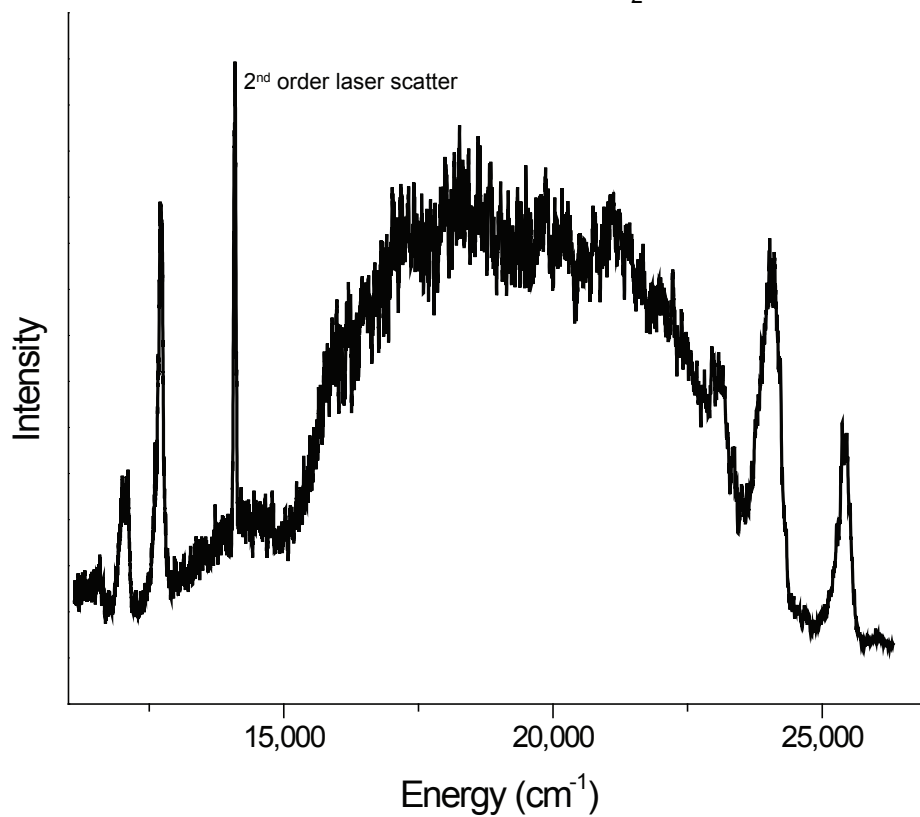


Figure 7.6: Fluorescence from ablated U + 0.5% F₂ in Ar induced by 355 nm radiation. The spectrum was recorded with a 0.20 μ s gate delayed 0.10 μ s with respect to the laser firing. Notice the bands present in Figure 7.3 are not observed.

ments. Though less intense, the shape of the feature is identical to one observed in the discharge experiments. The other features observed in the wavelength selected fluorescence excitation spectra for the discharge experiments were not observed indicating a different matrix composition.

7.4 Analysis and Discussion

Let us first examine the predominant and broad fluorescence shown in Figures 7.3 and 7.6. In many of the other experiments presented here, the matrix composition was determined by comparing an IR spectrum with one recorded by Andrews or another group. In the case of UO_2 , it was a fluorescence spectrum that was compared. Unfortunately, the IR spectrometer was not available at the time of the UF_x experiments, so no direct comparison can be made with Hunt *et al.*'s experiments.[2]. Additionally, the vibrational frequencies of UF_x are too low in energy to be detected by the MCT detector. An indirect comparison, though, can be made. Table 7.3 list the peaks and positions for Andrews's IR spectra of ablated $\text{U} + \text{F}_2$. Not evident from the table is that the primary product trapped in the matrix when the ablation laser was operated at 30 mJ/pulse was UF . Only very small amounts of UF_2 and UF_4 were present immediately after deposition, and virtually no UF_5 or UF_6 was present. When the matrix was annealed to 20 K, the UF_2 peak greatly intensified and peaks for UF_5 and UF_6 appeared. After annealing to 35 K, the UF_5 and UF_6 features dominated.

In the experiments presented here, a comparison of Figures 7.3 and 7.6 with Figure 7.2 showed that UF_6 was not the fluorescing species in the microwave discharge or ablation experiments. A comparison of all the spectra from the microwave discharge and ablation experiments suggested that there were at least two different species fluorescing in the discharge experiments, one of which was not present in the ablation

UF _x in Ar Absorptions	
Assignment	Position (cm ⁻¹)
UF ₆	620
UF ₅	584
F ₃ ⁻	561
UF ₄	537
UF ₄	532
UF ₃	496
UF ₂	446
UF	400

Table 7.3: IR absorptions of U + F₂. [2]

experiments. For the following analysis it is best to define low order and high order UF_x. Low order refers to UF_x compounds where $x=1, 2, \text{ or } 3$. High order refers to UF_x compounds where $x=4, 5, \text{ or } 6$. (The assumption is that the maximum coordination number for U and F is six). Based on Hunt *et al.*'s annealing studies described in the previous paragraph, low orders of UF_x form during deposition and only after annealing are the high orders of UF_x formed. When the microwave discharge was used, the sample precursor was UF₆, a high order UF_x. Therefore, it is possible to initially trap high orders of UF_x in the matrix using the microwave discharge method. A reasonable assignment of the fluorescence is that the fluorescence common to both experiments is from UF₂. Notice that the 20,408 cm⁻¹ fluorescence from the ablation experiments is less intense, indicating it was not the primary product. The species giving rise to fluorescence observed only in the discharge experiment was probably UF₅ because it appeared by eye to be the weakest (other than UF₆) directly following deposition in Hunt *et al.*'s [2] experiments, which makes it possible that UF₅ fluorescence may not be observed in the ablation experiments. However, fluorescence intensity is determined by fluorescence quantum yields, which are often much different

from IR absorption strengths. Consequently, some species with weak IR absorptions may produce strong fluorescence, making it difficult to use an IR spectrum to predict a fluorescence spectrum. At any rate, there was a species not present in the ablation experiments that was present in the discharge experiments, and UF_5 was the most logical assignment.

Without the determination of the species trapped in the matrix, it is almost impossible to assign the peaks in Figure 7.3 to a vibrational progression. Unfortunately, the excitation and emission bands are so closely spaced together that this congested spectrum cannot be better resolved. Probably the best way to unravel these spectra would be to record the gas phase fluorescence spectra, in which the scattered light problem will not be as severe and rotational data could help identify the trapped species. Additionally, the REMPI mass spectrum should confirm what species should have been trapped in the matrices. Also, it is worth revisiting the calculations discussed in the introduction. To date the only quantitative predictions for the electronic levels of uranium fluorides were for UF .^[92] It is quite apparent that the fluorescence observed here involves energy levels lying well above those levels calculated by Federov *et al.*^[92] As a result, those calculations are of little help in interpreting the spectra presented here. However, they do suggest that better resolvable fluorescence may be found in the IR region of the spectrum, which unfortunately the MI experiment setup here cannot detect. Alternatively, the energy of the observed fluorescence fits better with the ligand to metal charge transfer transitions observed for other actinide containing molecules discussed previously.

Lastly, there are some relatively sharp bands in Figures 7.2 and 7.6 that have yet to be discussed. The peak at $24,455 \text{ cm}^{-1}$ in Figure 7.2 is always present in a matrix containing U, but has yet to be assigned. An U atomic line is a good first guess for this peak because it appears regardless of other sample precursors in gas mixture used during deposition. However, there are two selection rules governing

atomic transitions. One rule is that there must be a change in symmetry, that is, only $g \leftarrow u$ and $u \leftarrow g$ transitions are allowed. The other rule is that all $\Delta J=0, +1,$ or -1 transitions are allowed, where J is the total electronic angular momentum as described in Section 3.2. Because there is only one peak in the spectrum instead of three closely spaced peaks, it is very unlikely that this transition is from atomic U. In Figure 7.6 the peak at $24,455 \text{ cm}^{-1}$ is the same peak seen in Figure 7.2 discussed above. The peak at $25,536 \text{ cm}^{-1}$ also has not been assigned thus far and is not likely to be an atomic line based on selection rules. The two peaks to the left of the laser scatter are second order of the $24,455 \text{ cm}^{-1}$ and $25,536 \text{ cm}^{-1}$ peaks.

7.5 Conclusion

Fluorescence spectra for UF_x ($x < 6$) in Ar were successfully recorded. However, from the methods used to produce the UF_x , x in the fluorescing species was unclear because a number of different UF_x compounds were probably produced. Therefore without knowing the species giving rise to the fluorescence, it was hard to further interpret the fluorescence bands. Also, it is much harder in MI spectroscopy to identify the carrier of the fluorescence than in gas phase spectroscopy because for compounds containing heavy metals, no rotational structure is present. As a result, it was proposed either to use gas-phase LIF or REMPI to determine the fluorescing species from a number of possible candidates that could be trapped in the matrix. This proposal was based on the belief at the time that the data collected here could guide future gas phase experiments by providing a low resolution spectral map. Coincidentally, researchers began to realize the large perturbations on actinide compounds caused by the rare gas, especially Ar as discussed in Chapter 4. The perturbations for Ne are far less. (Knowing the latter, it would be desirable to use Ne as the host gas for all the experiments presented here, but the MI refrigerator used in this setup cannot freeze

Ne). With the uncertainty in matrix effects, one could not be certain of the blue shift in the gas-phase bands relative to the matrix bands, which could make the gas-phase experiments more challenging. The uranium fluoride experiments, however, solidified the need to obtain an IR spectrometer so that LIF and IR spectra recorded for the same matrix could be correlated, thus making the interpretation of the LIF spectra easier. Now that the IR spectrometer is present, IR spectra can help identify the composition of the matrices in the above experiments.

Chapter 8

The Search for the Electronic Spectra of Uranium Nitrides

8.1 Introduction

In order to obtain the most conclusive results from the fluorescence MI spectroscopy, it was pertinent to know what species were trapped in the matrix. From the IR spectra recorded during the MI spectroscopy of uranium oxides (Chapter 6), there was enough background N₂ impurities to always form UN₂ when U metal was ablated (see Figure 8.1). However, no fluorescence in the previous experiments was ever attributed to UN₂. The only previous spectroscopy studies of uranium nitrides were a study by Green and Reedy[94] and several studies by Andrews and colleagues[95, 96, 97], both using IR spectroscopy.

The geometry of UN₂ is predicted to be linear ($D_{\infty h}$) with a UN bond length of 1.726 Å (see Figure 8.2).[96] UN₂ is isoelectric with the UO₂²⁺ discussed in Chapter 5. The electronic configuration for the ground state is $^1\Sigma_g^+(5f^2)$, which is the same for the uranyl ion.[98] The configuration was determined by comparing predicted vibrational frequencies with the experimentally measured frequencies. Because experimental data

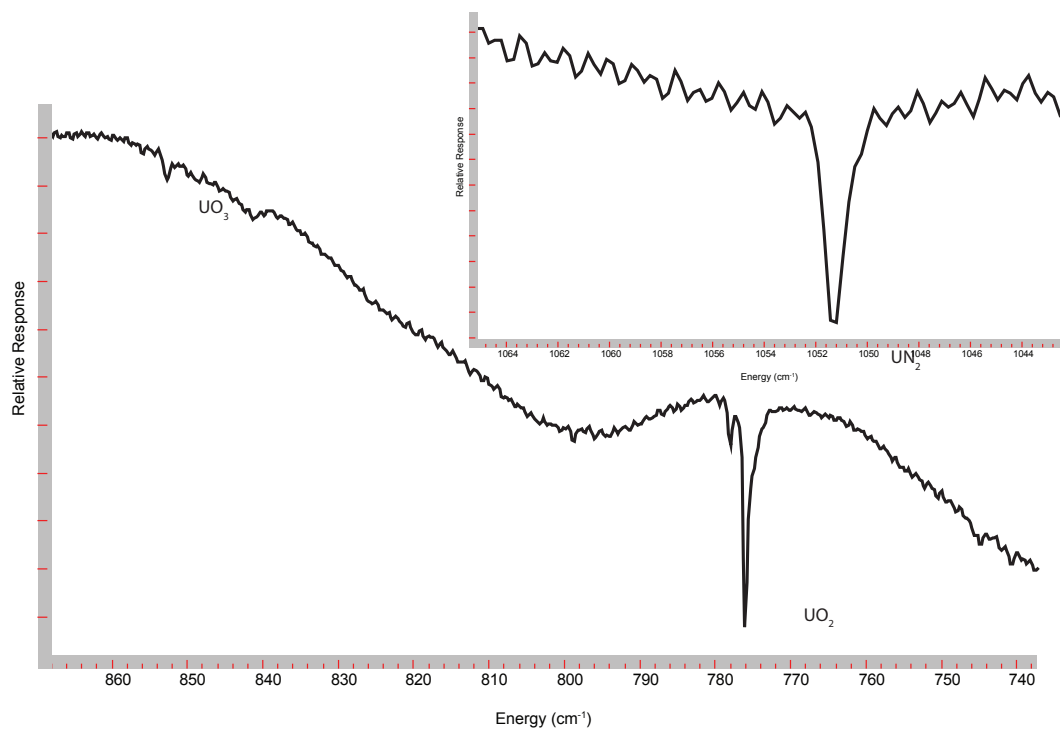


Figure 8.1: IR absorptions of ablated U + 1% O₂ in Ar. In every IR spectrum recorded for the experiments in Chapter 6, the absorption for UN₂ was present.

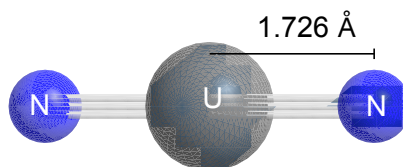


Figure 8.2: The geometry of UN₂. [96]

on the electronic structure of UN_2 is lacking, there is also a lack of explicit theoretical predictions for excited states of the molecule. Based on the similarity with uranyl ion, a search for UN_x fluorescence was logical because its presence in a matrix could be confirmed via IR spectroscopy and no such spectra had been reported previously. It was also logical to expect fluorescence in the green, yellow, and orange region of the visible spectrum, which could easily be detected with the experiment setup here. Additionally, one would expect strong absorption bands in the blue spectral region.

8.2 Experiment Details

The source of U atoms was a U rod (Oak Ridge National Laboratory). A piece of steel was epoxied to the end of the rod so that it could be moved with a magnet as described in Section 2.3.2.1. Green light from the Nd:YAG laser (40 mJ/pulse; 5 Hz) was used to ablate the metal. The laser spot on the surface was manually moved by adjusting the focusing lens. During the ablation, a mixture of N_2/Ar was flown over the metal at a rate of 3 mmol/h and the resultant mixture was allowed to deposit on the cold CsI substrate. For most of the following spectra, unless otherwise noted, the N_2 concentration in the host gas was 1%. Immediately after deposition, prior to any fluorescence measurements, an IR spectrum was recorded. Then, the matrices were excited by various pulsed laser sources and the resulted fluorescence was recorded.

8.2.1 IR Absorption

Figure 8.3 shows two IR spectra recorded for $\text{U} + \text{N}_2$. The black trace was recorded immediately following deposition and the purple trace was recorded after fixed frequency excitation, which could induce photolysis. Both 355 and 266 nm irradiation produced the same results. The peaks in the spectra are labeled according to the

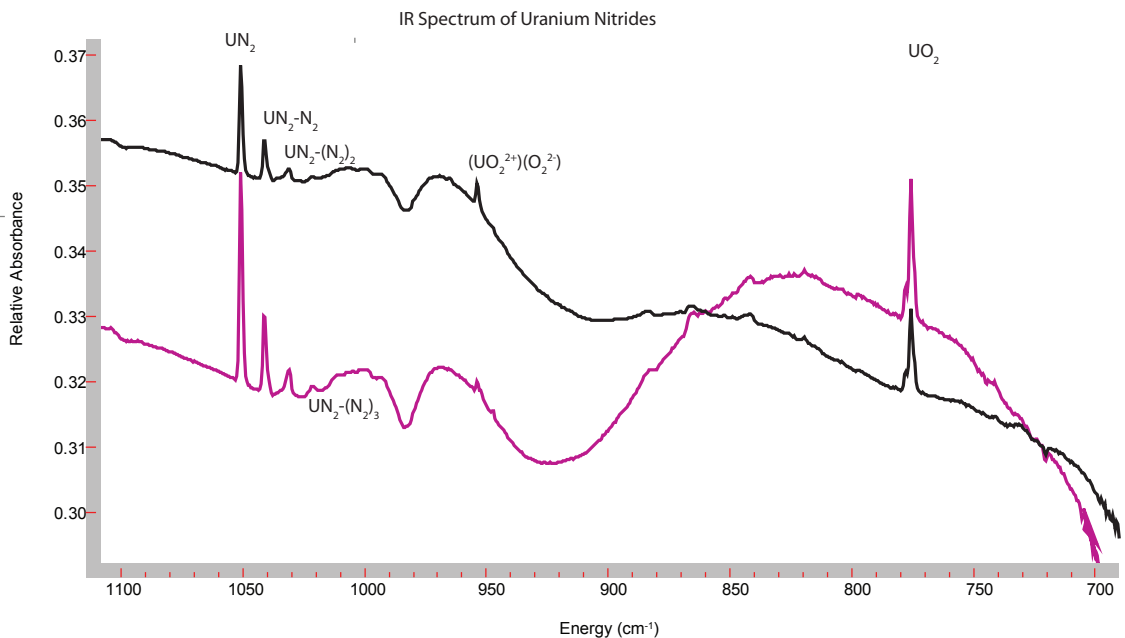


Figure 8.3: IR absorption spectra for U + 1% N₂ in Ar. The black trace was recorded immediately following deposition. The purple trace was recorded following 355 nm photolysis, though 266 nm photolysis produced an identical spectrum. Note that for ease in interpreting the spectrum, the absolute absorbance for the purple trace has been shifted. Peaks are labeled according to Hunt *et al.*'s spectra.[95]

spectra recorded by Hunt *et al.*[95] An important method to using the IR spectra to determine the species producing the fluorescence described in the next two sections is to compare the intensity changes after photolysis. With the exception of (UO₂)²⁺(O₂)²⁻, all the absorptions labeled in the spectrum increase after photolysis. As time elapses after deposition, the total IR radiation that reaches the detector decreases, making it a safe assumption that all observed increases in IR absorptions are real and not an artifact of alignment. This decrease is most likely caused by the degradation of the optical quality of the matrix due such effects as surface cracking. Also, the only optics that are adjusted between the recording of the IR spectrum and photolysis is the position of the CsI substrate. Table 8.1 summarizes the changes in the IR spectra shown in Figure 8.3 induced by photolysis. Another item worth noting here is the lack of the UN absorption in the spectrum, which occurs at 1,000.9

IR Absorptions		
Peak (cm ⁻¹)	Assignment	Increase After Photolysis?
1,050	UN ₂	yes
1,041	UN ₂ -N ₂	yes
1,031	UN ₂ -(N ₂) ₂	yes
1,021	UN ₂ -(N ₂) ₃	yes
954	(UO ₂ ²⁺)(O ₂ ²⁻)	no
776	UO ₂	yes

Table 8.1: Summary of the IR absorptions for U + 1% N₂ in Ar.

cm⁻¹. There are two possible reactions involving U + N₂:



Equation 8.1 is often referred to as an extraction mechanism, while Equation 8.2 is known as an insertion mechanism. According to Hunt *et al.*[95], the bond energy, D, of N₂ is 225 kcal/mol, whereas D(UN) is 126±5 kcal/mol. Consequently, Equation 8.1 is not energetically favorable. However, D(O₂) is 118 kcal/mol, whereas D(UO) is 179±7 kcal/mol. Thus, the reaction for U + O₂ analogous to Equation 8.1 is energetically favorable, and in the study of uranium oxides, UO was formed from the ablation of U metal in an O₂/Ar mixture. The IR absorption for UN has been observed in prior experiments[94, 96, 97], but these experiments used NO (D=150 kcal/mol)[99] or NO₂ (D=117 kcal/mol)[100].

8.2.2 Fixed Frequency Excitation

Excitation of the matrix with 355 and 266 nm radiation produced several long and short lived emission features as shown in Figure 8.4 (a) and (b) and Figure 8.5. The short-lived fluorescence induced by 266 nm radiation was not recorded because the CsI substrate interfered with such a spectrum.

8.2.2.1 Tunable Excitation

Tunable laser excitation was used to investigate the excited levels that gave rise to the emission bands shown in Figure 8.4. Wavelength selected fluorescence excitation spectra were recorded by scanning the excitation wavelength while monitoring the light emitted by the $15,924\text{ cm}^{-1}$ emission band, as indicated by the arrow in Figure 8.4 (a). Figure 8.6 shows the several spectra spanning the blue-green region of the visible spectrum. Each segment of the Figure 8.6 was fluorescence induced by a different laser dye. What is peculiar is that the middle segment has the best signal to noise ratio, but the lowest peak intensity. Additionally, all three segments were recorded using the same PMT biased by the same high voltage. Data also were recorded using the oscilloscope and PC as described in Section 2.4, which described how a comparison of absolute intensities in different spectra was meaningful. Therefore, some change in experimental conditions such as the alignment of the laser spot on the matrix must have changed over the course of the three scans that produced Figure 8.6. After the excitation spectra were recorded, the radiation of wavelength ($21,673\text{ cm}^{-1}$) producing the strongest fluorescence (indicated by the pink arrow in Figure 8.6) was used to excite the matrix. The resulting spectrum is shown in Figure 8.7. The same spectrum could be obtained by exciting the matrix with radiation corresponding to any of the peaks in Figure 8.6. Unfortunately the spectrum is no better resolved than those obtained with the fixed frequency UV excitation. Table

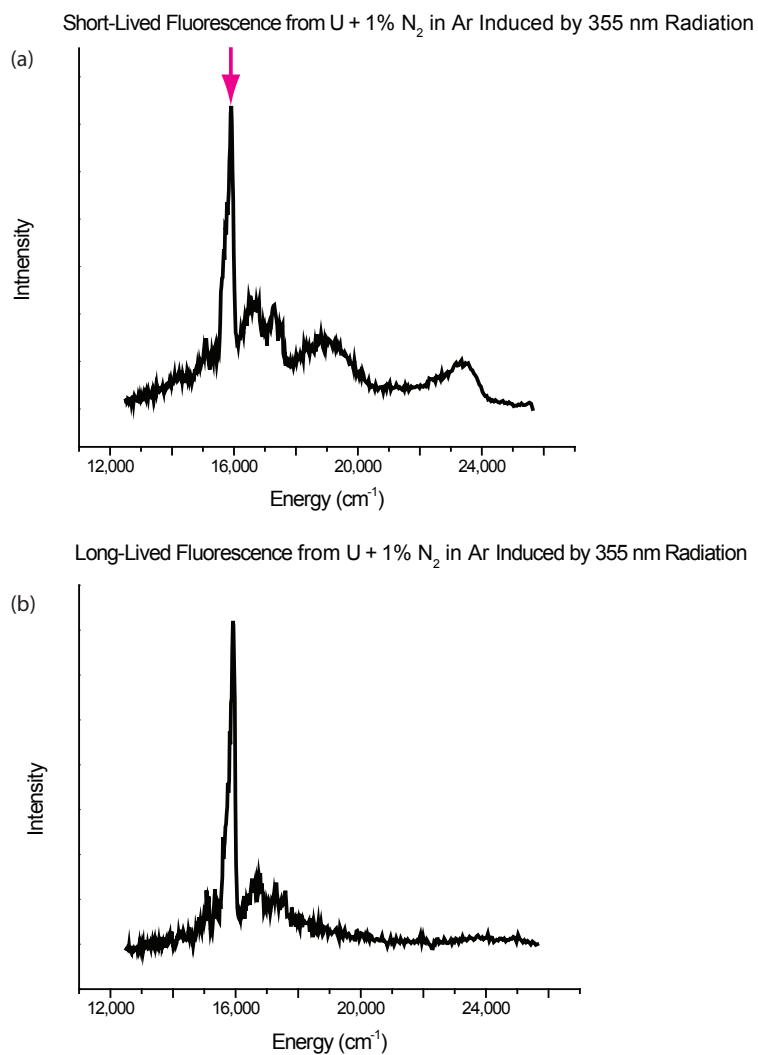


Figure 8.4: Fluorescence from U + 1% N₂ in Ar induced by 355 nm radiation. (a) The spectrum was recorded with 0.20 μ s delay and 0.30 μ s gate width with respect to the laser firing. (b) The spectrum was recorded with 15 μ s delay and 20 μ s gate width with respect to the laser firing.

Long-Lived Fluorescence from U + 1% N₂ in Ar Induced by 266 nm Radiation

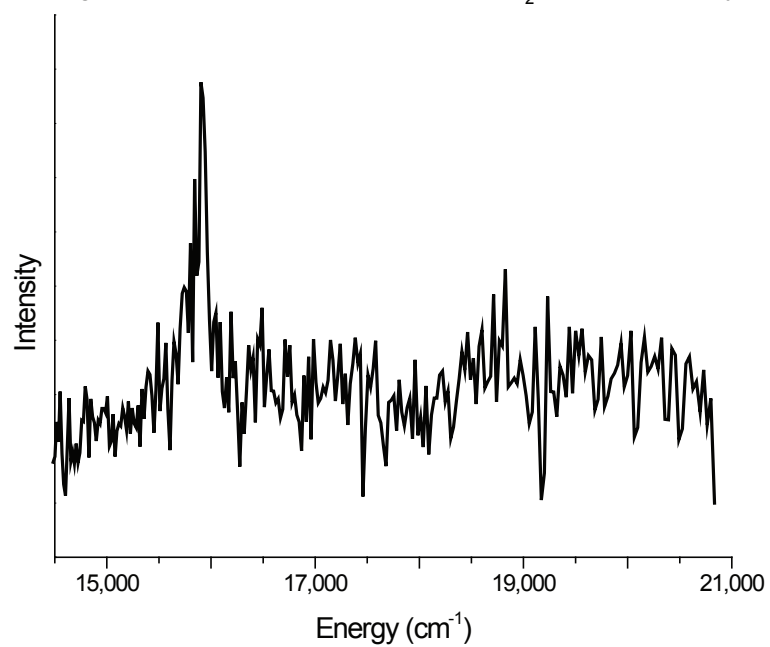


Figure 8.5: Fluorescence from U + 1% N₂ in Ar induced by 266 nm radiation. The spectrum was recorded with 15 μ s delay and 20 μ s gate width with respect to the laser firing.

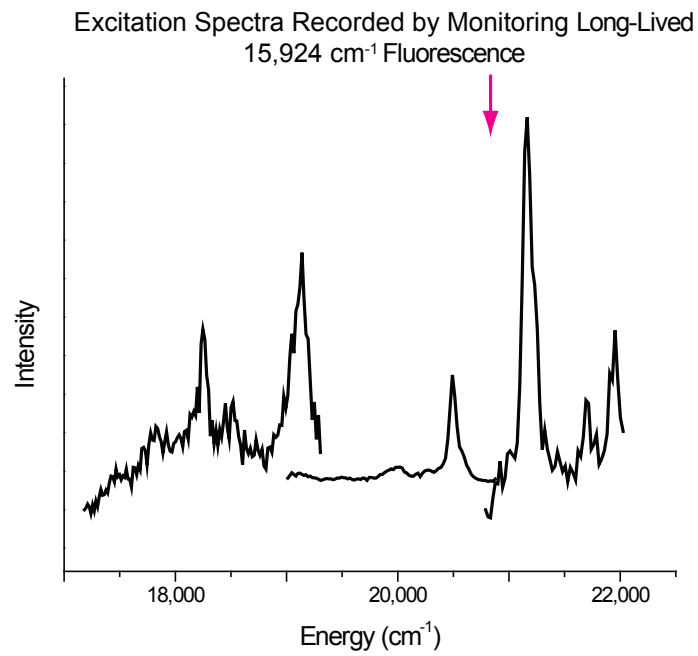


Figure 8.6: Excitation spectra of U + 1% N₂ in Ar recorded by monitoring 15,924 cm^{-1} fluorescence. The spectrum looks disjointed because several spectra were pasted together to form the spectrum. Consequently, peak intensities cannot be compared. The pink arrow indicates the excitation wavelength in Figure 8.7.

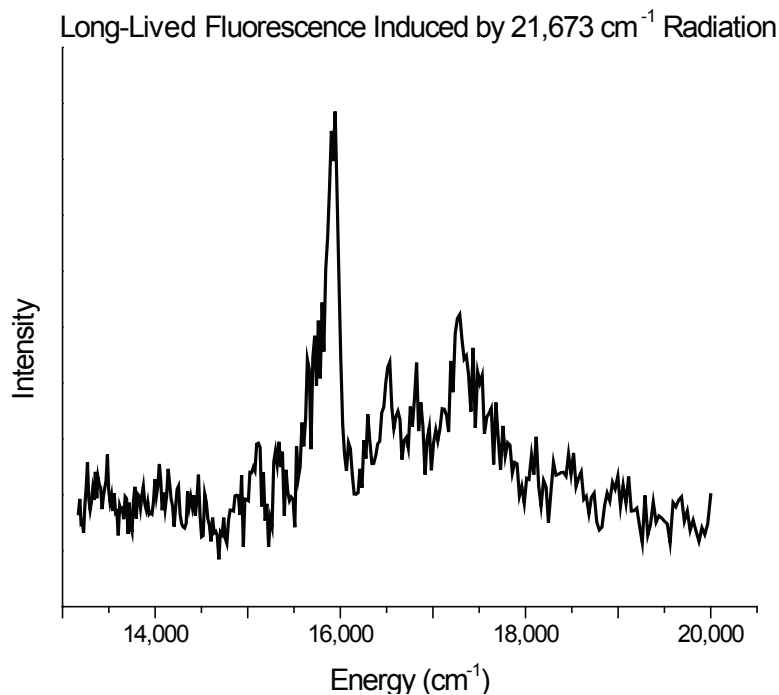


Figure 8.7: Fluorescence from U + 1% N₂ induced by 21,673 cm⁻¹ radiation. The shape of the fluorescence bands are identical (though weaker) to the fluorescence observed in Figure 8.4 (b).

8.2 summarizes the change in visible fluorescence after UV photolysis. As mentioned in the previous chapters, the experiment setup used here made any observation of absolute fluorescence intensity tentative.

Fluorescence decay curves were recorded for all of the emission bands in Figure 8.4 (b) and all the excitation bands in Figure 8.6. By fitting the decay curves to a biexponential function, it was determined that there must be two species or electronic states involved in producing the fluorescence. The decay curve for 15,924 cm⁻¹ fluorescence induced by 21,739 cm⁻¹ radiation is shown in Figure 8.8. There is long-lived ($\sim 51.6 \pm 0.5 \mu\text{s}$) fluorescence and even longer lived fluorescence ($\sim 167.7 \pm 0.7 \mu\text{s}$). Because the fluorescence decay curves for the other bands are nearly identical they are not shown here.

Excitation		Emission	
Peak (cm ⁻¹)	Increase After Photolysis?	Peak (cm ⁻¹)	Increase After Photolysis?
18,188	no	15,159	no
18,346	no	15,425	no
19,040	no	16,036	no
19,919	no	16,680	no
20,445	no	16,894	no
21,107	no	17,342	no
21,653	no	17,624	no
21,895	no		

Table 8.2: Summary of U + 1% N₂ in Ar Fluorescence.

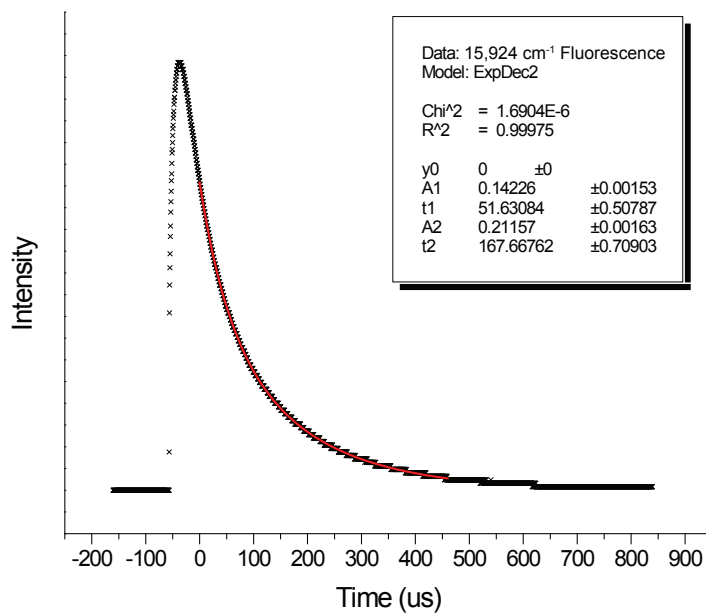


Figure 8.8: 15,924 cm⁻¹ fluorescence induced by 21,739 cm⁻¹ radiation. The fluorescence is biexponential with 51.6 ± 0.5 and 167.7 ± 0.7 μ s being the values of τ_1 and τ_2 respectively.

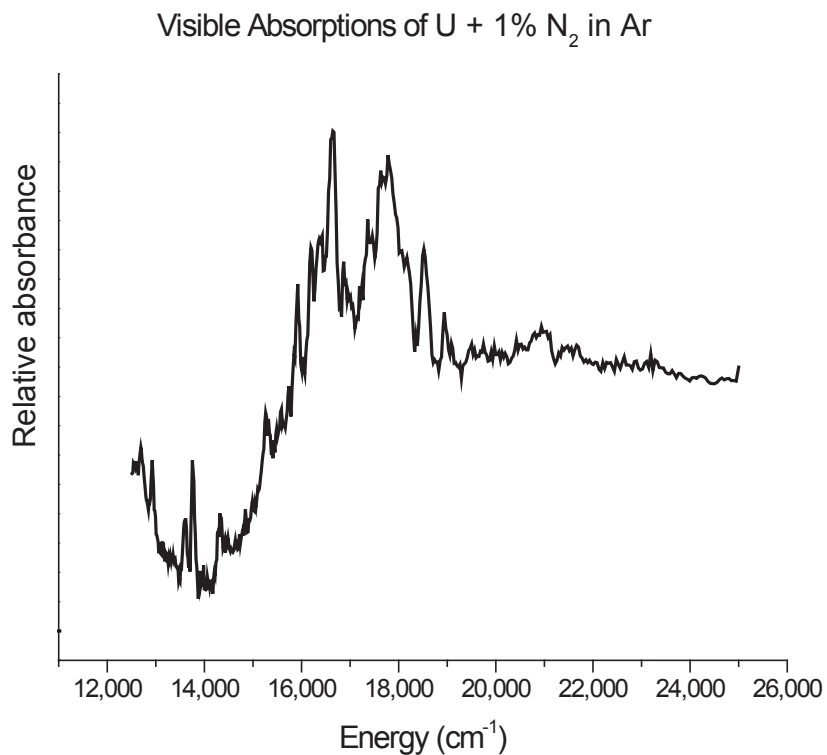


Figure 8.9: Visible absorptions of U + 1% N₂ in Ar.

8.2.3 Visible Absorption

Visible absorption spectra were recorded in hopes of locating some absorption bands which would yield better resolved fluorescence when directly excited. With the substrate being CsI it was very simple to take an absorption spectrum using a tungsten lamp and the same 0.65 m monochromator used for the fluorescence spectra. Figure 8.9 shows the visible absorption spectrum for U + 1% N₂ in Ar. It is important to note that a background scan was recorded and subtracted to obtain this figure. Absorptions found in this spectrum that were not observed in Figure 8.6 were investigated using tunable laser excitation, but no resolvable fluorescence was observed.

8.3 Determining the Fluorescing Species

In other experiments presented here the species giving rise to the fluorescence could be determined in a variety of ways. For UO_2 the Ar matrix spectrum was matched with previous gas phase spectra and theoretical predictions. In other experiments, the IR spectra were compared with those recorded by Andrews to determine the matrix composition. Then, by correlating the visible vibrational progression frequencies with the IR absorption frequencies, the fluorescing species was determined. In this case, it was much more difficult to determine the fluorescing species because of the behavior of the matrix upon photolysis. The visible spectroscopy of $(\text{UO}_2)^{2+}(\text{O}_2)^{2-}$ and UO_2 was discussed in Chapters 4 and 6, and those molecules clearly were not the carrier of the fluorescence. Table 8.1 indicates the identified IR absorptions that increase after photolysis, which includes all the observed absorptions except $(\text{UO}_2)^{2+}(\text{O}_2)^{2-}$. However, no such behavior is observed for the visible fluorescence, which is unchanged after photolysis (Table 8.2). These results would lead one to believe that the uranium nitride or oxide is not the species giving rise to the fluorescence. However, no laser power measurements were made, and that fact combined with the instability of the laser power, made it very uncertain if there really was no change in fluorescence intensity. Alteration of the sample precursor would be necessary to eliminate possible candidates that were fluorescing. A series of experiments were performed to determine the fluorescing species.

In the first of these experiments, the assumption was that N_2 was necessary to produce the fluorescing species because the fluorescence band in Figure 8.4 was not observed in previous U experiments. Based on the IR spectrum, the uranium nitrides present in the matrix after deposition are UN_2 and $\text{UN}_2(\text{N}_2)_x$. The latter of these species should only form in the presence of excess N_2 . Therefore, reducing the concentration of N_2 in the carrier gas should favor the formation of UN_2 . Figure 8.10 shows IR spectrum recorded when the N_2 concentration in the carrier gas was reduced

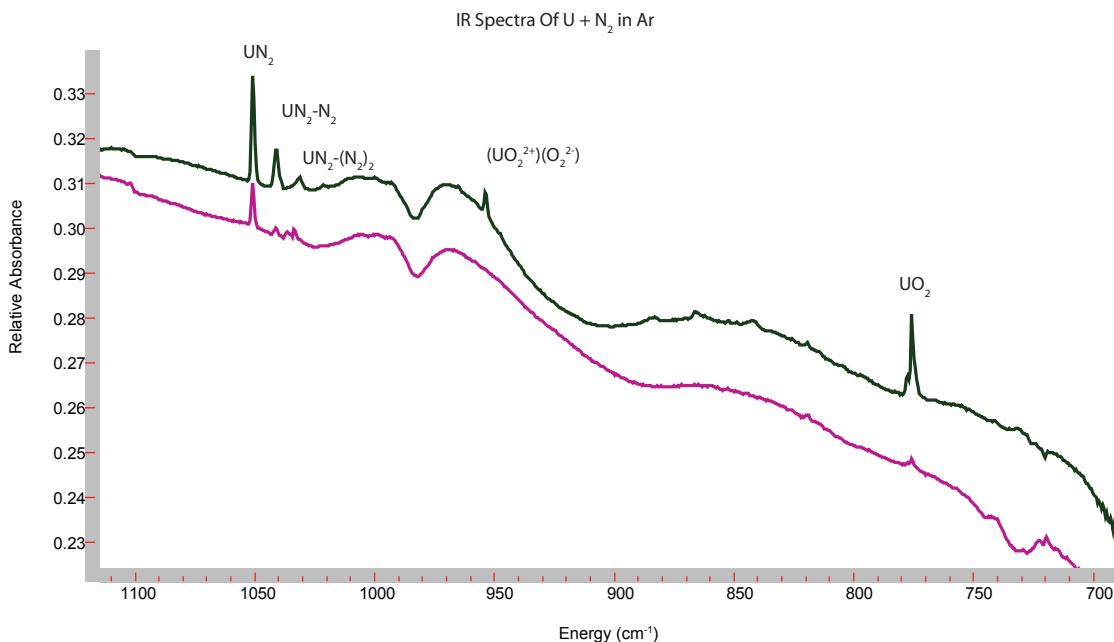


Figure 8.10: IR spectra for U + N₂ in Ar. The pink trace is for U + 0.5% N₂ in Ar and the black trace is for U + 1% N₂ in Ar shown for comparison. Note that the absolute absorbance for both traces has been shifted for ease of viewing the two traces.

from 1 to 0.5%. In this spectrum the intensity of the UN₂(N₂)_x bands decreased with respect to the UN₂. As a result, if UN₂(N₂)_x produced the fluorescence, then the fluorescence band intensity should be weaker relative to those in Figure 8.4. Because the visible fluorescence was identical to the fluorescence recorded for the 1% N₂ matrices, it will not be shown here. However, the fluorescence intensities suggested that UN₂(N₂)_x was not the fluorescing species.

After eliminating UN₂(N₂)_x as candidate for the fluorescing species, the only other nitride possibility was UN₂. The second experiment was designed to verify the presence of N in the fluorescing molecule. For this experiment, 0.5% D₂ replaced the N₂ in the previous experiments. The D₂ was used as a reducing agent to prevent the formation of nitrides and oxides. The IR spectrum for this experiment is shown in Figure 8.11. Notice that all the features related to uranium nitrides are gone with the exception of a hint of UN₂. The peak in the pink trace near the position of UN₂(N₂)₂

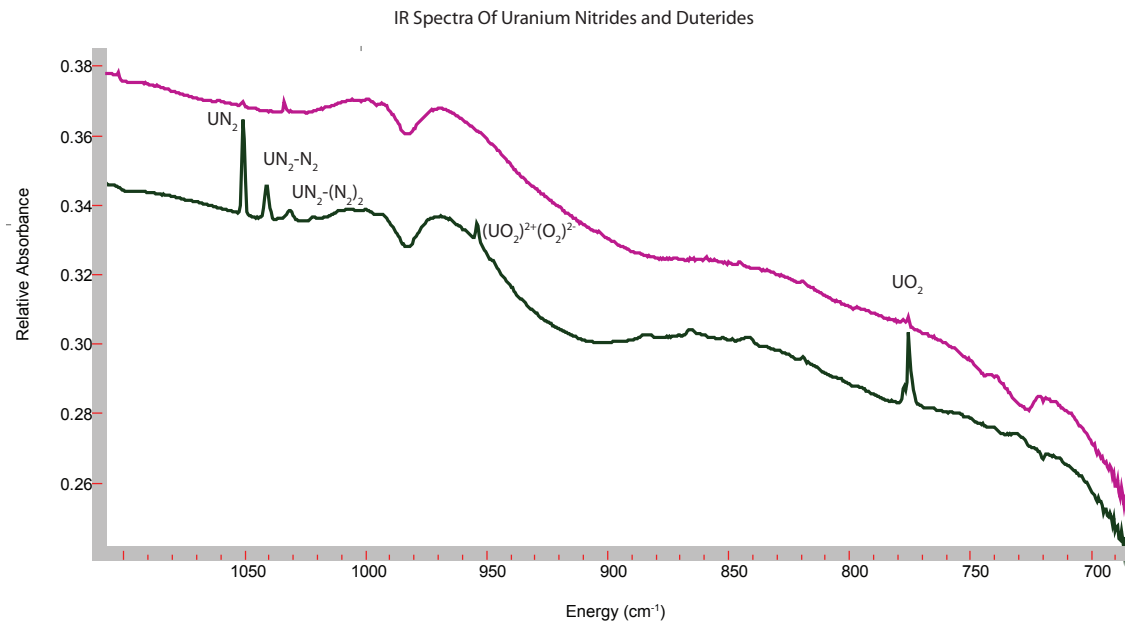


Figure 8.11: IR spectrum for U + D₂ in Ar. The pink trace is for U + 0.5% D₂ in Ar. The black trace is the same U + 1% N₂ in Ar spectrum which has been used before for comparison.

is actually some impurity slightly to the blue of the real peak. Fluorescence experiments (not shown) confirmed that the fluorescence observed in Figure 8.4 was still present.

The last experiment in this series was used to verify that U was necessary to produce the fluorescing species. Instead of ablating U, Cu was ablated in 0.5% D₂/Ar mixture. Figure 8.12 shows a dispersed fluorescence spectrum induced by fixed frequency UV radiation. The Cu dimer spectrum (see Section 2.3.2.1) is evident in the spectrum as well as CuO, but the fluorescence from Figure 8.4 is absent. The bands appearing to the red of the laser scatter line are second order fluorescence.

Short-Lived Fluorescence from Cu + D₂ Induced by 355 nm Radiation

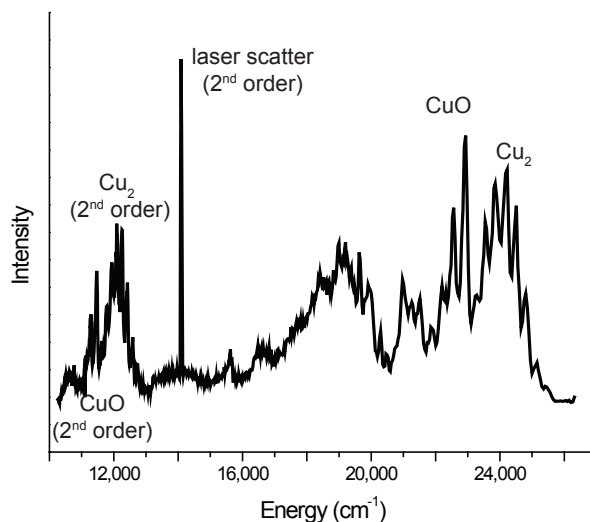


Figure 8.12: Fluorescence from Cu + 0.5% D₂ in Ar induced by 355 nm radiation. The tall spike in the spectrum is second order laser scatter.

8.4 Analysis and Discussion

After three separate experiments to determine the fluorescing species, it was probable that the fluorescing species consisted of only U atoms. Granted, Ar was present as the host in all the matrices, but from what is known so far, Ar should only cause perturbations in the spectra with only some shifting of the band positions. In other words, if the Ar was replaced with Ne in all of the prior experiments in this chapter, the spectrum should look almost identical to the ones shown. The first logical assignment of the fluorescence spectra would be to U atomic lines. Because of the vast number of electronic states of actinides, it is actually very easy to match many of the fluorescence bands shown in the prior figures with atomic U lines. Atomic transitions, though, must obey selection rules. One rule is that there must be a change in symmetry, that is, only $g \leftarrow u$ or $u \leftarrow g$ transitions are allowed. Another rule is that all $\Delta J=0$, $+1$, or -1 transitions are allowed, where J is the total electronic angular momentum as described in Section 3.2. The problem with assigning the observed features to

atomic lines is that for each atomic transition there should be a series of three closely spaced lines corresponding to each of the allowed values of ΔJ . As a consequence of the selection rules governing atomic transitions, the observed fluorescence cannot be coming from atomic U.

If atomic U is discredited as the fluorescing species, then the next most probable candidate is U atom clusters. The setup for the ablation is the configuration shown in Figure 2.6 (c). Unlike the UO_2 experiment which used the ablation setup in Figure 2.6 (b), the metal target was ablated much closer to the substrate, and ablation occurred with comparable laser power. Therefore, it is conceivable that more U would make it to the substrate as compared with the UO_2 experiments, which could lead to the formation of U clusters instead of U atom monomers. While no further experiments have been performed to verify the fluorescence is from clusters or the cluster size, the idea of forming U clusters is very exciting. In the past decade Gagliardi and collaborators have published papers on the nature of the diuranium bond in both neutral and charged species.[101, 102] To date there is no experimental data on such species, and it is not known if they actually can be formed experimentally. Hopefully, further experiments, such as decreasing the U atom concentration by means of lowering the ablation laser power, will shed light on the cluster size. Another question worth asking is how much of a role the Ar plays in stabilizing the clusters? In other words, could U_x exist in the gas phase? U_2^+ has been observed in the mass spectrometer by the Heaven group, but the parent molecule could not be determined.

While the observed fluorescence is not from UN_2 , a question arises as to why UN_2 fluorescence was not observed because it is evident from the IR spectra that the molecule was produced during the ablation process. One explanation for this observation is that the lowest allowed electronic absorption may be too high in energy to be reached by 355 or 308 nm radiation. Consequently, 266 nm radiation may be needed. If the resultant fluorescence transition has a lifetime on the order of magni-

tude of $0.1 \mu\text{s}$, it would be nearly impossible to see if the matrix was deposited on the CsI substrate because of interfering fluorescence from CsI. This explanation could be confirmed using the Cu substrate instead of the CsI. Based on the similarity between UN_2 and UO_2^{2+} , one would expect to observe the symmetric stretch in the fluorescence spectra, which was predicted at 1008.3 cm^{-1} [95] and 1070.1 cm^{-1} [96] in Ar and in the gas phase respectively and could be used to identify the fluorescence. Another explanation for the lack of fluorescence is that the electronically excited molecule relaxes through non-radiative decay to very low-lying excited states. Fluorescence then can occur between these states and the ground state. Because these excited states are so close to the ground state, the fluorescence will be in the IR region of the spectrum. Though no attempt was made to look in the IR region of the spectrum for fluorescence, such fluorescence is unlikely given that UN_2 is isoelectric with UO_2^{2+} . As discussed in Chapter 5, the lowest electronically excited level for UO_2^{2+} lies roughly $19,100 \text{ cm}^{-1}$ above the ground state.[77] It would be difficult to rationalize how there would be very low-lying electronic states.

8.5 Conclusion

The search for UN_2 fluorescence from ablated $\text{U} + \text{N}_2$ in Ar did not produce any fluorescence spectra that could be attributed to UN_2 . However, fluorescence spectra were recorded for matrices containing ablated $\text{U} + \text{N}_2$ in Ar. While no definite carrier of the fluorescence has been determined, various matrices were made from different sample precursors in order to rule out possible candidates. From these experiments, it was determined that neither N nor O was necessary to produce the fluorescing molecule. It was also determined that U atoms were necessary to produce the molecule because the fluorescence did not appear in matrices where Cu replaced U as a sample precursor. Consequently, the most probable candidate for producing the fluorescence

is U atom clusters, though the exact composition of the clusters is undetermined. Given the fact that UN_2 is isoelectric with UO_2^{2+} , it is still unclear why there is no resolvable fluorescence that can be assigned to UN_2 . Further experiments and theoretical investigations are necessary to fully understand the electronic structure of UN_2 and the species that produced the fluorescence in the experiments described in this chapter.

Part II

Electronic and Infrared Spectroscopy of OH-Xe Isolated in Solid Ar

Chapter 9

OH-Xe

9.1 Introduction

The spectroscopy of an open shell molecule, HX, such as OH/D complexed with a closed shell species such as a rare gas atom (Rg) can provide much insight into weak and long range intermolecular interactions such as van der Waals forces. Such forces play a role in reaction dynamics. In the Rg-HX model system, the strength of the interaction can be varied by changing the rare gas. Table 9.1[3] summarizes some spectroscopically derived constants for Rg-OH complexes. In the table ω'_s is the excited ($A^2\Sigma^+$) state stretching frequency along the van der Waals bond and $\omega'_s x_s$

Complex	ω'_s	ω_{sXs}'	D_0'	D_0''
Ne-OH	43	6.5	47-52	28
Ar-OH	170.2	9	717	107
Kr-OH	233.3	7.3	1752	117
Xe-OH				

Table 9.1: Experimentally determined vibrational constants for Rg-OH.[3]

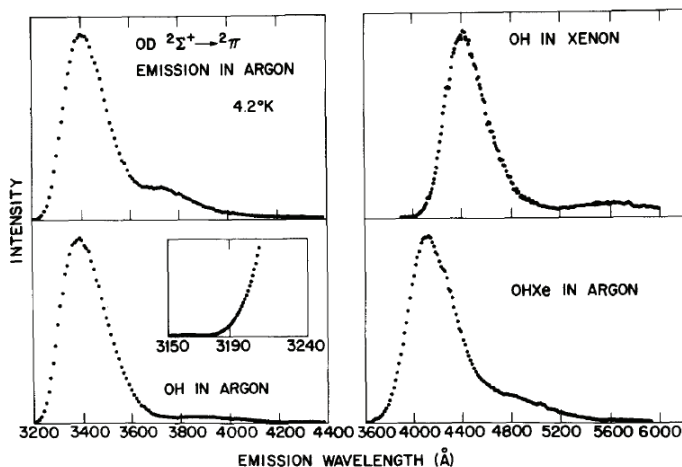


Figure 9.1: Fluorescence from various OH containing species.[5]

is the anharmonicity constant for the excited ($A^2\Sigma^+$) state. D'_0 and D_0'' are the dissociation energies for the $A^2\Sigma^+$ and $X^2\Pi$ states respectively. From the table one can see that the strength of the bonding in ground electronic state of the Rg-OH complexes (Rg= Ne, Ar, and Kr) is consistent with a weak long range interaction. However, the bonding in the excited state is stronger, and in the case of Rg=Kr, it is much stronger than a typical long-range interaction.

One should notice that the data for Xe-OH is lacking in Table 9.1. While there is no accurate determination of these constants for Xe-OH, it would be expected that the strength of the Xe-OH bond would be even stronger than a Kr-OH bond. Early experiments by Goodman and Brus[5] in the 1970's showed a roughly $5,000\text{ cm}^{-1}$ redshift in the $A^2\Sigma^+ \rightarrow X^2\Pi$ emission band of Xe-OH in solid Ar, compared with OH in an Ar matrix (see Figure 9.1). Brus and colleagues[5] were interested in the difference between a hydrogen bond, which is mediated by a proton, and other weak interactions. At the time of their study the strongest known bound rare gas complex is XeF($X^2\Sigma$), which is bound by roughly $1,200\text{ cm}^{-1}$. The lowest electronically excited state is the Xe^+F^- charge transfer state. Because OH is isoelectronic with F, Xe-OH was good candidate to study. Specifically, Brus and colleagues [5, 103] were interested

in the charge transfer between the heavier rare gases and OH and the ability for OH to hydrogen bond with very polarizable rare gases such as Xe. However, they did not determine the spectroscopic constants for Xe-OH either in the ground or first excited state.

Another item of interest for Brus and colleagues[5, 103] was the participation of molecular rotations in radiationless relaxation of Rg-OH species. By deconvoluting the fluorescence lifetimes for the $A^2\Sigma^+, \nu = 1$ they were able to measure the vibrational relaxation rates of Rg-OH and Rg-OD, and found the rate for Rg-OH to be faster. One would expect the pure vibrational relaxation rate of Rg-OH to be much slower than Rg-OD because it has a higher vibrational frequency. It is the energy dissipation into molecular rotations that shortens the lifetime of OH relative to OD. Additionally, Brus and colleagues[103, 5] observed a shortening of the lifetime of the Rg-OH complex as the rare gas became heavier. Table 9.2 summarizes the lifetimes and band centers for the fluorescence from the various molecules Brus and colleagues have studied.

More recently, some of the constants for $X^2\Pi$ the have been determined by Gilijamse *et al.*[9]. They studied the collisions between a molecular beam of OH with tunable velocity and Xe. Using LIF spectroscopy, they were able to examine the energetics of the OH radicals after the collision. Even though they did not form a stable Xe-OH complex, the information obtained from the collisions provided information about the interaction potential for the ground electronic state of the complex. Using *ab initio* calculations Gilijamse *et al.* also constructed potential energy surfaces for the ground state Xe-OH to interpret the information obtained from the experiments. There are two potential energy surfaces for the $X^2\Pi$ state: A' corresponds to the unpaired electron of the OH in the plane of the Xe, O, and H atoms; A'' corresponds to the unpaired electron in the plane of the Xe, O, and H atoms. Figure 9.2 shows the ground state potential energy surfaces for the A' (top) and A'' (bottom) ground

(0,0) Emission		
Species	Lifetime (μs)	Band Center (cm^{-1})
OH		
In vacuum	0.788 ± 0.013	$32,474^{\text{a}}$
In solid Ar	0.475 ± 0.010	29,412
In solid Ne	0.582 ± 0.010	32,362
In solid Kr	0.450 ± 0.020	27,548
In solid Xe	0.100 ± 0.040	22,727
ArHO		
In solid Ne	0.690 ± 0.010	
XeHO		
In solid Ne	0.450 ± 0.030	24,390

(a)= reference [104]

Table 9.2: Radiative lifetimes and emission band centers for (0,0) emission from different OH containing species.[5] For each measurement, the $A^2\Sigma^+ \leftarrow X^2\Pi$ band of OH was excited and $\nu(0,0)$ fluorescence was observed. There was no significant difference in the lifetimes of line centers for OH species versus OD species. There is however a shift in the asymmetrical distribution of the line shape.[5]

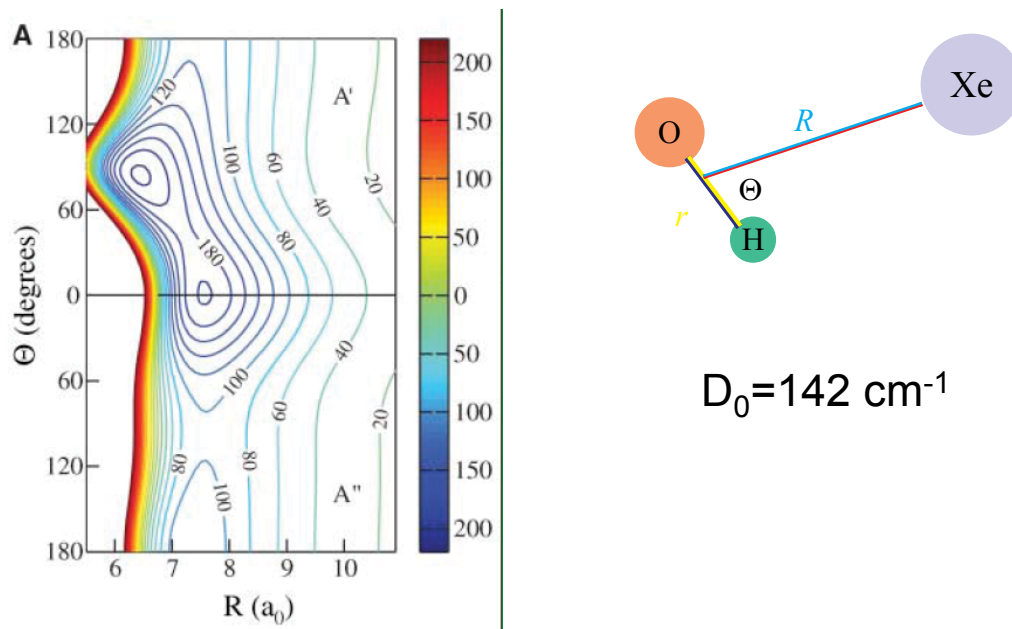


Figure 9.2: Xe-OH ground state potential energy surfaces.[9] The top surface is the A' surface and the bottom one is the A'' surface. The A' potential shows a T-shaped configuration with Θ near 90° . The top half of the potential is for the configuration where the unpaired electron of OH resides in a p orbital in the plane of the molecule. The bottom half is for when it is out of plane.

state along with a cartoon depicting the ground state geometry for the absolute minimum. The figure shows that the global minimum for the ground state (A') surface has a T-shaped geometry, with a weakly bound secondary minimum for the hydrogen bonded linear configuration. The D_e for the global minimum is roughly 224 cm^{-1} , which is indicative of a weak electrostatic bond. With such a shallow minimum and roughly only a 20 cm^{-1} barrier between the two configurations it is likely that there is enough zero point energy that the ground state is delocalized.

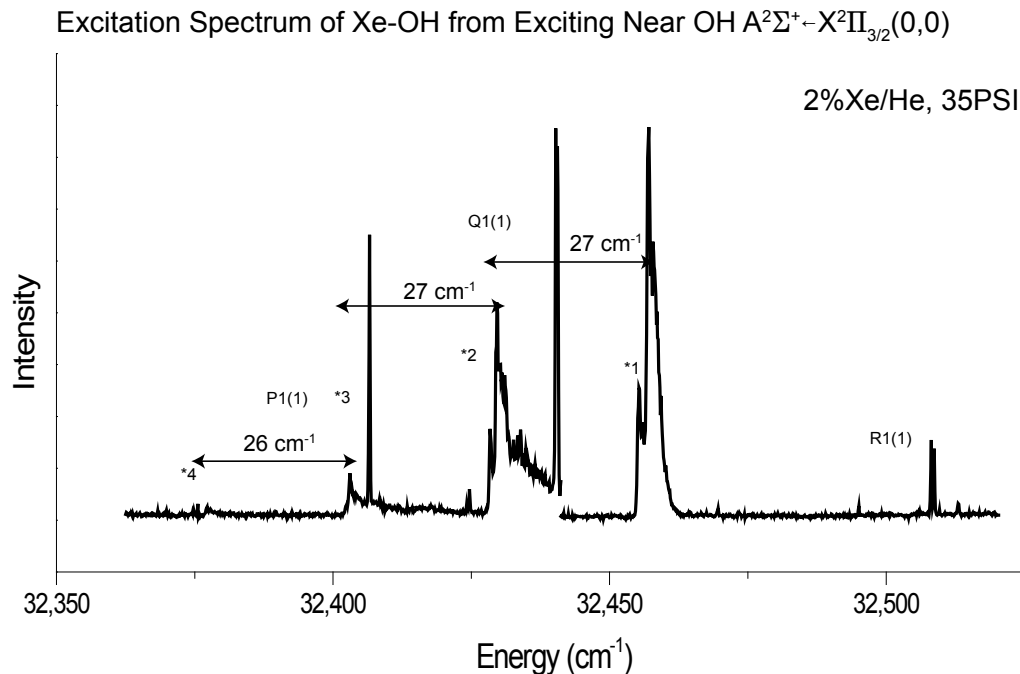


Figure 9.3: Fluorescence from Xe-OH induced by exciting OH $A^2\Sigma^+ \leftarrow X^2\Pi(0,0)$. The bands belonging to Xe-OH are marked with a "*".

Although, the experiments and calculations by Gilijamse *et al.* provided information on the $X^2\Pi$ state of Xe-OH, no information was obtained about the $A^2\Sigma^+$ state. Additionally, there has been no published report of gas-phase LIF spectra for the Xe-OH complex. To investigate the excited state Han *et al.*[4] recorded the LIF spectra of gas-phase Xe-OH (see Figure 9.3) by exciting the OH $A^2\Sigma^+ \leftarrow X^2\Pi(0,0)$ transition. In the figure the bands belonging to Xe-OH are labeled with a "*". The spectrum in Figure 9.3 is quite different from those recorded by Goodman and Brus in Figure 9.1. Additionally, the lifetime of Xe-OH in the gas phase recorded by Han *et al.* was $0.106 \mu\text{s}$, which is roughly 4 times shorter times than the lifetime recorded by Goodman and Brus for Xe-OH in Ne.

Taking into account that MI spectroscopy mimics gas-phase spectroscopy, especially for lighter molecules such as OH, it was very puzzling why there is such a discrepancy between the gas-phase and MI data. The experiments presented in this chapter reinvestigate the spectroscopy of matrix isolated Xe-OH to further probe the

difference the gas-phase and MI results.

9.2 Experiment Details— Generating OH and Xe-OH

After generating OH radicals, Xe-OH forms when Xe is added to the carrier gas or matrix host gas. Generating OH is a process that deserves a little more attention. Several papers pertaining to atmospheric chemistry describe the 193 nm photolysis of HNO₃ or HONO to produce OH.[105, 106, 107] Photolysis of N₂O/H₂ by 193 nm laser light also produces OH radicals. However, 193 nm laser light is usually created with pulsed excimer lasers. The problem with pulsed laser photolysis during matrix deposition is that the commonly used deposition process is continuous, and therefore, very little of the deposited material would be photolyzed. (There are methods for pulsed deposition of a matrix, but none of them were used here). Several other techniques have been used to produce OH for matrix experiments, all of which pass the sample material through a microwave discharge prior to deposition. The earliest method used to generate matrix isolated OH was passing a rare gas / water mixture through a discharge. The resulting vacuum ultra violet light would produce OH, even if the water was already frozen on the substrate.[108] A more recent paper compared the IR spectra of OH formed by passing four different samples through the discharge namely, water, O₂+H₂, NO₂+H₂, and O₃+H₂. [109] Based on this paper it was concluded the O₂+H₂ and O₃+H₂ methods produced spectra with the best signal to noise. Because oxygen is easier to handle than ozone, the oxygen method was used for the OH and Xe-OH spectra shown here.

In order to make OH and Xe-OH matrices from the O₂, H₂, and Xe precursors, the microwave discharge apparatus described in section 2.3.1.2 was used. For the OH experiments, a gas cylinder was prepared in house with 0.5% each of O₂ and H₂ with a balance of Ar using the techniques described in section 2.3.1. For the Xe-OH

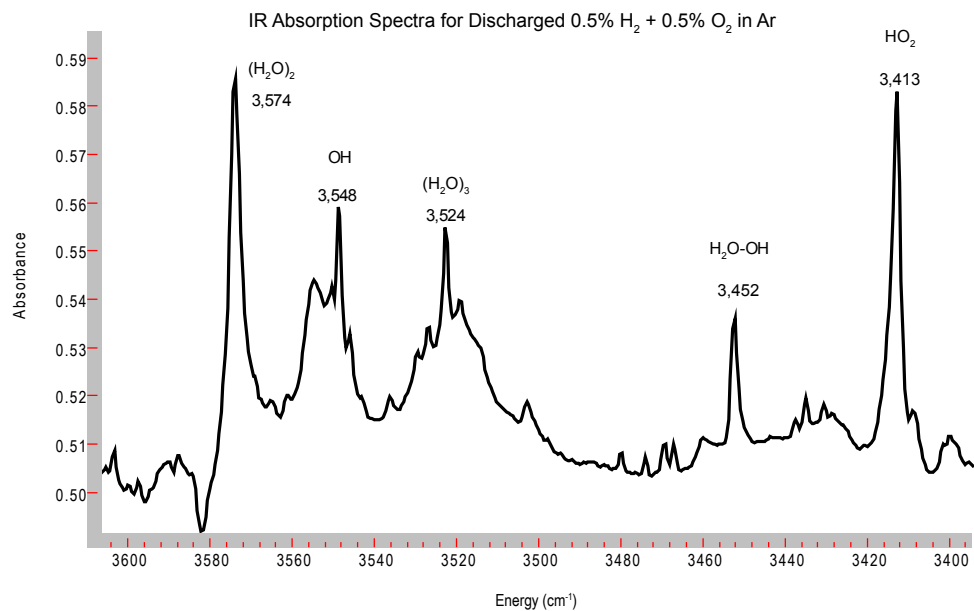


Figure 9.4: Infrared spectrum of discharged 0.5% O₂ + 0.5% H₂ in Ar. Two peaks in the spectrum are assigned to OH and labeled accordingly.

experiments, a similar cylinder was filled with anywhere between 0.5% to 4.0% Xe and 0.5% each of O₂ and H₂ with a balance of Ar. The gas mixtures were allowed to pass through the discharge and deposit on the CsI substrate at a rate of 3 mmol/hour for about 3 hours.

9.3 Results

9.3.1 IR Spectra

IR spectra were recorded immediately after deposition, and again after any annealing experiments. Figure 9.4 shows the IR spectrum of discharged 0.5% O₂ + 0.5% H₂ in Ar. Other OH containing species such as HO₂ were observed and are also labeled. Figure 9.5 shows the IR spectrum for a similar matrix except that 4.5% Xe was added to the gas mixture. While the “free” OH in Ar is observed, nothing in the spectrum

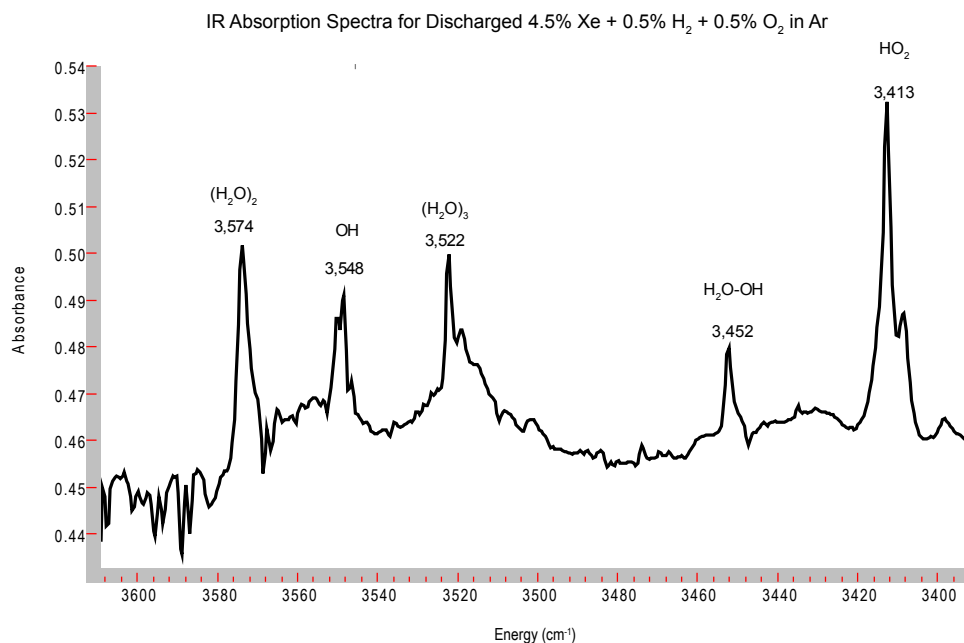


Figure 9.5: Infrared absorptions of discharged 4.5% Xe + 0.5% O₂ + 0.5% H₂ in Ar. “Free” OH is still present in this matrix. Xe containing species such as XeO were not observed. To date, no absorption has been assigned to Xe-OH.

could be assigned to a Xe containing species. For both the Xe containing and non Xe matrices, after annealing, the optical transmission of the matrix degraded enough to make the observed peaks less distinguishable, and there were no new features or growth / decrease of existing ones relative to each other.

9.3.2 Fixed Frequency Excitation

308 nm and 266 nm laser light was used for fixed frequency excitation of the matrices. Both laser energies produced almost identical emission spectra. Spectra taken with 308 nm excitation had a better signal to noise ratio, probably as a result of the higher and more stable excimer laser power. Therefore, 308 nm light was used to induce the fluorescence in the spectra shown in this section. It should be noted that the grating of the ISA 0.6 m monochromator was not suitable for recording first order spectra

around the $29,492\text{ cm}^{-1}$ region of the OH fluorescence. Unlike the experiments in Part I, a Jarrel Ash 0.25 m Ebert monochromator was used for recording the spectra presented here because it was more suitable for dispersing near UV fluorescence.

In order to ensure complex formation, the first Xe-OH matrices were formed with a gas mixture containing 4.5% Xe. It was found in later experiments that with this relatively high Xe concentration, most of the OH formed in the discharge was complexed with at least one Xe atom in the matrix (see Figure 9.6(a)). Figures 9.6 (a), (b), and (c) show several spectra from matrices made from Xe+H₂+O₂ passed through a discharge. In (a) a gate with no delay with respect to the laser firing and with a $0.06\ \mu\text{s}$ width was used in recording the spectrum. Even when the gate was varied, the band belonging to Xe-OH ($24,450\text{ cm}^{-1}$) was much stronger than one belonging to OH ($29,412\text{ cm}^{-1}$). In (b) the matrix only contained 0.5% Xe. The gate was the same in (a). Notice that the higher energy band has a long tail protruding in the red direction all the way out to the Xe-OH band. When a longer delay ($\sim 0.40\ \mu\text{s}$) was used to record the fluorescence from the matrix in (b) the sharp feature at $24,450\text{ cm}^{-1}$ flattened out as observed in Figure 9.6 (c).

Figures 9.6 (b) and (c) clearly show variation in radiational lifetimes for the two band systems. A closer look at the decay curves for both bands (Figure 9.7) shows that OH in Ar has a radiational lifetime $0.406\pm 0.003\ \mu\text{s}$ and can be fit with a single exponential. The Xe-OH band can be fit with a double exponential. The short time component has a lifetime of $0.035\pm 0.004\ \mu\text{s}$ and can be attributed to Xe-OH. The longer lived component ($0.379\pm 0.007\ \mu\text{s}$) is attributed to the broad red tail of the OH in Ar band. Again, the error given for the lifetimes is from the least square fitting routine analysis and does not reflect larger systematic error.

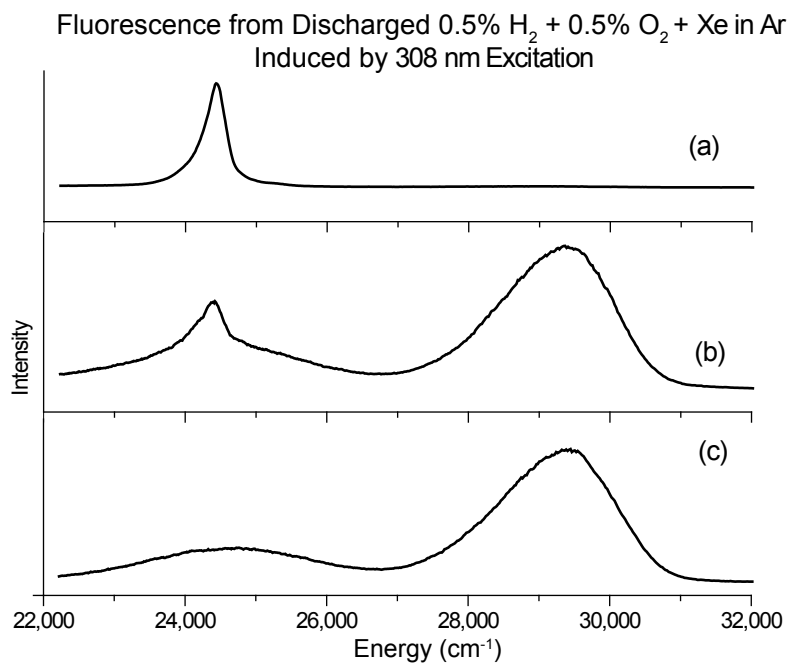


Figure 9.6: Fluorescence spectra of discharged 0.5% H₂ + 0.5% O₂ + Xe in Ar induced by 308 nm radiation. The matrix that gave rise to spectrum (a) contained 4.5% Xe. A gate with no delay with respect to the laser firing with a 0.06 μs width was used in recording the spectrum. The matrix that gave rise to spectrum (b) contained 0.5% Xe. A gate with no delay with respect to the laser firing and with a 0.06 μs width was used in recording the spectrum. (c) is from the same matrix as in (b). However, a gate with delay of 0.4 μs with respect to the laser firing and with a 0.3 μs width was used in recording the spectrum.

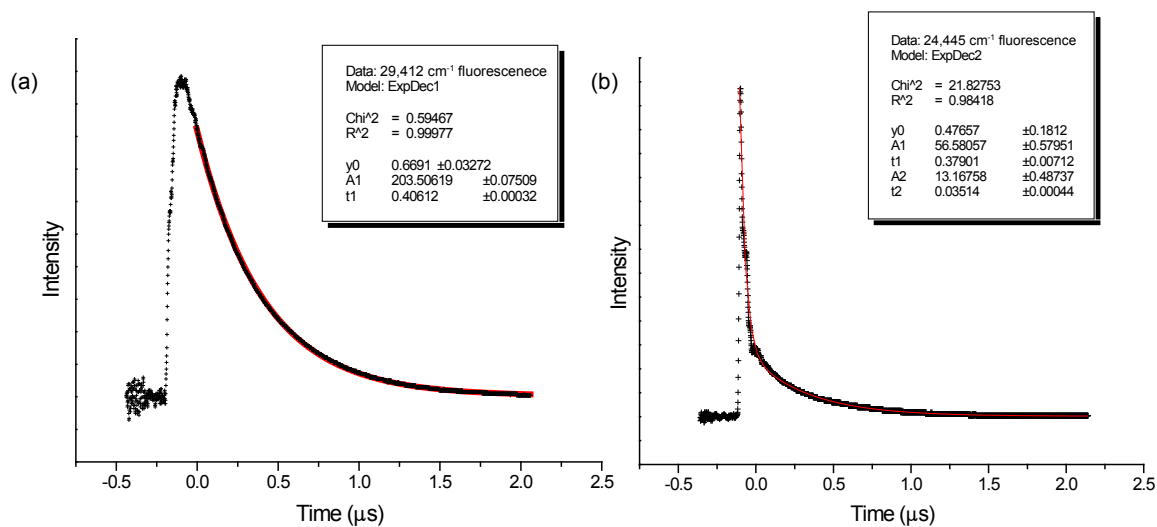


Figure 9.7: Fluorescence decay lifetimes of OH in Ar and Xe-OH in Ar. (a) The lifetime of the OH in Ar ($29,412\text{ cm}^{-1}$) emission band is $0.406 \pm 0.003\ \mu\text{s}$. (b) The lifetime of the Xe-OH ($24,450\text{ cm}^{-1}$) emission band is biexponential due to the long tail overlapping from the OH in Ar band as seen in Figure 9.6 (c). The lifetime for the Xe-OH in Ar fluorescence is $0.035 \pm 0.004\ \mu\text{s}$.

9.3.3 Tunable Excitation

Tunable laser excitation was used to investigate the excited levels giving rise to the fluorescence in Figure 9.6 (a). The band shown in Figure 9.6 (b) belonging to OH was not investigated because spectra for this band were previously recorded by Goodman and Brus.[5]. Wavelength selected excitation spectra were recorded by scanning the excitation wavelength while monitoring the light emitted by the $24,450\text{ cm}^{-1}$ emission band (Figure 9.8). A 340 cm^{-1} progression was observed for the Xe-OH A state. The region on the blue side of the spectrum is unresolvable because the bands are so broad that they overlap. Matrices made from sample precursors containing both 0.5% and 4.5% Xe produced the same spectrum. The spectrum was not recorded further in the red direction because of excess scattered light, even though appropriate long pass filters were used to ensure the observed spectra was fluorescence and not laser scatter. Again, the laser scatter issue was an artifact of this particular MI experiment setup, and no effort was spent to correct the problem because it had little effect on most of

Excitation Spectra Reordered by Monitoring the 24,450 cm^{-1} Emission Band

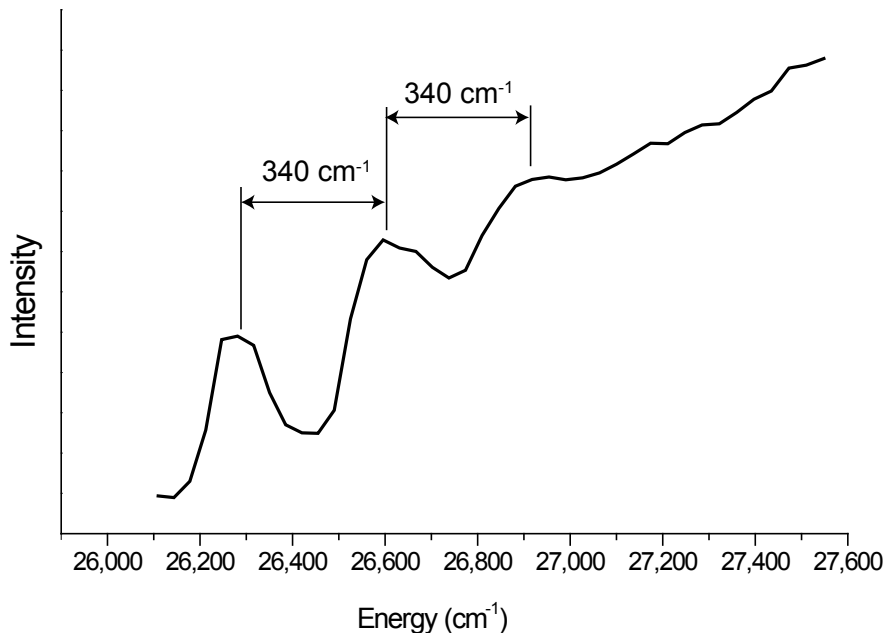


Figure 9.8: 24,550 cm^{-1} fluorescence from Xe-OH in Ar induced by tunable radiation. There is an observed 340 cm^{-1} progression. Both 0.5% and 4.5% Xe matrices produced the same spectra.

the experiments discussed here.

9.4 Analysis and Discussion

Evidence that both OH and Xe-OH were trapped in the Ar matrices came from a comparison of Cheng *et al.*'s[109] and Acquista *et al.*'s[108] IR spectra and Goodman and Brus's[5] fluorescence spectra. While, no peaks in the IR spectrum could be assigned to Xe-OH or other Xe containing species, the fluorescence spectra confirmed the presence of Xe-OH in the matrix. As is seen in Figures 9.5 and 9.7, all the observed peaks have a width of several wavenumbers. It is quite possible that matrix broaden peak assigned to OH masks the Xe-OH. It is unclear the exact extent Xe will perturb the OH stretching frequency, one might predict the perturbation to be

minimal because the ground state binding energy for the complex is only 224 cm^{-1} . Another factor that could make it harder to observe the OH stretch in Xe-OH is the low IR absorption strength. In many cases, the fluorescence quantum yield is much stronger than the IR absorptions for the same molecule making it much easier to observe the fluorescence. Additionally, the total IR throughput is very weak in this experiment setup, making many absorptions appear only slightly greater than the baseline. However, there is no reason why one would expect the strength of OH the IR absorptions for Xe-OH in Ar to be different from Oh in Ar.

The line centers of the UV and visible fluorescence bands for OH in Ar and Xe-OH in Ar coincide with the results published by Goodman and Brus.[5]. However, the FWHM for each of the bands is significantly narrower than the bands recorded by Goodman and Brus[5]. One possible explanation is that the concentration of the sample precursor in Goodman and Brus's experiments was higher so that various dimer, trimers, etc. were formed during the deposition process. These "clusters" would in turn cause inhomogeneous broadening of the bands. Additionally, the lifetime of Xe-OH in Ar reported here to be $0.035\ \mu\text{s}$ is roughly an order of magnitude faster than Goodman and Brus's $0.450\ \mu\text{s}$ for Xe-OH in Ne, and rather is closer to the $0.100\ \mu\text{s}$ he measured for OH in pure Xe. One likely explanation for the discrepancy in lifetimes is that Goodman and Brus may have used a single exponential function to fit their decay curve for Xe-OH in Ne. When the decay curve in Figure 9.7(b) is fitted with a single exponential function, the resultant lifetime is $0.289\pm 0.001\ \mu\text{s}$, which is more in line with the value Goodman and Brus reported. Based on the lifetimes reported in Table 9.2 the lifetime reported here is in good agreement with the trend that as the rare gas gets heavier, the lifetimes gets shorter. A contributing factor to the shortened lifetime of matrix isolated species versus the gas phase species is the index of refraction of the matrix. As one goes down the periodic table the polarizability of an element increases. In the case of the rare gas matrix host, in addition to a greater

interaction strength, this increase also increases the refractive index of the matrix and thus shortens the lifetime. The index of refraction for Ar is 1.000281 which is consistent with the observed shortened lifetime of OH in Ar versus the gas phase lifetime.

The 340 cm^{-1} progression shown in the excitation spectrum has been assigned to the A state stretching frequency of Xe-OH along the R axis. What is odd about this matrix excitation spectrum is that it is very different from unpublished gas-phase spectra also recorded in the Heaven group[4]. In the gas-phase, three vibrational levels close to D_e were observed for the excited A state in the excitation spectrum. The spectrum was resolved enough to show the P, Q, and R branches, but the rotational structure within the branches was not resolvable. Transitions from the ground electronic state to vibrationally excited levels in the A state that are near the dissociation limit may be the favored electronic transitions based on a Frank-Condon analysis. In contrast, vibrational levels closer to the bottom of the A state potential well are observed in the MI spectra in an Ar matrix. The more favorable Frank-Condon factors between the ground electronic state and lower vibrational levels in the $A^2\Sigma^+$ state may be a result of the stabilization of the ground state potential well by the Ar relative to the excited state.

The best way to understand the differences between the two experiments is by calculating a high quality potential energy surface for the Xe-OH excited state. Such a potential surface for the ground state was shown in Figure 9.2 and was discussed in Section 9.1.[9] Using the two surfaces the Frank-Condon factors could be calculated. At the time of these experiments, no such surface was available for the A state. However, very recently, the A state surface has been calculated by Merrit and Heaven and is shown in Figure 9.9.[10] Unlike in the X state, the global minimum geometry is predicted to be the oxygen bonded linear configuration ($D_e \approx 12,500\text{ cm}^{-1}$). The hydrogen bound configuration is still a secondary minimum ($D_e \approx 2,500\text{ cm}^{-1}$).

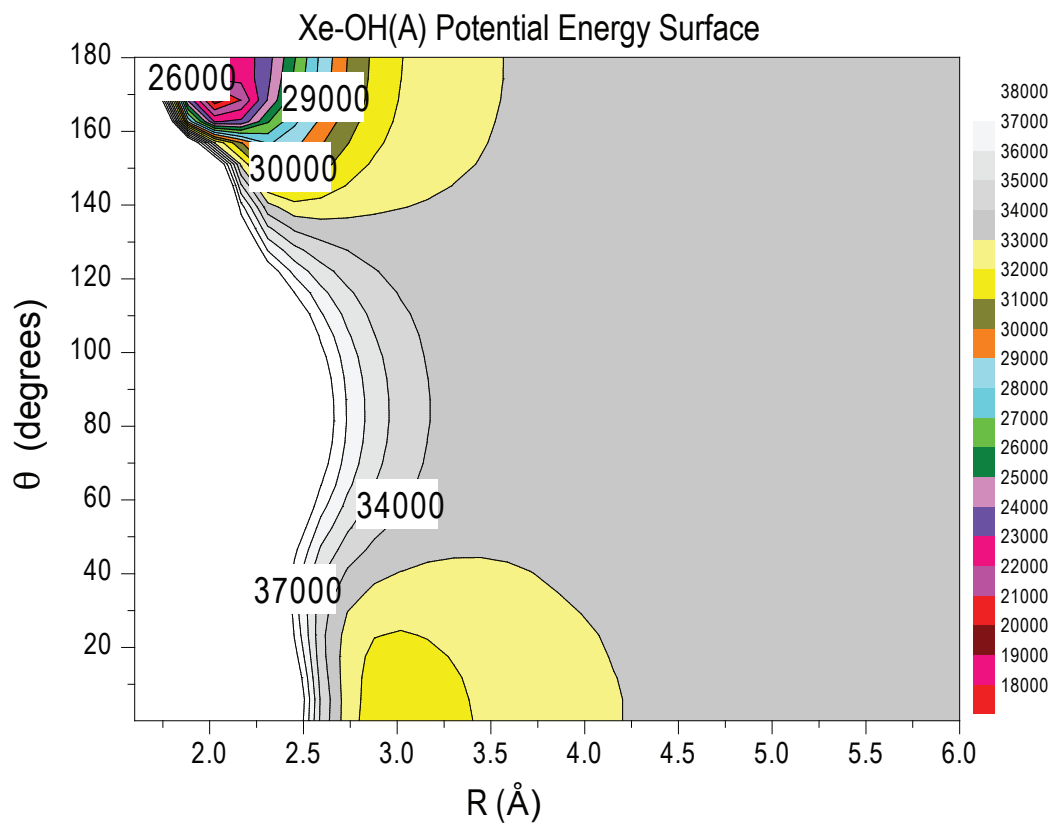


Figure 9.9: Xe-OH(A) potential energy surface.[10]

The next step in interpreting the gas-phase and MI spectra is to use the potential energy surfaces to calculate the bound state wavefunctions for both X and A states. Using the wavefunctions, the Frank-Condon factors can then be calculated. One point to keep in mind is that the potential surfaces are for gas-phase Xe-OH. It is quite possible that the Ar matrix host may help to stabilize certain configurations in both states. Further theoretical investigations should help understand the stabilization effect of Ar.

9.5 Conclusion

While there have been numerous studies on the family of Rg-HX complexes, data for Rg=Xe has been lacking. It has been known for a long time that Xe is different from other rare gases. The goal of these experiments was to obtain as much electronic structure information as possible from LIF MI experiments, which could help with interpreting gas phase LIF spectra and ultimately lead to an accurate potential energy surface for the Xe-OH A state. Also, observing the IR stretching frequency would give a indication of the interaction strength between the OH and Xe. Both LIF spectra from fixed frequency and tunable radiation were recorded. Unlike in the gas phase spectra, vibrational levels closer to the potential minimum in the A state ($\nu \approx 350 \text{ cm}^{-1}$) were accessible. Since the time of the MI experiments, the A state potential energy surface has been calculated. This surface can be used with the ground state surface[9] to calculate the Frank-Condon factors, which involves computing the bound state wavefunctions for both states. As with the experiments in Part I, it is intriguing that Ar can cause such large perturbations. Also, it is equally intriguing that the electronic spectra of Xe-OH are so different from other Rg-OH complexes. These observations should provide motivation for future experiments on Rg-OH complexes

Appendix A

A Note About Actinide Radioactivity

Mention the word uranium and people become scared and panic as if a nuclear bomb was detonated. Majority of actinide spectroscopy performed today uses either U or Th, both of which have stable, non-radioactive isotopes. The common isotopes used are either ^{238}U or ^{232}Th . These isotopes are often referred as the depleted form because the fissionable isotopes have already been removed for nuclear energy. Depleted U and Th have the same toxicity as any heavy metal such as lead. A big misnomer to the general population not working with depleted actinide compounds is that the actinide part of the molecule is what is so dangerous, when quite the opposite is true. For example, when UF_6 is exposed to water vapor in air, HF , one of the nastiest compounds, forms. While much of the actinide spectroscopy is performed in university laboratories without the necessary equipment to handle radioactive material, there is still a need for spectroscopic data for radioactive compounds such as Pu. There are facilities at Oak Ridge National Laboratory capable of dealing with the α emission from the radioactive actinides.

Appendix B

The Synthesis of Uranium Chloride

The synthesis of UCl_4 rather simple, provided one has the ability to carry out reactions under a dry atmosphere. The procedure used here was adapted from an article published by Kiplinger, Burns, *et al.*[110] 55 mL of hexachloropropene (Sigma Aldrich) was added to 200 mL 2-neck Schlenk tube containing a magnetic stir bar and connected to a Schlenk line. 5.3 g of UO_3 (Strem Chemicals) was added to second smaller Schlenk tube (~ 10 mL) which was connected to the side neck of the larger tube. A Schlenk frit was connected to the top neck of the larger tube. The tube containing the hexachloropropene was placed in an oil bath and heated to 190°C under strong nitrogen flow. While stirring, the UO_3 was added slowly by rotating the smaller flask. Upon addition of the UO_3 to the hexachloropropene, a very exothermic reaction occurred. So care was taken not to added to much UO_3 at a time. Once all the UO_3 was added the mixture was left to reflux overnight under nitrogen flow. The solution changed color from orangish-brown to a dark red as the reaction progressed. Temperature was measured by a thermometer in the oil bath.

The next morning the reaction was allowed to cool to room temperature. The mixture was then filtered on the Schlenk line and washed with methylene chloride (~ 100 mL) until the rinsing liquid became colorless. The remaining dark green powder

on the frit was left to dry overnight before it was taken into a glove box and transferred to a storage jar. Small vials of UCl_4 were removed from the glove box as needed.

The key to a successful synthesis is keeping the temperature just below the boiling point of hexachloropropene to provide the necessary activation energy without evaporating the solvent. The oil bath used here helps with this purpose. Also, the quantity of the reaction can easily be changed (as the published reaction used ~ 10 g UO_3), but the reaction size vessel should be altered so that UO_3 is completely covered by the solvent.

Bibliography

- [1] J. M. Grzybowski, and L. Andrews, *J. Chem. Phys* **68**, 4540 (1978).
- [2] R. D. Hunt, C. Thompson, P. Hassanzadeh, and L. Andrews, *Inorganic Chemistry* **33**, 388 (1994).
- [3] C. C. Carter, H.-S. Lee, A. B. McCoy, and T. A. Miller, *Journal of Molecular Structure* **525**, 1 (2000).
- [4] J. Han, and M. C. Heaven, “Fluorescence spectroscopy of XeOH in the gas phase,” (2007).
- [5] J. Goodman, and L. E. Brus, *Journal of Chemical Physics* **67**, 4858 (1977).
- [6] J. Li, B. E. Bursten, L. Andrews, and C. J. Marsden, *Journal of the American Chemical Society* **126**, 3424 (2004).
- [7] P. Pyykkö, J. Li, and N. Runeberg, *Journal of Physical Chemistry* **98**, 4809 (1994).
- [8] M. Zhou, L. Andrews, N. Ismail, and C. Marsden, *Journal of Physical Chemistry A* **104**, 5495 (2000).
- [9] J. J. Gilijamse, S. Hoekstra, S. Y. T. van de Meerakker, G. C. Groenenboom, and G. Meijer, *Science (Washington, DC, United States)* **313**, 1617 (2006).

- [10] J. Merrit, and M. C. Heaven, "Accurate Potential Energy Surfaces for the A' and A" Xe-OH," (2007).
- [11] L. Andrews, B. Liang, J. Li, and B. E. Bursten, *Journal of the American Chemical Society* **125**, 3126 (2003).
- [12] V. E. Bondybey, A. M. Smith, and J. Agreiter, *Chem. Rev.* **96**, 2113 (1996).
- [13] J. W. Hastie, R. H. Hauge, and J. L. Margrave, in C. N. R. Rao, and J. R. Ferraro, eds., "Spectroscopy in Inorganic Chemistry," , vol. 158–107 (Accademic Press, New York, 1970).
- [14] I. R. Dunkin, *Matrix Isolation Techniques, a Pratical Approach*, The Practical Approach in Chemistry Series (Oxford, New York, 1998).
- [15] M. Macler, *Spectroscopy and dynamics of matrix isolated iodine and iodine monobromide*, Ph.D. thesis, Emory University. Dept. of Chemistry (1991).
- [16] G. J. Hoffman, and V. A. Apkarian, *J. Phys. Chem.* **95**, 5372 (1991).
- [17] T. R. Burkholder, and L. Andrews, *J. Chem. Phys* **95**, 8697 (1991).
- [18] G. A. Ozin, S. A. Mitchell, and J. Garcia-Prieto, *Journal of Physical Chemistry* **86**, 473 (1982).
- [19] K. Fahmy, M. Merroun, K. Pollmann, J. Raff, O. Savchuk, C. Hennig, and S. Selenska-Pobell, *Biophysical Journal* **91**, 996 (2006).
- [20] P. C. Burns, K.-A. Kubatko, G. Sigmon, B. J. Fryer, J. E. Gagnon, M. R. Antonio, and L. Soderholm, *Angewandte Chemie, International Edition* **44**, 2135 (2005).
- [21] W. B. Lewis, L. B. Asprey, L. H. Jones, R. S. McDowell, S. W. Rabideau, and R. T. Paine, *J. Chem. Phys* **65**, 2707 (1976).

- [22] W. B. Lewis, F. Wampler, E. Huber, and G. Fitzgibbon, *J. Photochem.* **11**, 393 (1979).
- [23] W. B. Lewis, and A. H. Zeltmann, *J. Photochem.* **12**, 51 (1980).
- [24] W. W. Rice, F. B. Wampler, R. C. Oldenborg, W. B. Lewis, J. J. Tiee, and R. T. Pack, *J. Chem. Phys.* **72**, 2948 (1980).
- [25] E. Borsella, F. Catoni, and G. Freddi, *J. Chem. Phys.* **73**, 316 (1980).
- [26] P. M. Kroger, S. J. Riley, and G. H. Kwei, *J. Chem. Phys.* **68**, 4195 (1978).
- [27] D. D. Witte, R. Dumanchin, and M. Michon, *Chem. Phys. Lett.* **48**, 505 (1977).
- [28] N. M. Edelstein, *Journal of Alloys and Compounds* **223**, 197 (1995).
- [29] R. Tyagi, *Ab initio studies of systems containing actinides using relativistic effective core potentials.*, Ph.D. thesis, The Ohio State University (2005).
- [30] B. E. Bursten, E. J. Palmer, and J. L. Sonnenberg, Special Publication - Royal Society of Chemistry **305**, 157 (2006).
- [31] I. N. Levine, *Quantum Chemistry*, 5 ed. (Pentice Hall, Upper Saddle River, New Jersey, 2000).
- [32] R. W. Bethe, Hans A. Jackiw, *Intermediate quantum mechanics*, 3rd ed. (Benjamin/Cummings Pub. Co., Menlo Park, Calif., 1986), Hans A. Bethe, Roman W. Jackiw. 24 cm. Includes bibliographical references and index.
- [33] L. Gagliardi, B. O. Roos, P. Malmqvist, and J. M. Dyke, *Journal of Physical Chemistry A* **105**, 10602 (2001).
- [34] B. E. Bursten, M. L. Drummond, and J. Li, *Faraday Discussions* **124**, 1 (2003).
- [35] L. Jun, B. B. E, L. Binyong, and A. Lester, *Science* **295**, 2242 (2002).

- [36] B. Liang, L. Andrews, J. Li, and B. E. Bursten, *Inorganic Chemistry* **43**, 882 (2004).
- [37] B. O. Roos, W. Per-Olof, and G. Laura, *Faraday Discuss* **124**, 57 (2003).
- [38] L. Andrews, and X. Wang, *Journal of the American Chemical Society* **125**, 11751 (2003).
- [39] D. Hildenbrand, L. Gurvich, and V. Yungman .
- [40] E. G. Rauh, and R. J. Ackermann, *Journal of Chemical Physics* **60**, 1396 (1974).
- [41] F. Capone, Y. Colle, J. P. Hiernaut, and C. Ronchi, *Journal of Physical Chemistry A* **103**, 10899 (1999).
- [42] J. Han, V. Goncharov, L. A. Kaledin, A. V. Komissarov, and M. C. Heaven, *Journal of Chemical Physics* **120**, 5155 (2004).
- [43] M. E. Jacox, *Journal of Molecular Spectroscopy* **113**, 286 (1985).
- [44] M. E. Jacox, *Journal of Molecular Structure* **157**, 43 (1987).
- [45] M. Zhou, L. Andrews, J. Li, and B. E. Bursten, *Journal of the American Chemical Society* **121**, 9712 (1999).
- [46] J. Tague, Thomas J., L. Andrews, and R. D. Hunt, *Journal of Physical Chemistry* **97**, 10920 (1993).
- [47] R. D. Hunt, and L. Andrews, *Journal of Chemical Physics* **98**, 3690 (1993).
- [48] J. Li, B. E. Bursten, B. Liang, and L. Andrews, *Science (Washington, DC, United States)* **295**, 2242 (2002).
- [49] J. Han, L. A. Kaledin, V. Goncharov, A. V. Komissarov, and M. C. Heaven, *Journal of the American Chemical Society* **125**, 7176 (2003).

- [50] Q. Chang, *Ab Initio Calculations on UO₂*, Masters thesis, The Ohio State University (2002).
- [51] L. Gagliardi, M. C. Heaven, J. W. Krogh, and B. O. Roos, *Journal of the American Chemical Society* **127**, 86 (2005).
- [52] I. Infante, E. Eliav, M. J. Vilkas, Y. Ishikawa, U. Kaldor, and L. Visscher, *Journal of Chemical Physics* **127**, 124308/1 (2007).
- [53] D. W. Steinhaus, J. Radziemski, Leon J., R. D. Cowan, J. Blaise, G. Guelachvili, Z. B. Osman, and J. Verges, "Present status of the analyses of the first and second spectra of uranium (U I and U II) as derived from measurements of optical spectra." (1971).
- [54] L. A. Kaledin, J. E. McCord, and M. C. Heaven, *Journal of Molecular Spectroscopy* **164**, 27 (1994).
- [55] L. A. Kaledin, and M. C. Heaven, *Journal of Molecular Spectroscopy* **185**, 1 (1997).
- [56] S. D. Gabelnick, G. T. Reedy, and M. G. Chasanov, *Journal of Chemical Physics* **58**, 4468 (1973).
- [57] D. Majumdar, K. Balasubramanian, and H. Nitsche, *Chemical Physics Letters* **361**, 143 (2002).
- [58] J. R. Morrey, *Inorg. Chem.* **2**, 163 (1963).
- [59] J. R. Morrey, D. G. Carter, and J. B. Gruber, *J. Chem. Phys* **46**, 804 (1967).
- [60] R. McLaughlin, *J. Chem. Phys* **36**, 2699 (1962).
- [61] S. A. Arthers, and I. R. Beattie, *Journal of the Chemical Society, Dalton Transactions: Inorganic Chemistry (1972-1999)* 819–26 (1984).

- [62] C. Goerller-Walrand, S. De Houwer, L. Fluyt, and K. Binnemans, *Physical Chemistry Chemical Physics* **6**, 3292 (2004).
- [63] J. V. Wazer, and G. John, *J. Am. Chem Soc.* **70**, 1207 (1948).
- [64] P. F. Souter, and L. Andrews, *Journal of Molecular Structure* **412**, 161 (1997).
- [65] G. K. T. Conn, and C. K. Wu, *Transactions of the Faraday Society* **34**, 1483 (1938).
- [66] B. Kedzia, and B. Jezowska-Trzebiatowska, *Bulletin de l'Academie Polonaise des Sciences, Serie des Sciences Chimiques* **14**, 639 (1966).
- [67] H. Gerding, G. Prins, and W. Gabes, *Revue de Chimie Minerale* **12**, 303 (1975).
- [68] M. Gal, P. L. Goggin, and J. Mink, *Journal of Molecular Structure* **114**, 459 (1984).
- [69] R. G. Denning, D. N. P. Foster, T. R. Snellgrove, and D. R. Woodward, *Molecular Physics* **37**, 1089 (1979).
- [70] R. G. Denning, T. R. Snellgrove, and D. R. Woodward, *Molecular Physics* **37**, 1109 (1979).
- [71] R. G. Denning, J. C. Green, T. E. Hutchings, C. Dallera, A. Tagliaferri, K. Girarda, N. B. Brookes, and L. Braicovich, *Journal of Chemical Physics* **117**, 8008 (2002).
- [72] D. W. Green, S. D. Gabelnick, and G. T. Reedy, *Journal of Chemical Physics* **64**, 1697 (1976).
- [73] R. G. Denning, *Structure and Bonding (Berlin, Germany)* **79**, 215 (1992).
- [74] S. Matsika, Z. Zhang, S. R. Brozell, J.-P. Blaudeau, Q. Wang, and R. M. Pitzer, *Journal of Physical Chemistry A* **105**, 3825 (2001).

- [75] Z. Zhang, and R. M. Pitzer, *Journal of Physical Chemistry A* **103**, 6880 (1999).
- [76] S. Matsika, R. M. Pitzer, and D. T. Reed, *Journal of Physical Chemistry A* **104**, 11983 (2000).
- [77] K. Pierloot, and E. van Besien, *Journal of Chemical Physics* **123**, 204309/1 (2005).
- [78] T. J. Barker, R. G. Denning, and J. R. G. Thorne, *Inorganic Chemistry* **26**, 1721 (1987).
- [79] J. C. Krupa, E. Simoni, J. Sytsma, and N. Edelstein, *Journal of Alloys and Compounds* **213/214**, 471 (1994).
- [80] P. A. Haas, "Literature information applicable to the reaction of uranium oxides with chlorine to prepared uranium tetrachloride." (1992).
- [81] V. Goncharov, L. A. Kaledin, and M. C. Heaven, *Journal of Chemical Physics* **125**, 133202/1 (2006).
- [82] J. Selbin, and M. Schober, *Journal of Inorganic and Nuclear Chemistry* **28**, 817 (1966).
- [83] J. Jin, R. Gondalia, and M. C. Heaven.
- [84] R. Pitzer, "Normal Modes of Uranyl Chloride," (2005).
- [85] B. Kanellakopoulos, and H. Parthey, *Journal of Inorganic and Nuclear Chemistry* **28**, 2541 (1966).
- [86] S. D. Gabelnick, G. T. Reedy, and M. G. Chasanov, *Journal of Chemical Physics* **59**, 6397 (1973).
- [87] D. W. Green, G. T. Reedy, and S. D. Gabelncik, *J. Chem. Phys* **73**, 4207 (1980).

- [88] R. G. Denning, and I. D. Morrison, *Chemical Physics Letters* **180**, 101 (1991).
- [89] J. C. Miller, S. W. Allison, and L. Andrews, *J. Chem. Phys* **70**, 3524 (1979).
- [90] W. R. Wadt, and P. J. Hay, *Journal of the American Chemical Society* **101**, 5198 (1979).
- [91] M. Krauss, and W. J. Stevens, *J. Comp. Chem.* **4**, 127 (1983).
- [92] D. G. Fedorov, T. Nakajima, and K. Hirao, *J. Chem. Phys* **118**, 4970 (2003).
- [93] P. J. Hay, W. R. Wadt, L. R. Kahn, R. C. Raffanetti, and D. H. Phillips, *Journal of Chemical Physics* **71**, 1767 (1979).
- [94] D. W. Green, and G. T. Reedy, *Journal of Chemical Physics* **65**, 2921 (1976).
- [95] R. D. Hunt, J. T. Yustein, and L. Andrews, *Journal of Chemical Physics* **98**, 6070 (1993).
- [96] M. Zhou, and L. Andrews, *Journal of Chemical Physics* **111**, 11044 (1999).
- [97] G. P. Kushto, P. F. Souter, and L. Andrews, *Journal of Chemical Physics* **106**, 5894 (1997).
- [98] L. Gagliardi, and B. O. Roos, *Chemical Physics Letters* **331**, 229 (2000).
- [99] G. Herzberg, New York: Van Nostrand Reinhold, 1950, 2nd ed. (1950).
- [100] W. M. Uselman, and E. K. C. Lee, *Chemical Physics Letters* **30**, 212 (1975).
- [101] L. Gagliardi, and B. O. Roos, *Nature (London, United Kingdom)* **433**, 848 (2005).
- [102] L. Gagliardi, P. Pyykkö, and B. O. Roos, *Physical Chemistry Chemical Physics* **7**, 2415 (2005).

- [103] L. E. Brus, and V. E. Bondybey, *Journal of Chemical Physics* **63**, 786 (1975).
- [104] J. Han, "Spectrum of Gaseous OH in Jet," (2006).
- [105] A. A. Turnipseed, G. L. Vaghjiani, J. E. Thompson, and A. R. Ravishankara, *Journal of Chemical Physics* **96**, 5887 (1992).
- [106] T. Papenbrock, H. K. Haak, and F. Stuhl, *Berichte der Bunsen-Gesellschaft* **88**, 675 (1984).
- [107] R. D. Kenner, F. Rohrer, and F. Stuhl, *Journal of Physical Chemistry* **90**, 2635 (1986).
- [108] N. Acquista, L. J. Schoen, and J. Lide, David R., *Journal of Chemical Physics* **48**, 1534 (1968).
- [109] B. M. Cheng, Y. P. Lee, and J. F. Ogilvie, *Chemical Physics Letters* **151**, 109 (1988).
- [110] J. L. Kiplinger, D. E. Morris, B. L. Scott, and C. J. Burns, *Organometallics* **21**, 5978 (2002).